

AN ABSTRACT OF THE THESIS OF

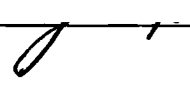
DENNIS MARC GUTHALS for the degree of DOCTOR OF PHILOSOPHY

in Chemistry presented on August 18, 1980

Title: COHERENT ANTI-STOKES RAMAN SPECTROSCOPY OF GASES

Redacted for Privacy

Abstract approved:

 Professor J. W. Nibler

The development and applications of a 0.2 cm^{-1} resolution Nd-YAG laser powered coherent anti-Stokes Raman spectroscopy, CARS, spectrometer for gas phase studies is chronicled in this thesis. Applications including CARS lineshape analysis, resonant CARS, and CARS of transient species and excited state molecules is reported.

The intensity of the signal generated at the CARS frequency, ω_3 , is governed by the behavior of the square of the nonlinear third order electronic susceptibility, $|\chi^{(3)}|^2$, which contains resonant, χ_{Res} , and nonresonant, χ_{NR} , terms. The various nonlinear optical three wave mixing, 3WM, processes which contribute to the intensity at ω_3 are discussed in terms of a semiclassical derivation of $\chi_{\text{Res}}^{(3)}$. From Maxwell's equations, a wave equation is obtained from expressing the induced nonlinear polarization, P^{NL} , as a function of the applied electric fields. A damped harmonic oscillator model is assumed for the

response of the electrons to the applied fields. Two similar expressions for $\chi_{\text{Res}}^{(3)}$ result from introducing the non-linearity into either the oscillator response (anharmonic term) or the driving force. $\chi^{(3)}$ is a function of various molecular parameters such as molecular number densities, Raman cross sections and Raman active vibration-rotation transition frequencies. A computer program is reported for calculating $|\chi^{(3)}|^2$ for homonuclear diatomic molecules. The program features a convolution over an analytical lineshape function to account for probe laser linewidths. Results are presented for calculated and observed spectra of O_2 gas at room temperature and in the free jet region of a supersonic molecular beam. Rotational cooling to 10K is indicated in the supersonic jet by CARS lineshape analysis.

The design and performance of the CARS spectrometer is discussed in terms of the various components. The linewidth of the primary ω_1 beam was reduced to about 0.03 cm^{-1} by employing two intracavity etalons and an electronic line narrowing device. Two dye laser designs and two optical pumping schemes are evaluated in terms of stability, linewidth, and ease of operation. The spectrometer resolution is limited by the dye laser linewidth of about $0.2\text{-}0.3 \text{ cm}^{-1}$. Wavelength tuning ranges and optimal concentrations are reported for 16 commercially available laser dyes pumped with the third harmonic of the Nd-YAG

laser at 355 nm. The laser dye outputs cover the visible range from 410 to 715 nm. High and low resolution broadband CARS spectra were obtained using an intensified optical multichannel analyzer as a detector.

Resonant CARS spectra are reported for nitrogen dioxide gas for frequency shifts of 1200-3400 cm^{-1} from a 532 nm ω_1 pump source. The spectra change dramatically with slight changes in ω_1 frequency. Much vibrational-rotational structure is observed but the analysis is complicated by the contribution of more than one resonant process. Various possible resonances are considered and absorption spectra and intensity measurements are used to assess the importance of some of these.

Intense 3WM spectra are reported for transient fragments produced by 266 nm laser photolysis of benzene, several substituted benzenes, and acetylene. Single pulse broadband 3WM spectra taken with an optical multichannel analyzer establish that the fragments are primary photoproducts obtained under collision-free conditions. The spectra consist of many features at anti-Stokes frequency shifts of 900-3100 cm^{-1} from a 532 nm ω_1 pump. Ninety degree fluorescence studies of the photolysis zone show that C_2 is produced in various electronic states and energetic consideration require that dissociation of C_6H_6 must involve two or more photons at 266 nm. Three wave mixing spectra of C_6D_6 are identical to those of C_6H_6 in the

anti-Stokes shift region near 3000 cm^{-1} and hence the transients do not contain CH bonds. Three wave mixing spectra of C_2H_2 fragments are also identical to those of benzene in the 3000 cm^{-1} region so that C_2 is believed to be responsible for both 3WM and fluorescence spectra. The 3WM spectra cannot be interpreted in terms of simple CARS vibrational resonances of C_2 . Intensity considerations suggest that enhancement due to multiple resonance is likely, and various electronic-electronic and vibrational-electronic 3WM processes are discussed. Calculations of possible resonances in the Swan system involving overtone Raman transitions indicate that many of the spectral features could arise from such processes.

Coherent Anti-Stokes Raman Spectroscopy
of Gases

by

Dennis Marc Guthals

A THESIS

submitted to

Oregon State University

in partial fulfillment of
the requirements for the
degree of

Doctor of Philosophy

June 1981

APPROVED:

Redacted for Privacy

Professor of Chemistry
in charge of major

Redacted for Privacy

Chairman of the Department of Chemistry

Redacted for Privacy

Dean of Graduate School

Date thesis is presented August 13, 1980

Typed by Deanna L. Cramer for Dennis Marc Guthals

ACKNOWLEDGEMENTS

The support and patience of my research director, Professor Joseph W. Nibler, is greatly appreciated. The collaboration and assistance of Dr. Kenneth P. Gross in the design and construction phases of the laser system and with much of the NO_2 and benzene work is also greatly appreciated. Dr. John Wilkerson is acknowledged for his help in writing the software necessary to generate the computer graphics. The final form for the CARS diatomic molecule spectral calculations was done in collaboration with Dr. Peter Huber-Wälchli, and his results for the supersonic molecular beam experiments are especially appreciated. Much thanks are in order for Jerry Allison for his insight and prompt help in overcoming problems associated with the electronics. John Archibald deserves special thanks for the many hours he spent teaching me machine shop skills, and for his assistance in the design and construction of the dry ice cooler for the OMA.

TABLE OF CONTENTS

| | <u>Page</u> |
|---|-------------|
| Chapter 1. Introduction, Background and Theory of CARS | 1 |
| 1.A Introduction | 1 |
| 1.B Electronic Susceptibilities. | 4 |
| 1.C Maxwell's Equations and Electromagnetic Waves | 7 |
| 1.D Nonlinear Induced Polarizations. | 13 |
| 1.E CARS Intensities | 25 |
| 1.F CARS Lineshapes. | 29 |
| Chapter 2. Experimental. | 41 |
| 2.A Basic Experimental Configuration | 41 |
| 2.B Nd-YAG Laser | 44 |
| 2.C YAG Harmonic Generation. | 49 |
| 2.D Dye Laser. | 53 |
| 2.E Broadband CARS | 61 |
| Chapter 3. Resonant CARS Spectra of NO ₂ | 65 |
| 3.A Introduction | 65 |
| 3.B Experimental | 66 |
| 3.C Results and Discussion | 66 |
| 3.D Summary. | 82 |
| Chapter 4. Electronic Three Wave Mixing Spectra of Transient Species Produced by UV Laser Photolysis of Benzene | 83 |
| 4.A Introduction | 83 |
| 4.B Experimental | 84 |
| 4.C General Spectral Characteristics | 85 |
| 4.D Photolysis Behavior. | 91 |
| 4.E Photolysis of Substituted Benzene. | 94 |
| 4.F Identification of Photofragments | 97 |
| 4.G Fragmentation Process. | 100 |
| 4.H Possible 3WM Processes | 103 |
| 4.I Summary. | 125 |
| References. | 127 |
| Appendix A. Fourier Transformations of the Wave Equation | 132 |
| Appendix B. Linear Electronic Susceptibility | 134 |
| Appendix C. CARS Intensity Calculations for Homonuclear Gaseous Diatomic Molecules | 137 |

Table of Contents -- continued

Page

| | |
|--|-----|
| Appendix D. Tuning Ranges of 355 nm Pumped Laser | |
| Dyes from 410 to 715 nm | 152 |

LIST OF FIGURES

| <u>Figure</u> | | <u>Page</u> |
|---------------|--|-------------|
| 1.1 | Energy level diagrams showing possible 3WM processes which could contribute to intensity at ω_3 | 6 |
| 1.2 | Orientation of the wave vectors for phase matching. | 26 |
| 1.3 | Plots of the real and imaginary parts of the susceptibility for an isolated resonance. . | 31 |
| 1.4 | Effects of the nonresonant contribution to the lineshape of total squared susceptibility . | 32 |
| 1.5 | Calculated "unconvoluted" CARS spectrum of the Q-branch of O_2 gas at 300K. | 34 |
| 1.6 | Observed spectrum of the Q-branch of O_2 gas at 300K | 35 |
| 1.7 | Observed and calculated spectra of the Q-branch of O_2 gas. | 39 |
| 2.1 | Schematic diagram of the CARS spectrometer. . . | 42 |
| 2.2 | Schematic diagram of Nd-YAG laser cavity. . . . | 45 |
| 2.3 | Oscilloscope traces of the 1064 nm Nd-YAG beam showing multimode and single mode operation | 47 |
| 2.4 | Orientation of KD*P type II crystal for second harmonic generation at 532 nm. | 51 |
| 2.5 | Orientation of KD*P type II crystal for third harmonic generation at 355 nm | 51 |
| 2.6 | Transverse optical pumping. | 54 |
| 2.7 | Semilongitudinal optical pumping. | 54 |
| 2.8 | Schematic drawing of the Hansch dye laser cavity used in this work. | 57 |
| 2.9 | Schematic diagram of the grazing incidence dye laser used in this work | 57 |

List of Figures -- continued

| <u>Figure</u> | | <u>Page</u> |
|---------------|--|-------------|
| 2.10 | Diagram showing the orientation of the two detectors mounted to the Spex-1402 spectrometer | 63 |
| 3.1 | Resonant CARS spectrum of 20 torr NO ₂ | 67 |
| 3.2 | Effect of slight ω_1 frequency variations on the $2\nu_2$ spectrum of NO ₂ | 71 |
| 3.3 | Energy level diagram for a possible "resonant" CARS triplet of NO ₂ | 73 |
| 3.4 | Possible resonant processes which could contribute to the CARS spectra of NO ₂ | 77 |
| 3.5 | Comparison of CARS and ω_2, ω_3 absorption spectra of NO ₂ | 80 |
| 4.1 | 3WM spectrum produced by 266 nm photolysis of 2.5 torr benzene. | 86 |
| 4.2 | 3WM spectra produced by 266 nm photolysis of 2.5 torr benzene, toluene, and chlorobenzene. | 90 |
| 4.3 | Single pulse broadband 3WM spectrum of 5 torr benzene. | 93 |
| 4.4 | 3WM spectra produced by 266 nm photolysis of C ₆ D ₆ and C ₂ H ₂ | 96 |
| 4.5 | Comparison of the 3WM and the C ₂ Swan band fluorescence spectra produced by 266 nm photolysis of benzene. | 99 |
| 4.6 | Energy level diagram of singlet and triplet states of C ₂ | 105 |
| 4.7 | Energy level diagram of the a and d triplet states of C ₂ | 106 |
| 4.8 | High resolution broadband 3WM spectra produced by 266 nm photolysis of 10 torr C ₆ H ₆ and 60 torr C ₂ H ₂ | 117 |

List of Figures -- continued

| <u>Figure</u> | | <u>Page</u> |
|-----------------|--|-------------|
| 4.9 | Energy level diagram of the a and d triplet states of C ₂ including the three sublevels for K = J ² - 1, J and J + 1 | 119 |
| 4.10 | Effect of ω_1 frequency on the 3WM spectra produced by 266 nm photolysis of 10 torr benzene. | 123 |
| <u>Appendix</u> | | |
| <u>Figures</u> | | |
| D.1 | 355 nm pumped laser dye tuning curves. | 153 |

LIST OF TABLES

| <u>Table</u> | <u>Page</u> | |
|-----------------|---|-----|
| 3.1 | CARS transitions observed in the $2\nu_2$ region for NO_2 | 76 |
| 4.1 | General features of 3WM resonances of 266 nm photolysis fragments of C_6H_6 , C_6D_6 and C_2H_2 | 87 |
| 4.2 | Observed high resolution 3WN spectral features of 266 nm photolyzed C_6H_6 and C_2H_2 , and calculated Swan band resonances | 111 |
| <u>Appendix</u> | | |
| <u>Tables</u> | | |
| C.1 | Table of O, Q, and S-branch fundamental transition frequencies for O_2 for $J = 0 - 30$ | 149 |
| C.2 | Table of unconvoluted CARS intensity maxima for O_2 at 300 K | 150 |
| C.3 | Table of convoluted CARS intensity maxima for O_2 at 300K. | 150 |
| D.1 | Concentration and tuning ranges for 355 nm pumped dyes | 153 |

COHERENT ANTI-STOKES RAMAN SPECTROSCOPY OF GASES

CHAPTER 1

INTRODUCTION, BACKGROUND, AND THEORY OF CARS

1.A Introduction

Coherent anti-Stokes Raman spectroscopy, CARS, was first reported by Terhune and Maker in 1964 [1, 2]. Initial experiments were performed on solid and liquid samples and the first CARS signal from a gas was observed by Rado in 1967 [3]. In the early 1970's, Taran and co-workers in France advanced gas phase CARS techniques and pioneered applications to combustion analysis [4]. These studies yielded important information such as concentrations and temperatures during the course of the combustion process. Harvey and co-workers, at NRL, used CARS to probe N_2 and D_2 arc plasmas in 1976, and were able to measure vibrational and rotational temperatures [5]. At this point in time, the work presented in this thesis was initiated. The latter part of the 1970's has experienced a tremendous growth in the popularity and applications of CARS as evidenced by a number of recent review articles [6-10] and reflecting the increased availability of high powered laser sources.

The four research objectives of this work were:

1. to further develop techniques for the application of CARS to gas phase systems. This involved computer modeling of gas phase CARS lineshapes and is presented in the remainder of Chapter 1.
2. to design and construct a stable and reliable CARS spectrometer system based on a Nd-YAG laser. Chapter 2 contains a description of the spectrometer.
3. to explore means to improve CARS detection limits in gases. One such method is by electronic resonance enhancement. Chapter 3 discusses the resonant CARS spectra of NO_2 .
4. to apply the above techniques to the study transient species which are very difficult or impossible to probe by other means. A study of the fragments formed by the 266 nm photolysis of benzene is the topic of Chapter 4.

The CARS process involves the optical mixing of two coherent beams, of frequencies ω_1 and ω_2 , through the bulk third order susceptibility, $\chi^{(3)}$, of the sample to generate the CARS beam at frequency $\omega_3 = 2\omega_1 - \omega_2$. The intensity of ω_3 is proportional to the square of the susceptibility, $|\chi^{(3)}|^2$, and can be calculated from known molecular parameters. It is possible to compare observed and calculated CARS spectra so as to accurately extract parameters of interest such as number densities, Raman cross sections, and vibrational and rotational temperatures.

The procedure used for calculating $\chi^{(3)}$ begins with a power series expansion of the induced polarization in terms of the applied electromagnetic fields. An expression for $\chi^{(3)}$ follows from the relationships in Maxwell's equations and assuming a damped harmonic oscillator model for the response of the electrons to the applied electric fields. $\chi^{(3)}$ contains both resonant, χ_{Res} , and nonresonant, χ_{NR} , terms. χ_{Res} is made up of real, χ' , and imaginary, χ'' , parts which contain electronic and vibrational resonance denominator terms along with other molecular parameters. The "normal" CARS experiment is only concerned with vibrational resonances. χ_{NR} arises from the response of all the electrons to the applied fields and produces a constant background intensity. The total susceptibility must be summed over all molecular resonances, and the effects of the probing laser lineshapes are considered. Results for such calculations for O_2 are shown along with experimental results. The presence of χ_{NR} places a detection limit on dilute samples. Various polarization [11] and interference [12] schemes have been proposed to reduce χ_{NR} but these have not been convenient in practice. Another approach to overcome χ_{NR} is through additional electronic resonance enhancement of χ_{Res} .

1.B Electronic Susceptibilities

The polarization, $P_{(\omega, t)}$, induced by the interaction of an electromagnetic field, $E_{(\omega, t)}$, with a dielectric medium may be represented by a power series expansion of the electric field [13]

$$P_{(\omega, t)} = \chi^{(1)} E_{(\omega, t)} + \chi^{(2)} E_{(\omega, t)}^2 + \chi^{(3)} E_{(\omega, t)}^3 + \dots, \quad (1.1)$$

The coefficients, χ , are known as the electronic susceptibilities which will be shown to be dependent on resonant frequencies and other properties of the medium. The first term in the series represents the familiar linear electronic susceptibility, $\chi^{(L)}$, and describes the behavior of such parameters as the index of refraction, n , and the absorption coefficient, α . The higher order susceptibilities are quite small compared to $\chi^{(L)}$ and the nonlinear effects predicted are only observed when very large electric fields are applied. The recent availability of high peak powered pulsed lasers has generated much interest in various nonlinear optical techniques.

One such technique is coherent anti-Stokes Raman spectroscopy, CARS, which depends on the third order susceptibility, $\chi_{(\omega_3)}^3$, at the anti-Stokes Raman shifted frequency, ω_3

$$\omega_3 = 2\omega_1 - \omega_2 = \omega_1 + (\omega_1 - \omega_2)$$

$$\omega_3 = \omega_1 + \omega_{nk} . \quad (1.2)$$

ω_1 and ω_2 are usually provided by pulsed lasers with peak powers in the KW to GW range and ω_{nk} corresponds to a Raman active vibrational frequency between states n and k . ω_1 is of fixed frequency and is usually more intense than a tunable ω_2 beam. Figure (1.1) shows the energy levels involved for several processes which may contribute to intensity at the CARS frequency, ω_3 . CARS is concerned primarily with the resonance process described in figure (1.1f) but the complications that may arise from the electronic resonances, figures (1.1c,d,e,g,h), must not be neglected. The interpretation of the CARS spectra of NO_2 and the photofragments of benzene (chapters 4 and 5) rely heavily upon such electronic resonant processes. Non-resonant processes, figure (1.1a,b), due to the bulk electronic response, also contribute to the CARS signal.

CARS can also be done with a broadband dye laser replacing the tunable ω_2 source. This makes possible one laser shot spectroscopy which is particularly well suited for the study of transient species.

The sections that follow discuss the parametric three wave mixing (3WM) processes involved, in terms of a semi-classical derivation of $\chi_{(\omega_3)}^{(3)}$ similar to that demonstrated by Terhune [2], DeWitt et al. [14] and others. Idealized,

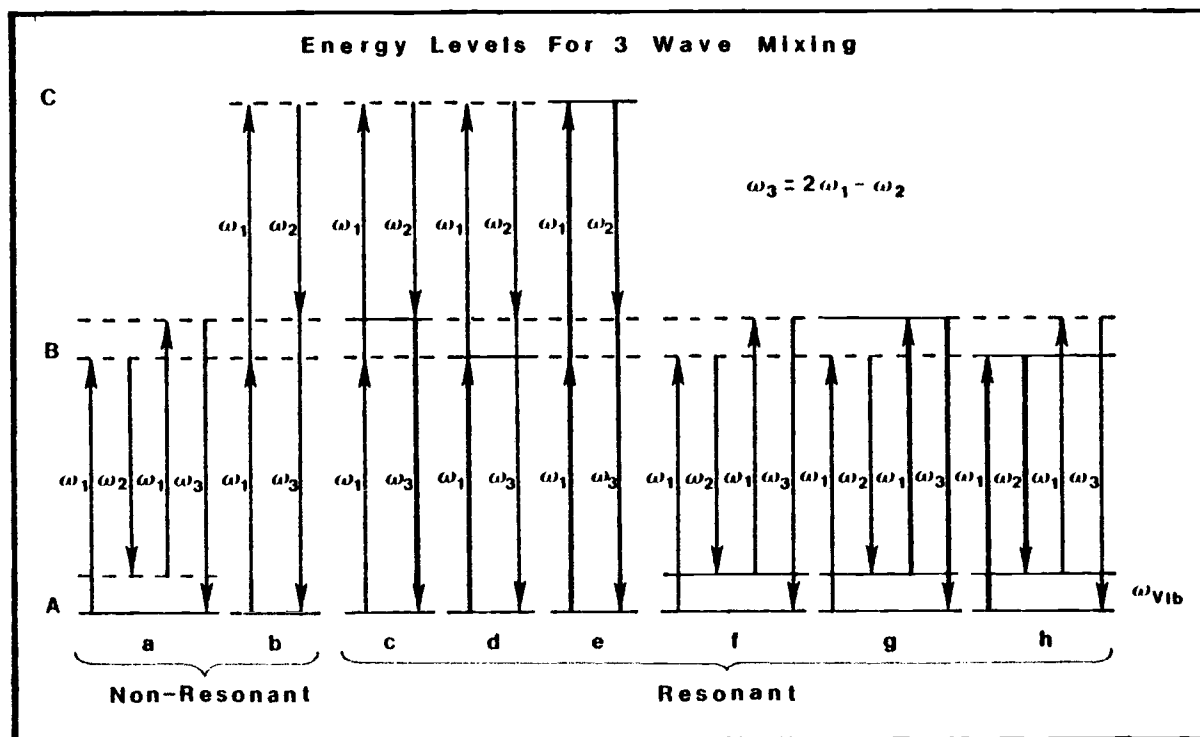


Figure 1.1. Energy level diagrams showing possible 3WM processes which could contribute to intensity at ω_3 . (a) and (b) produce nonresonant signal at ω_3 ; (c) and (d) involve a one photon resonance in either ω_3 or ω_1 ; (e) involves a two photon resonance in ω_1 ; (f) "normal CARS" involving a Raman resonance in $\omega_1 - \omega_2$; (g) and (h) multiple resonances in not only $\omega_1 - \omega_2$ but also in either ω_1 and ω_3 (g) or ω_1 and ω_2 (h).

monochromatic laser sources are assumed initially in this discussion. The effects of using real lasers as sources are dealt with in the latter parts of this chapter. The discussion begins with a review of Maxwell's equations and the properties of electromagnetic waves.

1.C Maxwell's Equations and Electromagnetic Waves

The interaction of electromagnetic waves and matter is governed by Maxwell's equations which may be written as follows (in c.g.s. units) [15]:

$$\bar{\nabla} \times \bar{E} = -\frac{1}{C} \frac{\partial \bar{B}}{\partial t} \quad (1.3)$$

$$\bar{\nabla} \times \bar{B} = \frac{1}{C} \left(\frac{\partial \bar{D}}{\partial t} + 4\pi \bar{J} \right) \quad (1.4)$$

$$\bar{\nabla} \cdot \bar{D} = 4\pi \rho \quad (1.5)$$

$$\bar{\nabla} \cdot \bar{B} = 0 \quad (1.6)$$

\bar{E} and \bar{B} are called the electric field vector and the magnetic induction vector respectively, and together they describe the electromagnetic field. \bar{J} is the free charge electric current density and ρ is the electric charge density. The electric displacement vector, \bar{D} , and the magnetic field vector, \bar{H} , are defined by the following two equations:

$$\bar{\mathbf{B}} = \bar{\mathbf{H}} + 4\pi\bar{\mathbf{M}} \quad (1.7)$$

$$\bar{\mathbf{D}} = \bar{\mathbf{E}} + 4\pi\bar{\mathbf{P}} \quad (1.8)$$

where $\bar{\mathbf{M}}$ is the magnetization and $\bar{\mathbf{P}}$ is the induced polarization.

In an isotropic material under nonrelativistic conditions the following constitutive relations apply [16]:

$$\bar{\mathbf{J}} = \sigma\bar{\mathbf{E}} \quad (1.9)$$

$$\bar{\mathbf{P}} = \chi\bar{\mathbf{E}} \quad (1.10)$$

$$\bar{\mathbf{D}} = \epsilon\bar{\mathbf{E}} \quad (1.11)$$

$$\bar{\mathbf{B}} = \mu\bar{\mathbf{H}} \quad (1.12)$$

where σ is the specific conductivity, χ is the electronic susceptibility, ϵ is the dielectric constant, and μ is the magnetic permeability. As was noted earlier, in the presence of large fields, equations (1.9-1.12) must include higher order nonlinear terms. These higher order terms will be introduced later as needed to generate a form of (1.1).

A wave equation which $\bar{\mathbf{E}}$ must satisfy separately may be obtained from Maxwell's first two equations. Taking the curl of Maxwell's first equation (1.3) yields

$$\bar{\nabla} \times (\bar{\nabla} \times \bar{\mathbf{E}}) = -\frac{1}{c} \frac{\partial}{\partial t} (\bar{\nabla} \times \bar{\mathbf{B}}) . \quad (1.13)$$

Rewriting Maxwell's second equation (1.4) with the substitution of (1.8) for $\bar{\mathbf{D}}$ gives

$$\bar{\nabla} \times \bar{\mathbf{B}} = \frac{1}{c} \left(\frac{\partial \bar{\mathbf{E}}}{\partial t} + 4\pi \frac{\partial \bar{\mathbf{P}}}{\partial t} + 4\pi \bar{\mathbf{J}} \right) . \quad (1.14)$$

At this point it is important to carefully define what is meant by charge current density. The second term in (1.14) indicates that a charge current density is produced by a time varying change in the polarization. This quantity, $\frac{\partial \bar{\mathbf{P}}}{\partial t}$, is known as the bound charge current density and must be distinguished from the free charge current density, $\bar{\mathbf{J}}$.

The CARS experiment is carried out in the absence of free charges ($\sigma = 0$, $\bar{\mathbf{J}} = 0$) but it is the bound charge current density which gives rise to the electronic susceptibility. Since $\bar{\mathbf{J}} = 0$, Maxwell's second equation (1.4) becomes

$$\bar{\nabla} \times \bar{\mathbf{B}} = \frac{1}{c} \left(\frac{\partial \bar{\mathbf{E}}}{\partial t} + 4\pi \frac{\partial \bar{\mathbf{P}}}{\partial t} \right) . \quad (1.15)$$

Substitution of (1.15) into (1.13) leads to

$$\bar{\nabla} \times (\bar{\nabla} \times \bar{\mathbf{E}}) = -\frac{1}{c^2} \left(\frac{\partial^2 \bar{\mathbf{E}}}{\partial t^2} + 4\pi \frac{\partial^2 \bar{\mathbf{P}}}{\partial t^2} \right) . \quad (1.16)$$

This wave equation in time expresses the desired polarization induced by the applied field $\bar{\mathbf{E}}$. From (1.8) and (1.11) it is seen that

$$\epsilon \bar{\mathbf{E}} = \bar{\mathbf{E}} + 4\pi \bar{\mathbf{P}} \quad (1.17)$$

and (1.15) further simplifies to

$$\bar{\nabla} \times (\bar{\nabla} \times \bar{\mathbf{E}}) = -\frac{\epsilon}{c^2} \frac{\partial^2 \bar{\mathbf{E}}}{\partial t^2} . \quad (1.18)$$

The equation of wave motion suggests that the induced field propagates through the medium with a velocity given by

$$v = \frac{c}{\sqrt{\epsilon}} \quad (1.19)$$

and leads to Maxwell's definition of the index of refraction as

$$n = \frac{c}{v} = \sqrt{\epsilon} . \quad (1.20)$$

Equation (1.16) may be expressed in terms of a physically measurable quantity, ω , by performing a Fourier transformation on $\bar{\mathbf{P}}(t)$ and $\bar{\mathbf{E}}(t)$ (see Appendix A).

$$\bar{\nabla} \times \bar{\nabla} \times \bar{\mathbf{E}}_{(\omega)} - \frac{\omega^2}{c^2} \bar{\mathbf{E}}_{(\omega)} = \frac{4\pi\omega^2}{c^2} \bar{\mathbf{P}}_{(\omega)} \quad (1.21)$$

The induced polarization, $\bar{\mathbf{P}}_{(\omega)}$, may now be expressed as consisting of linear and nonlinear terms

$$\bar{\mathbf{P}}_{(\omega)} = \mathbf{P}_{(\omega)}^{\text{L}} + \mathbf{P}_{(\omega)}^{\text{NL}} \quad (1.22)$$

where L and NL correspond to linear and nonlinear respectively. Substitution of (1.22) into the wave equation (1.21) yields

$$\bar{\nabla} \times \bar{\nabla} \times \bar{\mathbf{E}}_{(\omega)} - \frac{\omega^2}{c^2} (\bar{\mathbf{E}}_{(\omega)} + 4\pi\mathbf{P}_{(\omega)}^{\text{L}}) = \frac{4\pi\omega^2}{c^2} \bar{\mathbf{P}}_{(\omega)}^{\text{NL}} . \quad (1.23)$$

The wave equation (1.23) may also be expressed in terms of the dielectric constant or the index of refraction since from (1.10) and (1.17)

$$\epsilon = 1 + 4\pi \chi_{(\omega)}^L = n^2 \quad (1.24)$$

which leads to

$$\bar{\nabla} \times \bar{\nabla} \times \bar{E}_{(\omega)} - \frac{\omega^2}{c^2} \epsilon \bar{E}_{(\omega)} = \frac{4\pi\omega^2}{c^2} \bar{P}_{(\omega)}^{NL} \quad (1.25a)$$

or

$$\bar{\nabla} \times \bar{\nabla} \times \bar{E}_{(\omega)} - \frac{\omega^2 n^2}{c^2} \bar{E}_{(\omega)} = \frac{4\pi\omega^2}{c^2} \bar{P}_{(\omega)}^{NL} . \quad (1.25b)$$

The field propagates through the medium in the form of oscillating dipoles and the induced polarization can be written to include nonlinear terms

$$\bar{P}_{(\omega)} = -Ne [\bar{q}_{(\omega)}^L + \bar{q}_{(\omega)}^{NL}] = \chi_{(\omega)}^L \bar{E}_{(\omega)} + \chi_{(\omega)}^{NL} \bar{E}_{(\omega)}^{NL} . \quad (1.26)$$

Ne is the number of dipoles per cm^3 , \bar{q} is the dipole displacement from equilibrium position coordinate, and e is the electron charge. The relation between $\chi_{(\omega)}^L$ and n that is shown in (1.24) is deduced from a damped harmonic oscillator approximation for the induced linear polarization. This solution for $\chi_{(\omega)}^L$ is shown in Appendix B since a similar model will be used to arrive at the nonlinear susceptibility.

The electronic susceptibility, $\chi_{(-\omega, \omega_1, \dots, \omega_r)}^{(r)}$ is a tensor of rank $r+1$ and is invariant with respect to the $r!$ permutations of the frequencies. If n frequencies are the same, $n!$ permutations must be divided out. In component form, the polarization can be written as [14]

$$P_{(\omega)}^{(r)} = \frac{r!}{n!} \chi_{(\omega)}^{(r)} E_{(\omega)} \cdots E_{(\omega_r)} .$$

For CARS $r=3$ with two frequencies equal ($n=2$) and

$$P_{(\omega_3)}^{(3)} = \frac{3!}{2!} \chi_{(-\omega_3, \omega_1, \omega_3, \omega_2)}^{(3)} E_{(\omega_1)}^2 E_{(\omega_2)}$$

$$P_{(\omega_3)}^3 = 3 \chi_{(\omega_3)}^{(3)} E_{(\omega_1)}^2 E_{(\omega_2)} .$$

or

$$\chi_{\text{CARS}} = 3 \chi_{(\omega_3)}^{(3)} \tag{1.27}$$

From Appendix B the linear electronic susceptibility is

$$\chi_{(\omega)}^L = \frac{Ne^2}{m} \left(\frac{1}{\omega_0^2 - \omega^2 - i\Gamma\omega} \right) \tag{1.28a}$$

or by making the substitution of $D_{(\omega)}$ for the denominator

$$\chi_{(\omega)}^L = \frac{Ne^2}{m} \left(\frac{1}{D_{(\omega)}} \right) . \tag{1.28b}$$

Since, in the CARS experiment, two driving fields are present at frequencies ω_1 and ω_2 , (1.28b) can be re-written as

$$\chi_{(\omega_3)}^L = \frac{Ne^2}{m} \left(\frac{1}{D(\omega_1)} + \frac{1}{D(\omega_2)} \right). \quad (1.29)$$

The linear susceptibility at ω_3 resulting from the applied fields at ω_1 and ω_2 will be used in deriving the nonlinear susceptibility, $\chi_{(\omega_3)}^{NL}$, terms needed to arrive at $\chi_{(\omega_3)}^{(3)}$.

1.D Nonlinear Induced Polarizations

The nonlinear response of a dipole, $P_{(\omega)}^{NL}$, to an applied electric field may be approximated by a damped anharmonic oscillator model;

$$\frac{\partial^2 \bar{q}}{\partial t^2} + \Gamma \frac{\partial \bar{q}}{\partial t} + \omega_0^2 \bar{q} + \lambda \bar{q}^2 = -\frac{eE}{m}. \quad (1.30)$$

All of the terms have been defined in Appendix B for a damped harmonic oscillator with the exception of λ which is introduced now as a small perturbation or anharmonic coefficient.

Following perturbation theory, \bar{q} can be assumed to have a solution in terms of an expansion of \bar{q} in increasing powers of λ

$$\bar{q} = \bar{q}_1 + \lambda \bar{q}_2 + \lambda^2 \bar{q}_3 + \dots \quad (1.31)$$

$$\bar{q}^2 = \bar{q}_1^2 + 2\lambda \bar{q}_1 \bar{q}_2 + \lambda^2 (2\bar{q}_1 \bar{q}_2 + \bar{q}_2^2) + \dots \quad (1.32)$$

Substitution of (1.31) and (1.32) and (1.30) gives:

$$\begin{aligned}
& \left(\frac{\partial^2 \bar{q}_1}{\partial t^2} + \lambda \frac{\partial^2 \bar{q}_2}{\partial t^2} + \lambda^2 \frac{\partial^2 \bar{q}_3}{\partial t^2} + \dots \right) \\
& + \Gamma \left(\frac{\partial \bar{q}_1}{\partial t} + \lambda \frac{\partial \bar{q}_2}{\partial t} + \lambda^2 \frac{\partial \bar{q}_3}{\partial t} + \dots \right) \\
& + \omega_0^2 (\bar{q}_1 + \lambda \bar{q}_2 + \lambda^2 \bar{q}_3 + \dots) \\
& + \lambda (\bar{q}_1^2 + 2\lambda \bar{q}_1 \bar{q}_2 + \lambda^2 (2q_1 q_3 + q_1^2) + \dots) \\
& + \frac{eE}{m} = 0 . \tag{1.33}
\end{aligned}$$

Setting the coefficient of each power of λ equal to zero results in the following set of equations:

$$\text{For } \lambda^0; \quad \frac{\partial^2 \bar{q}_1}{\partial t^2} + \Gamma \frac{\partial \bar{q}_1}{\partial t} + \omega_0^2 \bar{q}_1 + \frac{eE}{m} = 0 \quad , \tag{1.34a}$$

$$\text{For } \lambda^1; \quad \frac{\partial^2 \bar{q}_2}{\partial t^2} + \Gamma \frac{\partial \bar{q}_2}{\partial t} + \omega_0^2 \bar{q}_2 + \bar{q}_1^2 = 0 \quad , \tag{1.34b}$$

$$\text{For } \lambda^2; \quad \frac{\partial^2 \bar{q}_3}{\partial t^2} + \Gamma \frac{\partial \bar{q}_3}{\partial t} + \omega_0^2 \bar{q}_3 + 2q_1 \bar{q}_2 = 0 \quad . \tag{1.34c}$$

.
.

.

The solution for \bar{q}_1 in (1.34a) is the same as that for the damped harmonic oscillator problem (Appendix B)

and results in amplitudes of

$$q_{1(\omega_1)}^0 = \frac{-eE_1^0}{m(\omega_0^2 - \omega_1^2 - i\Gamma\omega_1)} = \frac{-eE_1^0}{mD(\omega_1)} \quad (1.35a)$$

$$q_{1(\omega_2)}^0 = \frac{-eE_2^0}{m(\omega_0^2 - \omega_2^2 - i\Gamma\omega_1)} = \frac{-eE_2^0}{mD(\omega_2)} \quad (1.35b)$$

where $\bar{q}_{1(\omega_3)} = \bar{q}_{1(\omega_1)} + \bar{q}_{1(\omega_2)}$.

The complete form for \bar{q}_1 including its c.c. is

$$\begin{aligned} \bar{q}_{1(\omega_3)} = \frac{-e}{m} & \left[\frac{E_1^0 e^{i(k_1 \cdot r - \omega_1 t)}}{D(\omega_1)} + \frac{E_2^0 e^{i(k_2 \cdot r - \omega_2 t)}}{D(\omega_2)} \right. \\ & \left. - \frac{e}{m} \left[\frac{E_1^{0*} e^{-i(k_1 \cdot r - \omega_1 t)}}{D^*(\omega_1)} + \frac{E_2^{0*} e^{-i(k_2 \cdot r - \omega_2 t)}}{D^*(\omega_2)} \right] \right] \end{aligned} \quad (1.36)$$

From (1.26) it follows that the linear susceptibility at ω_3 due to the applied fields at ω_1 and ω_2 is

$$\chi_{(\omega_3)}^{(1)} = \frac{Ne^2}{m} \left[\frac{1}{D(\omega_1)} + \frac{1}{D(\omega_2)} \right] + \text{c.c.} \quad (1.37)$$

The solution for \bar{q}_2 in (1.34b) leads to the first nonlinear term in the induced polarization. \bar{q}_2 must have the same form as \bar{q}_1^2 and can be written as

$$\begin{aligned} \bar{q}_{2(\omega_3)} = \frac{q_2^0}{2} & e^{i[(k_1 - k_2) \cdot r - (\omega_1 - \omega_2)t]} \\ & + \frac{q_2^{0*}}{2} e^{-i[(k_1 - k_2) \cdot r - (\omega_1 - \omega_2)t]} \end{aligned} \quad (1.38)$$

plus other terms involving $2\omega_1$, $2\omega_2$ and $\omega_1 + \omega_2$.

As will be seen, only the first term involving $\exp[\pm i(\omega_1 - \omega_2)t]$ need be considered for describing $\chi_{\text{CARS}}^{(3)}$ although the term containing $\exp(\pm 2\omega_1)$ is necessary to account for the electronic resonance shown in figure 1.1e. Substitution of \bar{q}_2 along with its first and second time derivatives into (1.34b) gives

$$\begin{aligned} \bar{q}_2(\omega_3) = & \frac{-e^2 E_1^0 E_2^{0*} e^{i[(k_1 - k_2) \cdot r - (\omega_1 - \omega_2)t]}}{2m^2 [D(\omega_1 - \omega_2) D(\omega_1) D^*(\omega_2)]} \\ & + \frac{E_1^{0*} E_2^0 e^{-i[(k_1 - k_2) \cdot r - (\omega_1 - \omega_2)t]}}{D^*(\omega_1 - \omega_2) D^*(\omega_1) D(\omega_2)} \end{aligned} \quad (1.39)$$

where $D(\omega_1 - \omega_2) = \omega_0^2 - (\omega_1 - \omega_2)^2 - i\Gamma(\omega_1 - \omega_2)$.

From (1.39) it follows that the first nonlinear susceptibility at ω_3 is

$$\begin{aligned} \chi_{(\omega_3)}^{(2)} = & \frac{Ne^3}{2m^2} \left[\frac{1}{D(\omega_1 - \omega_2) D(\omega_1) D^*(\omega_2)} \right. \\ & \left. + \frac{1}{D^*(\omega_1 - \omega_2) D^*(\omega_1) D(\omega_2)} \right] . \end{aligned} \quad (1.40)$$

From the results of \bar{q}_1 (1.36) and \bar{q}_2 (1.39), \bar{q}_3 can now be found with (1.34c)

$$\begin{aligned}
\frac{\partial^2 \bar{q}_3}{\partial t^2} + \Gamma \frac{\partial \bar{q}_3}{\partial t} + \omega_0^2 \bar{q}_3 &= -2q_1 q_2 \\
&= \frac{-e^3 E_1^0 E_1^0 E_2^{0*} e^{-[(2k_1 - k_2) \cdot r - (2\omega_1 - \omega_2) t]}}{2m^3 [D^2(\omega_1) D(\omega_1 - \omega_2) D^*(\omega_2) D(2\omega_1 - \omega_2)]} \\
&\quad + \frac{E_1^{0*} E_1^{0*} E_2^0 e^{-[(2k_1 - k_2) \cdot r - (2\omega_1 - \omega_2) t]}}{(D^*(\omega_1))^2 D^*(\omega_1 - \omega_2) D(\omega_2) D^*(2\omega_1 - \omega_2)} \quad (1.41) \\
&+ \text{other terms involving: } 3\omega_1, 3\omega_2, 2\omega_1 + \omega_2, \\
&\quad \text{etc.}
\end{aligned}$$

Only the first term involving $\exp[\pm i(2\omega_1 - \omega_2)t]$ is needed to describe the susceptibility at $\omega_3 = 2\omega_1 - \omega_2$.

$$\begin{aligned}
\bar{q}_3(\omega_3) &= \frac{-e^3}{2m^3} \left[\frac{e^{i[(2k_1 - k_2) \cdot r - (2\omega_1 - \omega_2) t]}}{D^2(\omega_1) D(\omega_1 - \omega_2) D^*(\omega_2) D(2\omega_1 - \omega_2)} \right. \\
&\quad \left. + \frac{e^{-i[(2k_1 - k_2) \cdot r - (2\omega_1 - \omega_2) t]}}{(D^*(\omega_1))^2 D^*(\omega_1 - \omega_2) D(\omega_2) D^*(2\omega_1 - \omega_2)} \right] \quad (1.42)
\end{aligned}$$

Using the results for $\bar{q}_3(\omega_3)$ (1.42) and the expressions for $\chi_{(\omega)}^{NL}$ (1.26, 1.27), the nonlinear susceptibility at ω_3 is

$$3\chi_{(\omega_3)}^{(3)} = \frac{Ne^4}{m^3} \frac{1}{D^2(\omega_1) D(\omega_1 - \omega_2) D^*(\omega_2) D(2\omega_1 - \omega_2)} \quad (1.43)$$

This form for $\chi_{\text{CARS}}^{(3)}$ explicitly shows the resonance denominators which account for electronic 3WM and electronic enhanced CARS spectra. The $D_{(\omega_1)}$ factor gives rise to processes involving one photon resonances in ω_1 (Figure 1-d,h), and likewise the $D_{(2\omega_1-\omega_2)}$ factor accounts for one photon resonances in ω_3 (Figure 1-c,g). If no electronic resonances are possible, then the $D_{(\omega_1-\omega_2)}$ factor determines the behavior of $\chi_{(\omega_3)}^{(3)}$ (normal CARS) since the other denominator terms are slowly varying. The following section describes an alternative method of deriving $\chi_{(\omega_3)}^{(3)}$ in which only a vibrational resonance is assumed.

The nonlinear response of the dipole can also be accounted for by introducing the nonlinearity into the driving force [17] instead of the oscillator response. The susceptibility may be expressed as an expansion of the polarizability, α , as follows

$$\chi = N\alpha = N(\alpha_0 + q(\frac{\partial\alpha}{\partial q})_0 + \dots) \quad (1.44)$$

where N is the total number of dipoles induced at a given frequency. The oscillator response may now be written as

$$\frac{\partial^2 \bar{q}}{\partial t^2} + \Gamma \frac{\partial \bar{q}}{\partial t} + \omega_0^2 \bar{q} = \frac{F}{m} \quad (1.45)$$

F is the force acting on the system of U energy,

$$F = -\frac{\partial U}{\partial q} = -\frac{\partial(-\frac{1}{2}\alpha E^2)}{\partial q} = \left(\frac{\partial \alpha}{\partial q}\right) E^2 \quad (1.46)$$

and (1.45) becomes

$$\frac{\partial^2 q}{\partial t^2} + \Gamma \frac{\partial q}{\partial t} + \omega_0^2 q = \frac{1}{2m} \left(\frac{\partial \alpha}{\partial q}\right) E^2 . \quad (1.47)$$

Fields at frequencies ω_1 and ω_2 are present and E is assumed to have the same complex form as before.

$$E^2 = \frac{E_1^0 E_2^{0*}}{4} e^{i[(k_1 - k_2) \cdot r - (\omega_1 - \omega_2)t]} + \text{c.c.} \quad (1.48)$$

q is assumed to have the same form as E^2 and

$$q = \frac{q^0}{2} e^{i[(k_1 - k_2) \cdot r - (\omega_1 - \omega_2)t]} + \text{c.c.} \quad (1.49)$$

$$\begin{aligned} \frac{\partial q}{\partial t} &= -i(\omega_1 - \omega_2) \frac{q^0}{2} e^{i[(k_1 - k_2) \cdot r - (\omega_1 - \omega_2)t]} \\ &\quad + i(\omega_1 - \omega_2) \text{c.c.} \end{aligned} \quad (1.50)$$

$$\begin{aligned} \frac{\partial^2 q}{\partial t^2} &= -(\omega_1 - \omega_2)^2 \frac{q^0}{2} e^{i[(k_1 - k_2) \cdot r - (\omega_1 - \omega_2)t]} - (\omega_1 - \omega_2)^2 \text{c.c.} \end{aligned} \quad (1.51)$$

Substitution of (1.49), (1.50) and (1.51) into (1.47) gives

$$\begin{aligned}
& [-(\omega_1 - \omega_2)^2 - i\Gamma(\omega_1 - \omega_2) + \omega_0^2] \frac{q^0}{2} e^{i[(k_1 - k_2) \cdot r - (\omega_1 - \omega_2)t]} \\
& + [-(\omega_1 - \omega_2)^2 + i\Gamma(\omega_1 - \omega_2) + \omega_0^2] \frac{q^0}{2} e^{-i[(k_1 - k_2) \cdot r - (\omega_1 - \omega_2)t]} \\
& = \frac{1}{2m} \left(\frac{\partial \alpha}{\partial q} \right) \left[\frac{E_1^0 E_2^{0*}}{4} e^{i[(k_1 - k_2) \cdot r - (\omega_1 - \omega_2)t]} \right. \\
& \left. + \frac{E_1^{0*} E_2^0}{4} e^{-i[(k_1 - k_2) \cdot r - (\omega_1 - \omega_2)t]} \right] . \tag{1.52}
\end{aligned}$$

Again, only terms involving the frequency difference $\pm i(\omega_1 - \omega_2)$ have been retained. Solving for q ,

$$q = \frac{1}{4m} \left(\frac{\partial \alpha}{\partial q} \right) \left[\frac{E_1^0 E_2^{0*} e^{i[(k_1 - k_2) \cdot r - (\omega_1 - \omega_2)t]} + \text{c.c.}}{D(\omega_1 - \omega_2)} \right] \tag{1.53}$$

From (1.44) the nonlinear susceptibility due to ω_1 and ω_2 is

$$\chi_{(\omega_1, \omega_2)}^{NL} = Nq \left(\frac{\partial \alpha}{\partial q} \right) . \tag{1.54}$$

The polarization induced at $\omega_3 = 2\omega_1 - \omega_2$ can be expressed as

$$P_{(\omega_3)}^{(3)} = 3\chi_{(\omega_3)}^{(3)} E_1^2 E_2 = Nq \left(\frac{\partial \alpha}{\partial q} \right) E_1 \tag{1.55}$$

since q already contains $E_1 E_2$. The resulting form for the susceptibility is

$$3\chi_{(\omega_3)}^{(3)} = \frac{N}{m} \left(\frac{\partial \alpha}{\partial q} \right)^2 \frac{1}{D_{(\omega_1 - \omega_2)}} \quad (1.56)$$

Using the relationship between the differential optical cross section, $\frac{d\sigma}{d\Omega}$, and the changing polarizability [14]

$$\frac{d\sigma}{d\Omega} = \frac{\omega_2^2 q^2}{c^4} \left(\frac{\partial \alpha}{\partial q} \right)^2 \quad (1.57)$$

along with the assumption that the classical coordinate q may be quantized

$$q^2 = \frac{h}{2m\omega_0} \quad (1.58)$$

leads to the following semiclassical form for the susceptibility

$$3\chi_{(\omega_3)}^{(3)} = \frac{2Nc^4}{h\omega_2^4} \left(\frac{d\sigma}{d\Omega} \right) \left(\frac{\omega_0}{D_{(\omega_1 - \omega_2)}} \right) \quad (1.59)$$

This expression can be compared to the previous form for $\chi_{(\omega_3)}^{(3)}$ (1.43) by noting that the other denominator resonance terms are now included in $\frac{d\sigma}{d\Omega}$, the line strength factor.

In actuality the number density, N , in (1.59) is more properly expressed as a difference, $N_n - N_k$. If all of the molecules are in the n level a $(+N_n)$ factor appears in $\chi_{(\omega_3)}^{(3)}$ while if all of the molecules are in the k level a

$(-N_k)$ would appear in $\chi_{(\omega_3)}^{(3)}$. Making this subtraction along with

$$\omega_0 = \omega_{nk}$$

$$\left(\frac{d\sigma}{d\Omega}\right) = \left(\frac{d\sigma}{d\Omega}\right)_{nk}$$

and

$$D_{(\omega_1-\omega_2)} = \omega_{nk}^2 - (\omega_1-\omega_2)^2 - i\Gamma_{nk}(\omega_1-\omega_2)$$

where ω_{nk} is a Raman vibrational frequency between states n and k , Γ_{nk} is the full width at half maximum (FWHM) and $\left(\frac{d\sigma}{d\Omega}\right)_{nk}$ is the Raman cross section or line strength, gives

$$\chi_{\text{CARS}} = \frac{2(N_n - N_k)c^4}{h\omega_2^4} \left(\frac{d\sigma}{d\Omega}\right)_{nk} \frac{\omega_{nk}}{\omega_{nk}^2 - (\omega_1 - \omega_2)^2 - i\Gamma_{nk}(\omega_1 - \omega_2)}. \quad (1.60)$$

Equation (1.60) points out an important feature of CARS. Since the number density difference $(N_n - N_k)$ depends on the vibrational and rotational temperatures, it is possible to extract this information from a CARS spectrum. Applications of this type have been made for combustion diagnostics [10], glowing discharges [5], and supersonic molecular beams [18, 24].

The above expression may be simplified by factoring the denominator, making a few approximations and dividing by ω_{nk} as follows:

$$\chi_{\text{CARS}} = \frac{2(N_n - N_k) c^4}{h\omega_2^4} \left(\frac{\partial \sigma}{\partial \Omega} \right)_{nk} \frac{\omega_{nk}}{[\omega_{nk} - (\omega_1 - \omega_2)] [\omega_{nk} + (\omega_1 - \omega_2)] - i\Gamma_{nk}(\omega_1 - \omega_2)}$$

$$\omega_{nk} + (\omega_1 - \omega_2) \approx 2\omega_{nk}$$

$$\Gamma_{nk}(\omega_1 - \omega_2) \approx i\Gamma_{nk}(\omega_{nk})$$

$$\chi_{\text{CARS}} = \frac{(N_n - N_k) c^4}{h\omega_2^4} \left(\frac{\partial \sigma}{\partial \Omega} \right)_{nk} \frac{1}{(\omega_{nk} - (\omega_1 - \omega_2) - i\gamma_{nk})} \quad (1.61)$$

where $\gamma_{nk} = \frac{\Gamma_{nk}}{2}$.

A quantum mechanical derivation of χ_{CARS} , involving the computation of the average molecular dipole moment resulting from the third power of the electric fields, gives a similar expression [8]

$$\chi_{\text{CARS}} = \frac{(N_n - N_k) n_1 c^4}{2hn_2\omega_2^4} \left(\frac{d\sigma}{d\Omega} \right)_{nk} \frac{1}{\omega_{nk} - (\omega_1 - \omega_2) - i\gamma_{nk}} \quad (1.62)$$

where n_1 and n_2 are the indices of refraction for frequencies ω_1 and ω_2 respectively, and γ_{nk} is the half width at half maximum (HWHM) for the Raman transition.

From (1.61) it can be seen that χ_{CARS} contains real, χ' , and imaginary, χ'' , parts. The bulk response of all of the electrons to the applied fields contributes a nonresonant term, χ_{NR} , which is also real.

$$\chi_{\text{CARS}} = \chi' + \chi'_{\text{NR}} + \chi'' \quad (1.63)$$

$$\chi' = \frac{(N_n - N_k) c^4}{h \omega_2^4} \left(\frac{\partial \sigma}{\partial \Omega} \right)_{nk} \frac{\omega_{nk} - (\omega_1 - \omega_2)}{[\omega_{nk} - (\omega_1 - \omega_2)]^2 + \gamma_{nk}^2} \quad (1.64)$$

$$\chi'' = \frac{(N_n - N_k) c^4}{h \omega_2^4} \left(\frac{\delta \sigma}{\delta \Omega} \right)_{nk} \frac{i \gamma_{nk}}{[\omega_{nk} - (\omega_1 - \omega_2)]^2 + \gamma_{nk}^2} \quad (1.65)$$

The above expressions will be returned to later for consideration of the CARS lineshape profiles. It should be noted, however, that the expression for χ'' is essentially the stimulated Raman susceptibility with the number density difference $(N_n - N_k)$ replaced with the number density of the initial state, N_k [14]

$$\chi''_{\text{RAMAN}} = \frac{N_k c^4}{h \omega_2^4} \left(\frac{\partial \sigma}{\partial \Omega} \right)_{nk} \frac{i \gamma_{nk}}{[\omega_{nk} - (\omega_1 - \omega_2)]^2 + \gamma_{nk}^2} \quad (1.66)$$

The relationship between the CARS susceptibility, χ_{CARS} , and the detected power of the CARS signal, P_3 , is discussed in the following section.

The selection rules for a CARS transition have been shown to be the same as for the Raman experiment [8, 19]. This is not surprising since the CARS process, Figure (1.1f) can be thought of as two simultaneous Raman experiments (Stokes and anti-Stokes) with all transitions being Raman allowed.

1.E CARS Intensities and Lineshapes

The average intensity of the CARS beam can be determined from the magnitude of the Poynting vector \bar{S} , by [15]

$$\bar{S} = \bar{E} \times \bar{H} \quad (1.67)$$

$$I = |\bar{S}| \quad (1.68)$$

$$I_3 = |\bar{S}_3| = \frac{cn_3}{8\pi} |\bar{E}_3|^2 \quad (1.69)$$

where n_3 is the index of refraction at ω_3 and \bar{E}_3 is the electric field vector at ω_3 . The wave equation (1.21) can be solved for E_3^0 by integration over the interaction length, ℓ , assuming plane waves travelling in the z direction [8]

$$E_3^0 = \frac{2\pi\omega_3}{n_3c} \chi_{\text{CARS}} E_1^2 E_2^* [e^{i\Delta k \ell} - 1] \quad (1.70)$$

The above expression results from choosing the orientations (polarization) of \bar{E}_1 and \bar{E}_2 parallel to each other and orthogonal to z . Δk is the phase matching condition, figure (1.2), with

$$\Delta k = 2k_1 - k_2 - k_3 \quad (1.71)$$

The phase matching condition, $\Delta k = 0$, can be thought of as a consequence of the conservation of energy and momentum in the interaction region. Photons of frequency ω and

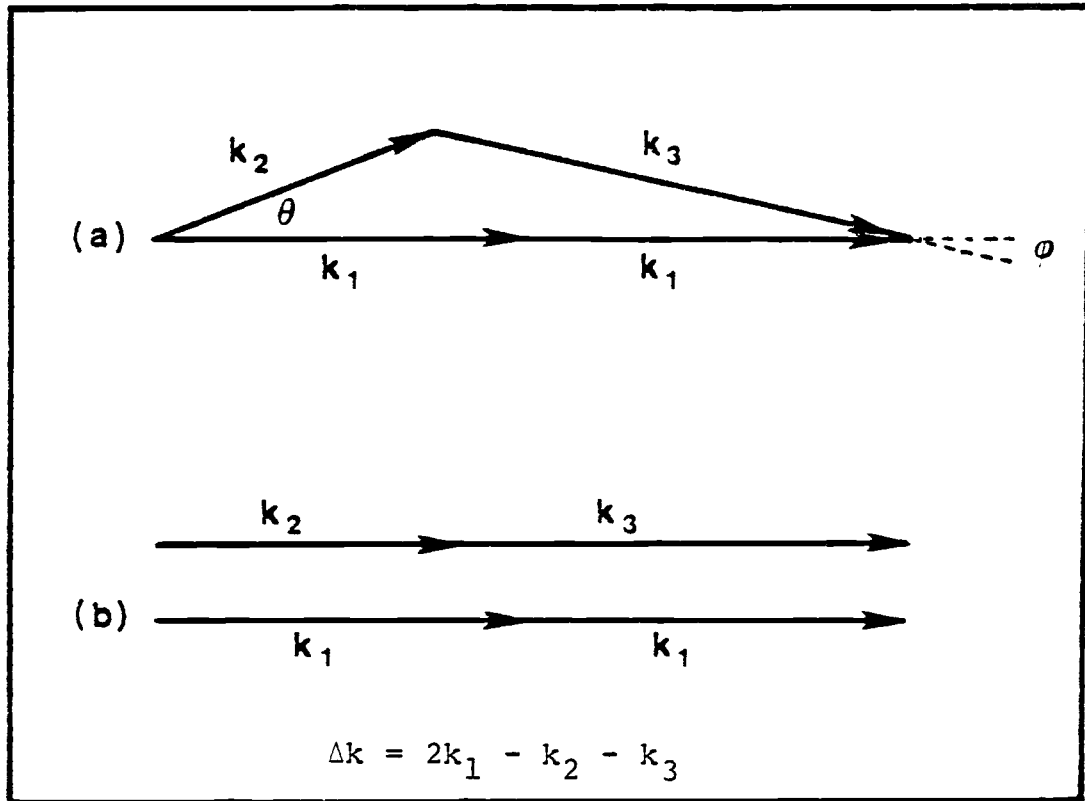


Figure 1.2. Orientation of the wave vectors for phase matching ($\Delta k = 0$). (a) shows the general case for $n_1 \neq n_2 \neq n_3$ (liquids and solids). (b) depicts the special case for gases where $n_1 = n_2 = n_3$ and all beams are colinear.

wave vector k propagate with energy $h\omega$ and momentum hk . In CARS, conservation of energy results in

$$\omega_3 = 2\omega_1 - \omega_2$$

and invoking conservation of momentum leads to

$$k_3 = 2k_1 - k_2 . \quad (1.72)$$

Amplification at ω_3 will only occur when this phase matching is met. Otherwise, the waves generated at ω_3 are incoherent and cannot beat with the driving force. The wave vector can be related to the index of refraction by [15]

$$k = \frac{\omega}{v} = \frac{n\omega}{c} \quad (1.73)$$

where v is the phase velocity. Substitution of (1.73) into (1.72) gives

$$n_3\omega_3 = 2n_1\omega_1 - n_2\omega_2 . \quad (1.74)$$

For gases, the index of refraction is nearly constant thus

$$n_1 \approx n_2 \approx n_3 \quad (1.75)$$

and from (1.74) proper phase matching is achieved with all beams colinear. In condensed materials, however, dispersion negates (1.75) and requires the ω_1 and ω_2 beams to cross at a small angle, θ , while ω_3 exits at a small angle ϕ .

The substitution of (1.70) back into the wave equation along with the relationship (1.69) gives the average intensity for ω_3 as

$$I_3 = \frac{256\pi^4 \omega_3^2}{n_1^2 n_2^2 n_3^2 c^4} |\chi_{\text{CARS}}|^2 I_1^2 I_2^2 \ell^2 \left(\frac{\sin(\Delta k \ell / 2)}{\Delta k \ell / 2} \right)^2. \quad (1.76)$$

For proper phase matching, $\Delta k = 0$, the last term equals 1, and the CARS intensity is seen to be proportional to the square of the interaction length (and to the square of the molecular density). The advantage of using high peak powered lasers is apparent from the quadratic and linear dependence on the intensities of ω_1 and ω_2 respectively.

For focused Gaussian beams, the above expression can be expressed in terms of the measurable power at ω_3 , P_3 , by [8]

$$P_3 \approx \left(\frac{2}{\lambda} \right)^2 \frac{256\pi^4 \omega_3^2}{n_1^2 n_2^2 n_3^2 c^4} |\chi_{\text{CARS}}|^2 P_1^2 P_2 \quad (1.77)$$

where λ is the average wavelength of the three beams, and $\Delta k = 0$. The calculation of CARS lineshapes and relative intensities results from (1.77) and the following relationship is used

$$P_3 \propto |\chi_{\text{CARS}}|^2 \quad (1.78)$$

assuming the average powers of ω_1 and ω_2 are unchanging during an experiment. As was mentioned earlier, the preceding discussion assumes idealized monochromatic laser sources for ω_1 and ω_2 . The CARS lineshape profile is then determined only by the linewidth of the Raman transition, Γ_{nk} . In reality, the CARS lineshape may be broadened by laser source linewidths greater than Γ_{nk} as well as by laser phase and amplitude fluctuations broadening the driving force. The following sections deal with these effects. The discussion begins by examining "pure" CARS lineshapes using (1.61) and introducing a convolution later to account for broadened laser sources.

1.F CARS Lineshapes

The lineshape of a single resonance is perhaps best seen by rewriting (1.61) in terms of a resonance variable, $\partial\omega = \omega_{kn} - (\omega_1 - \omega_2)$

$$\chi_{\text{CARS}} = C \frac{\partial\omega + i\Gamma}{\partial\omega + \Gamma^2} + \chi'_{\text{NR}} \quad (1.79)$$

where C is a constant. The real and imaginary parts of χ_{CARS} (neglecting C) are

$$\chi' = \frac{\partial\omega}{\partial\omega^2 + \Gamma^2} + \chi'_{\text{NR}} \quad (1.80)$$

$$\chi'' = \frac{i\Gamma}{\partial\omega^2 - \Gamma^2} \quad (1.81)$$

For a pure substance, χ'_{NR} is very small compared to the resonance term and may be neglected. Plots of χ' and χ'' as a function of $\partial\omega/\Gamma$ are shown in Figure (1.3). χ'' has a Lorentzian lineshape much like the absorption coefficient and χ' has a dispersion lineshape as does the index of refraction. From (1.78) the CARS intensity is

$$P_{\text{CARS}} \propto |\chi_{\text{CARS}}|^2 = |\chi'|^2 + |\chi''|^2, \quad (1.82)$$

and a plot of the square of the susceptibility has the same lineshape as χ'' for χ_{NR} equal to 0. For dilute samples the effect of χ_{NR} becomes apparent. As the nonresonant contribution increases, the CARS lineshape changes from a Lorentzian to a dispersion curve, figure (1.4), and the peak maximum shifts slightly. This effect places a limit on the detection of a CARS signal at about 1% for dilute liquids [20] and 10 ppm for gaseous mixtures [21]. It is possible, however, to overcome this limitation by enhancing χ_{CARS} with added electronic resonances (see equation 1.43). This technique is applied to NO_2 in Chapter 2 [37] and has also been demonstrated for I_2 [42]. Various schemes for reducing χ_{NR} by employing polarization [11] and interference [12] techniques have not been convenient in practice and do not offer the advantage of increasing the resonant signal. The remainder of this chapter deals with calculating the total χ_{CARS} for a molecular gas assuming only vibrational resonances.

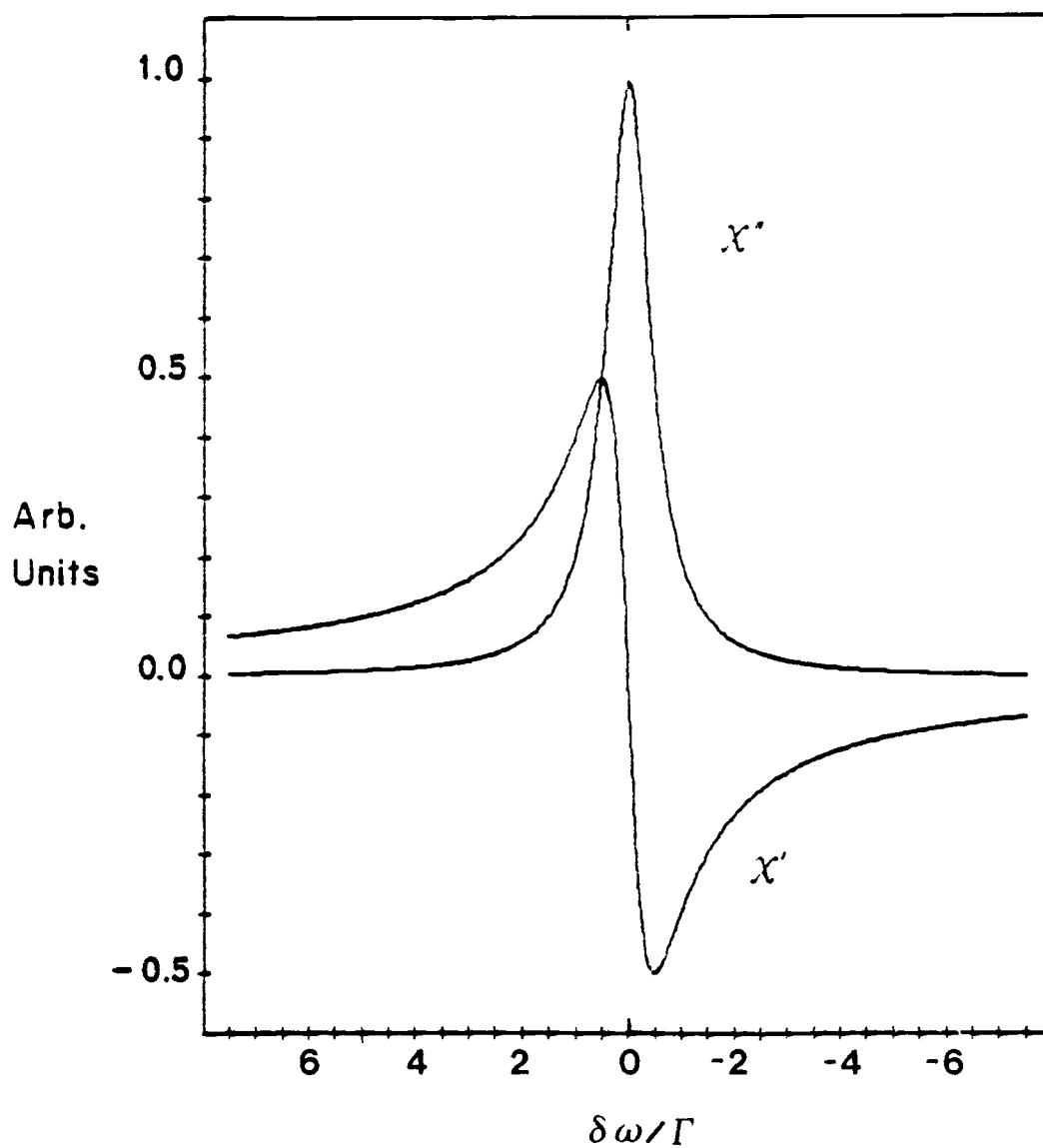


Figure 1.3. Plots of the real, χ' , and imaginary, χ'' , parts of the susceptibility for an isolated resonance.

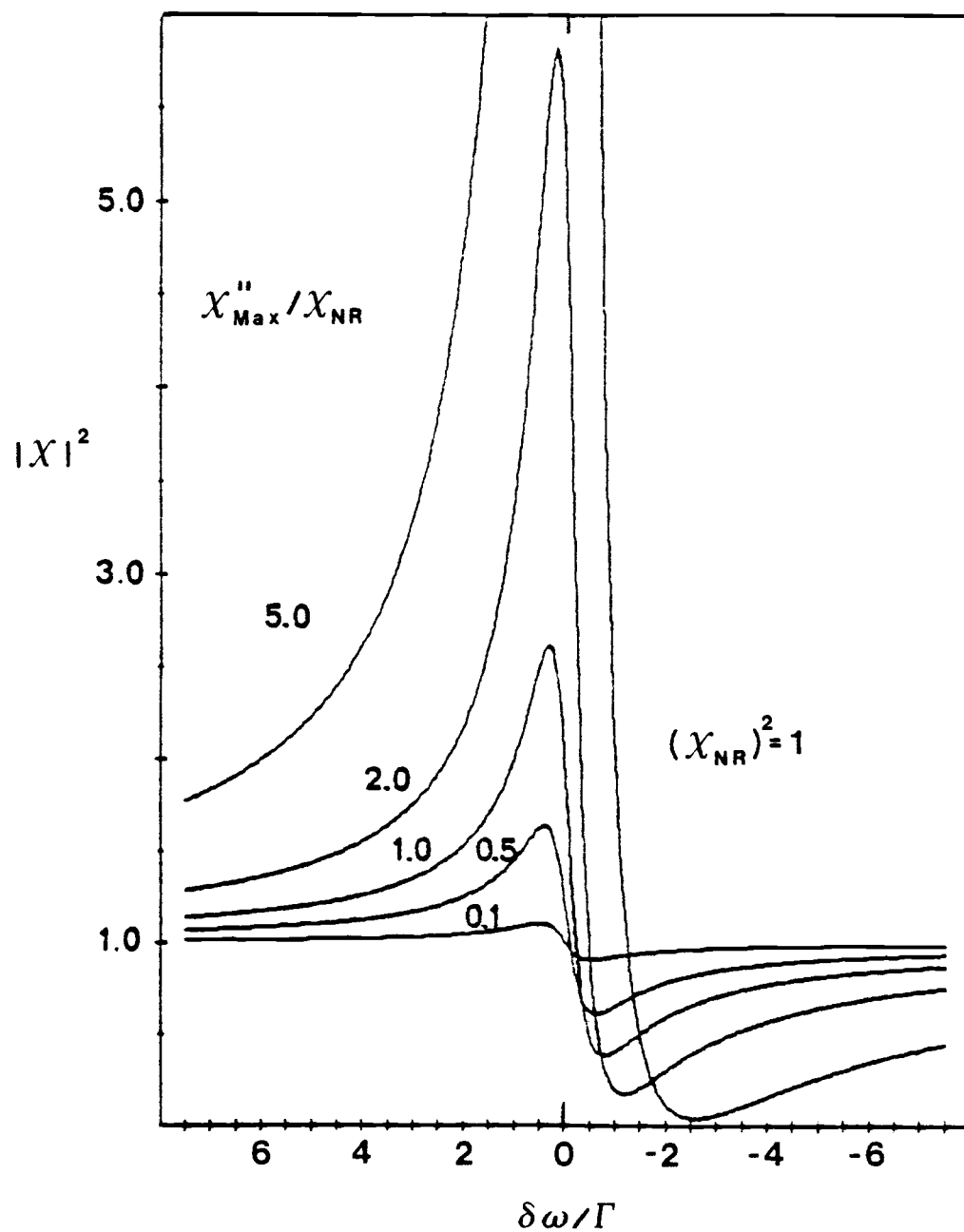


Figure 1.4. Effects of the nonresonant, χ_{NR} , contribution to the lineshape of total squared susceptibility, $|\chi|^2 = |\chi' + \chi'' + \chi'_{NR}|^2$.

The CARS spectrum of a molecular gas is composed of many resonance terms as $\omega_1 - \omega_2$ is scanned through various vibration-rotation transitions. The total third order susceptibility must be summed over all allowed transitions, nk,

$$\chi_{(\omega_3)}^{(3)} = \chi_{NR} + \sum_{nk} \chi_{CARS} \quad (1.83)$$

Appendix C contains a Fortran program, written for a PDP-11, that calculates χ_{CARS} for diatomic gases. The resolution of an observed CARS spectrum is limited by the linewidths of the laser sources since they are usually larger than the Raman transition linewidths, Γ_{nk} . The program in Appendix C calculates an "unconvoluted" CARS spectrum and the effect of laser linewidth is neglected. Figure (1.5) shows an "unconvoluted" CARS spectrum for O_2 calculated by the program listed in Appendix C. Γ_{nk} was assumed to be 0.03 cm^{-1} [19] and the rotational and vibrational temperatures (T_R and T_V) were 300K. This would closely resemble the CARS spectrum of O_2 if both laser sources had linewidths $\leq 0.01 \text{ cm}^{-1}$. An actual CARS spectrum of O_2 is shown in Figure 1.6. This spectrum was recorded with dye laser, $\Delta\omega_2$, and ND-YAG laser, $\Delta\omega_1$, linewidths of 0.15 and 0.03 cm^{-1} respectively. In order to calculate a spectrum resembling figure (1.6), the expression for the power at ω_3 (1.77) must be convoluted over the laser lineshapes.

Yuratich [22] has recently discussed the effects of laser lineshapes on CARS spectra and concludes that a

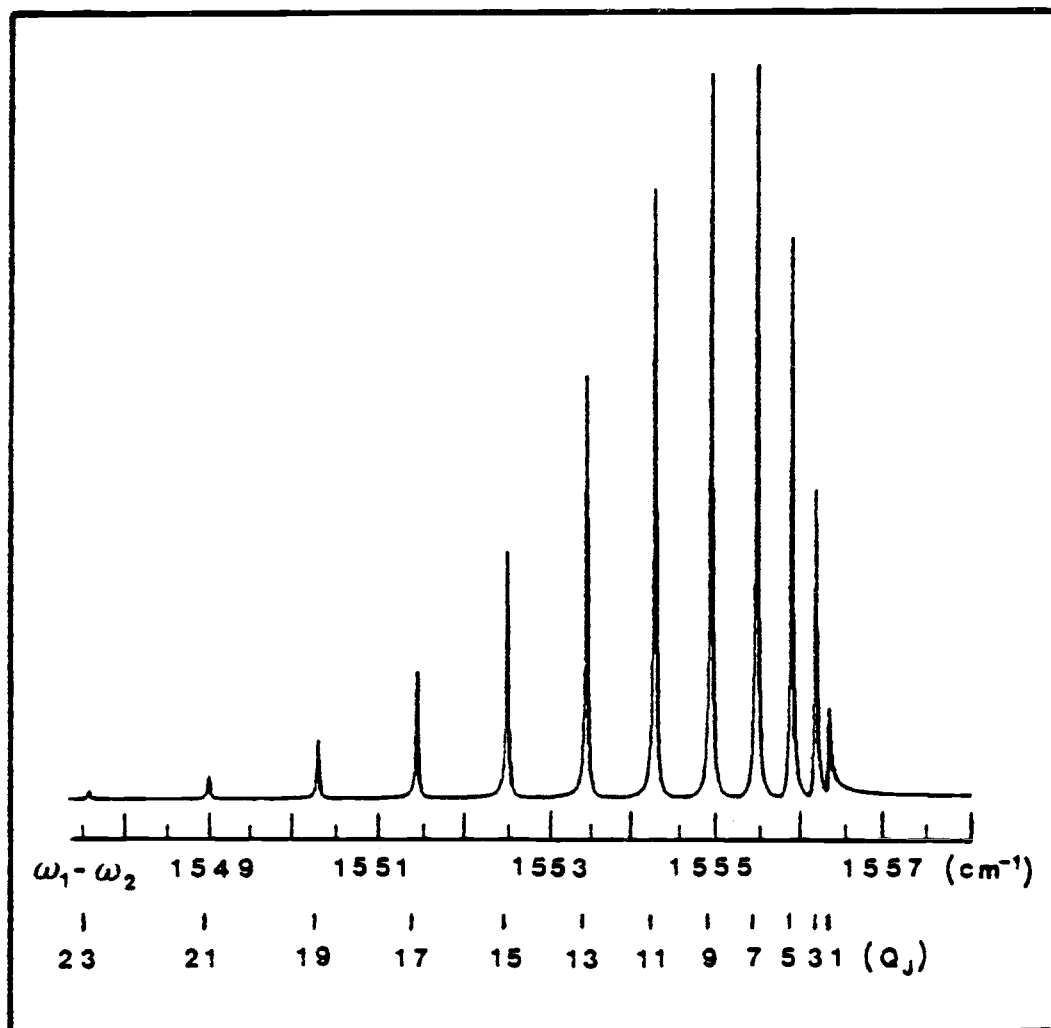


Figure 1.5. Calculated "unconvoluted" CARS spectrum of the Q-branch ($\Delta J = 0$) of O_2 gas at 300K. $\Gamma_{nk} = 0.03 \text{ cm}^{-1}$, resolution increment is 0.0005 cm^{-1} . Assignments are indicated below the frequency scale.

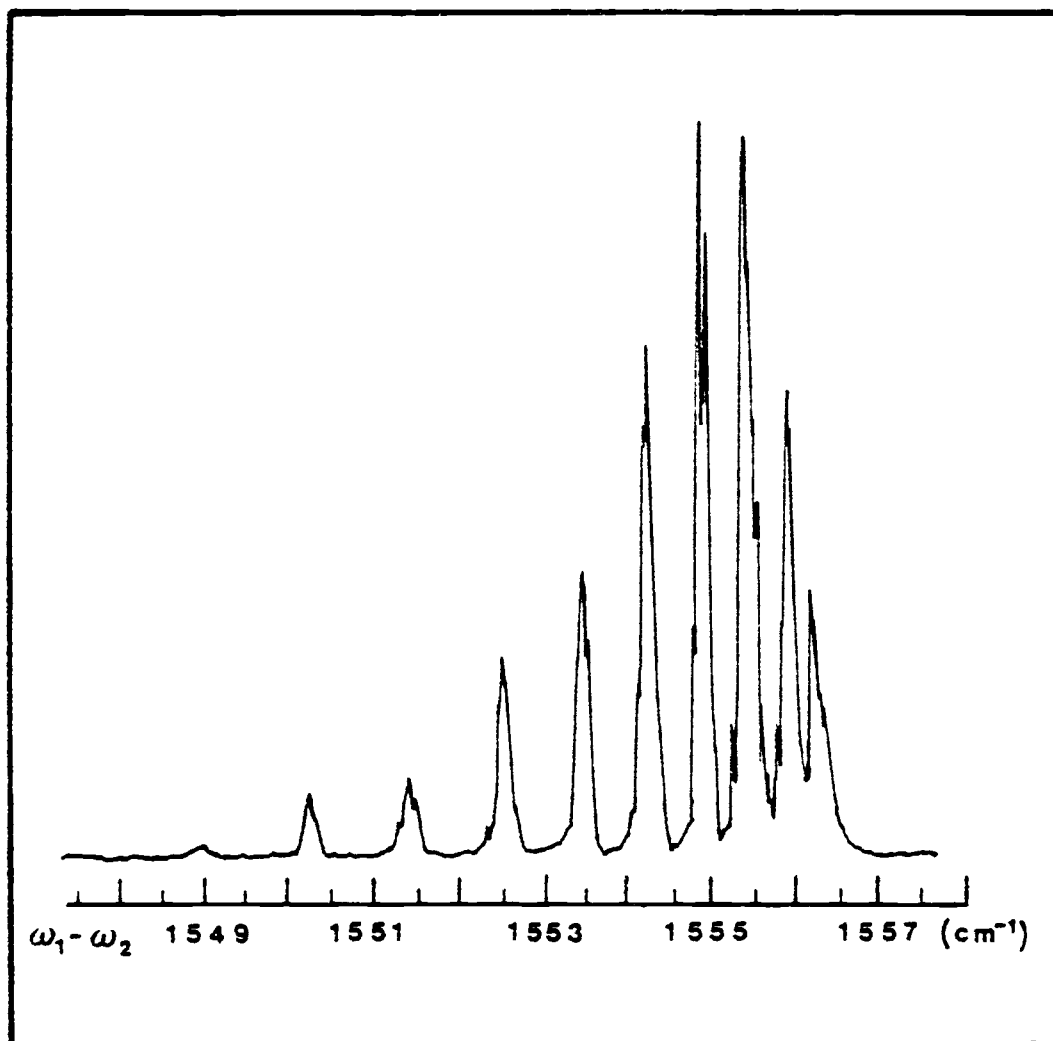


Figure 1.6. Observed spectrum of the Q-branch ($\Delta J = 0$) of O_2 gas at 300K. $\Delta\omega_1 \approx 0.03 \text{ cm}^{-1}$, $\Delta\omega_2 \approx 0.15 \text{ cm}^{-1}$.

convolution over a single lineshape function, that includes contributions from all broadening sources, is adequate. The particular lineshape function to be used should be arrived at by experiment. In the present work, the analytical lineshape function is chosen to be

$$L = F \cdot \text{Gaus} + (1-F) \cdot \text{Lor} \quad (1.84)$$

where F is a fraction, and Gaus and Lor are normalized Gaussian and Lorentzian lineshape profiles, respectively.

$$\text{Gaus} = \frac{2\sqrt{\ln 2}}{\Delta\omega\sqrt{\pi}} e^{-\left[\frac{(\omega^0 - \omega) 2\sqrt{\ln 2}}{\Delta\omega}\right]^2} \quad (1.85)$$

$$\text{Lor} = \frac{\Delta\omega}{2\pi} \frac{1}{(\omega^0 - \omega)^2 + \left(\frac{\Delta\omega}{2}\right)^2} \quad (1.86)$$

$\Delta\omega$ is the observed CARS linewidth (FWHM) for an isolated band. The advantage of using this sort of lineshape is that $\Delta\omega$ can be experimentally determined and F can then be used as a fitting parameter. If $F=1$, corresponding to a pure Gaussian lineshape the contributions to $\Delta\omega$ would be

$$\Delta\omega_G = (\Delta\omega_1^2 + \Delta\omega_2^2 + \Gamma_A^2 + \Gamma_D^2)^{\frac{1}{2}} \quad (1.87)$$

where $\Delta\omega_1$ and $\Delta\omega_2$ are the time averaged widths of the YAG and dye laser beams, and Γ_A and Γ_D are the broadenings due to laser amplitude fluctuations and Doppler broadening. Similarly, an expression for a pure Lorentzian lineshape would be

$$\Delta\omega_L = (\Delta\omega_1 + \Delta\omega_2 + \Gamma_{Ph} + \Gamma_{Pr}) \quad (1.88)$$

with Γ_{ph} and Γ_{pr} broadening due to phase fluctuations and pressure broadening, respectively. The major source of broadening is due to $\Delta\omega_2 \approx 0.15 \text{ cm}^{-1}$ while $\Delta\omega_1 \approx 0.03 \text{ cm}^{-1}$. From (1.84), (1.87) and (1.88) the experimental linewidth may be approximated by

$$\begin{aligned} \Delta\omega &\approx (F) \Delta\omega_G + (1-F) \Delta\omega_L \\ \Delta\omega &\approx F(\Delta\omega_1^2 + \Delta\omega_2^2 + \Gamma_A^2 + \dots)^{\frac{1}{2}} \\ &\quad + (1-F)(\Delta\omega_1 + \Delta\omega_2 + \Gamma_P + \dots) \end{aligned} \quad (1.89)$$

Using the above expression with $F = 0.75$ and $\Gamma_A, \Gamma_P,$ etc. = 0, gives

$$\Delta\omega \approx 0.16 \text{ cm}^{-1} .$$

This can be compared to the measured width of ω_3 at about 0.17 cm^{-1} . It is found in these calculations, that a value for the natural Raman linewidth, Γ_{nk} , less than 0.03 cm^{-1} produces negligible effects on the final convoluted spectrum. Consequently, the largest possible value was chosen to minimize the computational time since 5 or 6 values of χ_{CARS} are calculated per Γ_{nk} . Using the above values for F and $\Delta\omega$, the room temperature convoluted CARS spectrum was calculated for O_2 and is reproduced in Figure (1.7) along with experimental results.

The convolution is carried out with the Fortran program listed in Appendix C and involves scanning the chosen

lineshape function across the unconvoluted susceptibilities and calculating the intensity contribution from each resolution increment within the lineshape envelope. The ability to reproduce the experimental spectra demonstrates the possibility of determining the vibrational and rotational temperatures with this lineshape analysis procedure.

The impetus for performing the above calculations was provided by the development, by Peter Huber-Wälchli, of CARS spectra of supersonic molecular beams [18]. In these experiments, a gas at fairly high pressure (~ 1 atm or greater) is allowed to expand through a small orifice (~ 60 μm) into a region of low pressure and high pumping speed. The CARS spectra of the gas in the free jet region shows a dramatic rotational cooling effect as the rotational energy is degraded into kinetic energy [23]. The populations of the upper rotational states are depleted and most of the CARS intensity occurs in the lowest 2 or 3 rotational states. Although the effective pressure in the molecular beam is very low (< 1 torr) the piling up of intensity into only a couple of rotational states makes detection possible. Using the lineshape analysis discussed above for static conditions at room temperature to find F and $\Delta\omega_1$ lower temperature spectra can be calculated by varying T_V and T_R . For pure N_2 and O_2 Peter Huber-Wälchli has estimated rotational cooling down to 20K in the molecular beam [18, 24]. When an added carrier gas is present (Ar) to help

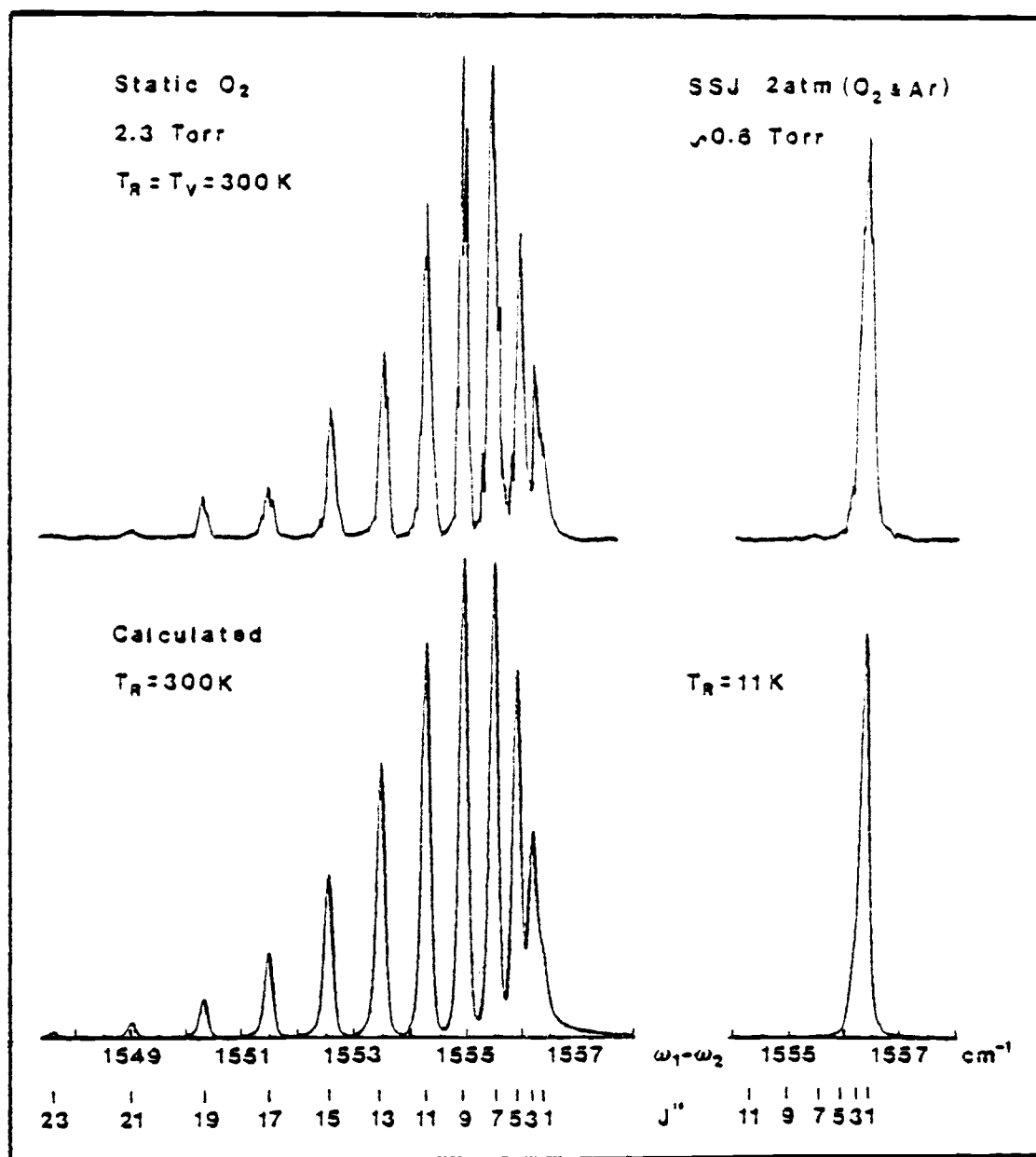


Figure 1.7. Observed (upper traces) and calculated (lower traces) spectra of the Q-branch of O₂ gas. The spectra on the left correspond to room temperature conditions (300K) while those on the right show the rotational cooling obtained when O₂ is expanded into a supersonic molecular beam.

carry away kinetic energy, rotational cooling down to $\sim 10\text{K}$ is possible [24]. Figure (1.7) shows experimental and calculated supersonic molecular beam CARS spectra of O_2 where such cooling is apparent. These types of calculations are also applicable at higher temperatures but the populating of many higher states places a limit on detection.

Another way of doing CARS, as mentioned earlier, is to replace the tunable ω_2 source with a broadband dye laser. Under these conditions, it is possible to acquire a complete CARS spectrum in one laser flash using an optical multi-channel analyzer (OMA) as a detector. The driving force at ω_3 picks out the components, ω_2 , in the broad band source which satisfy the resonance conditions. Resolution of broadband CARS is essentially limited by the dispersive device used. Lineshape analysis of broadband CARS spectra would need to include the intensity distribution of the broadband source along with proper slit functions for the dispersive element and detector.

The experimental arrangements used in this work are described in the following chapter.

CHAPTER 2

EXPERIMENTAL

2.A Basic Experimental Configuration

The basic experimental arrangement used in these studies is schematically diagrammed in Figure (2.1). The primary source of radiation is provided by a Nd-YAG-oscillator-amplifier (Quanta-Ray model DCR-1A) lasing at 1064 nm (ω_0) and producing a "doughnut" mode beam. A glass filter (Schott RG 780) removes the unwanted broadband visible flashlamp radiation. A 25 mm KD*P type II crystal doubles the frequency of the YAG and yields typically 100 mJ at 532 nm (ω_1) in a 10 nsec pulse at a rate of 10 Hz. A quartz prism separates the fundamental and first harmonic. The ω_0 , exiting from this prism is passed through a second KD*P type II crystal (30 mm), and the ~ 30 mJ of 532 nm radiation produced serves to pump and amplify a dye laser. The left-over ω_0 beam is reflected away with a dichroic beam splitter into an optical dump. The primary ω_1 beam is expanded with a 1.8X telescope to counter self focusing and thereby reduce damage to the optical elements. The ω_1 beam is optically delayed, ~ 8 nsec, so as to arrive at the sample the same instant as the dye laser beam, ω_2 . ω_1 and ω_2 are combined and made colinear with a dichroic beam splitter which reflects ω_1 and passes ω_2 . This beam

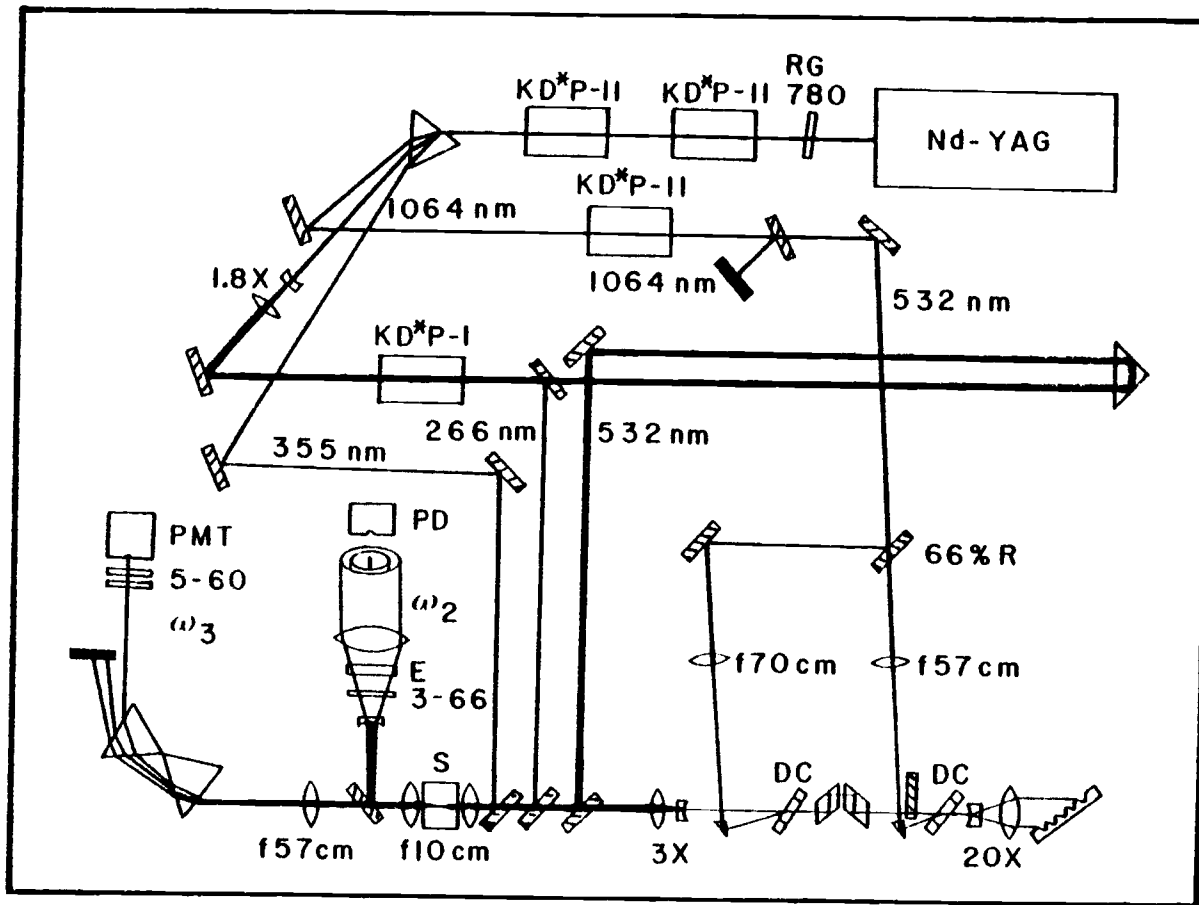


Figure 2.1. Schematic diagram of the CARS spectrometer.

splitter is housed in a sturdy mirror mount fitted with micrometer adjustment screws for fine adjustment of the beam overlap in the sample. The ω_1 and ω_2 beams are focused into the sample region and recollimated with two 100 mm focal length lenses. Most of the ω_1 and ω_2 intensity is reflected away with one or more dichroic beam splitters coated to reflect wavelengths greater than 500 nm and pass blue light, ω_3 . These reflected beams can be used to analyze the ω_1 and ω_2 linewidths and monitor the changing ω_2 frequency by passing them through appropriate Fabry-Perot etalons. ω_1 and ω_2 are further removed with various Corning filters (5-57, 5-58, 5-59, 5-60), prisms and diffraction gratings. The ω_3 beam is sensed with a photomultiplier detector (RCA 1P28A) operated at -400 to -800 VDC. The output pulse is stretched to 100 μ sec, amplified and processed with a gated pulse integrator (Evans Associates model 4130) with RC time constants from 0.5-5 sec. The integrator output is sent to one pen of a dual pen strip chart recorder (Linear Instruments model 385) which is driven by the same pulse train which runs the dye laser scan. The dye laser output is monitored by a photodiode (HP 4203) behind a pinhole over which the changing Fabry-Perot interference fringe pattern moves as ω_2 is scanned. This signal is similarly amplified and integrated and fed to the second recorder pen resulting in a series of peaks separated by the free spectral range (FSR) of the etalon and

providing an accurate relative frequency calibration. For absolute frequency measurements, the initial and final ω_2 frequencies of a scan are measured with a calibrated spectrometer (Cary-82 or Spex-1402). Frequency uncertainties are estimated to be 0.4 cm^{-1} or better. The remainder of this chapter deals with the various components in somewhat more detail and begins with a discussion of the Nd-YAG laser.

2.B Nd-YAG Laser

The Nd-YAG laser cavity, Figure (2.2), is equipped with four devices to reduce the linewidth ($\Delta\omega_0 \sim 1.5 \text{ cm}^{-1}$). These include a Q switch, two Fabry-Perot solid etalons coated for 18% reflectivity with free spectral ranges (FSR) of 1.1 and 0.26 cm^{-1} , and an electronic line narrowing device (Quanta-Ray model ELN-1). The thin film polarizer (POL) is set to pass radiation with electric vectors polarized at 45° to the lasing axis. The $\lambda/4$ wave plates create circularly polarized light for even extraction of energy stored in the laser rod (preventing hole burning). The Q switch (KD*P) is adjusted to allow slight leakage and a weak train of longitudinal modes builds up when the flashlamps are fired. A fast photodiode monitors the intensity of this train of pulses, and when a preset

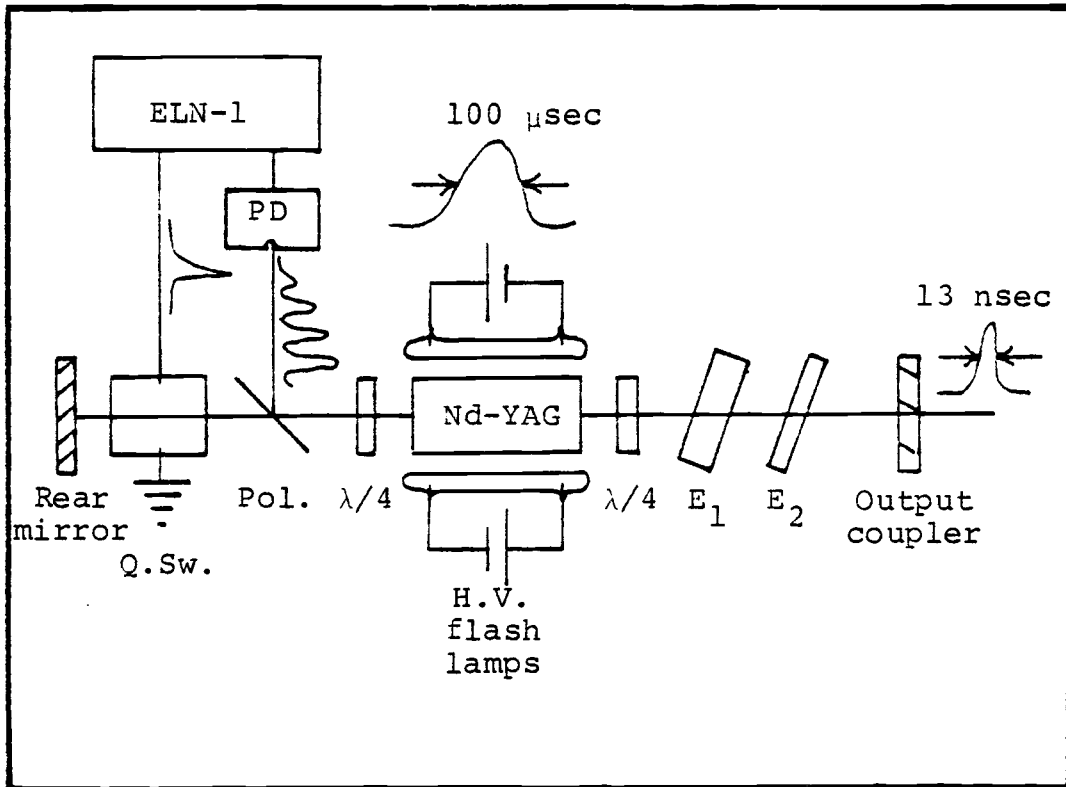


Figure 2.2. Schematic diagram of Nd-YAG laser cavity.

intensity is reached the ELN-1 fires the Q switch allowing a lasing window of ~ 13 nsec (FWHM) duration. Figure (2.3) shows two oscilloscope traces of the 1064 nm pulse taken with a TEK 7834 storage scope. The top trace clearly shows the effects of multiaxial (longitudinal) mode beating while the bottom trace shows single axial mode operation.

From the top trace, the measured time separation between adjacent axial modes, Δt_{ax} , is 5.6 nsec. The effective cavity length, L_{eff} , is related to Δt_{ax} by

$$\Delta t_{ax} = \frac{2L_{eff}}{c} = 5.6 \text{ nsec}$$

where c is the vacuum speed of light, and

$$L_{eff} = 84 \text{ cm} .$$

The measured cavity length is 70 cm but this includes high index materials such as the etalons, Q-switch and laser rod. The frequency difference between axial modes, $\Delta\omega_{ax}$, may be calculated from the effective length by

$$\Delta\omega_{ax} = \frac{1}{2L_{eff}} = 0.006 \text{ cm}^{-1} .$$

since the lasing duration is about 13 nsec (FWHM) it follows that, at the most, three axial modes may be present. This gives an approximation for the ω_0 frequency jitter, $\Delta\omega_0$, of



Figure 2.3. Oscilloscope traces of the 1064 nm Nd-YAG beam showing multimode, upper trace, and single mode, lower trace, operation. The time scale is 10 nsec/div.

$$\Delta\omega_0 \approx 3\Delta\omega_{ax} = 0.18 \text{ cm}^{-1} .$$

By careful Q-switch bias voltage adjustment and fine tuning of the intracavity etalons, it is possible to achieve single mode operation about 60% of the time. Since the two events pictured in Figure (2.3) are not distinguished during an experiment, the narrowest frequency width available is determined solely by this frequency jitter. The result is that the width of the second harmonic at ω_1 , $\Delta\omega_1$, is

$$\Delta\omega_1 \approx 2\Delta\omega_0 = 0.035 \text{ cm}^{-1} .$$

This may be compared to the measured width of ω_1 , obtained by examining the interference fringes of a 0.2 cm^{-1} FSR Fabry-Perot analyzing etalon, of about 0.03 cm^{-1} .

Quite frequently, during a long experiment, the ω_1 frequency begins to hop between thick etalon modes ($\Delta\omega_1 \approx 0.26 \text{ cm}^{-1}$). Keeping the room temperature between 65-67°F greatly improves this situation and the cause is most likely local heating in the thick etalon, even though the etalons are mounted in heated and well regulated cells. If ω_1 happens to be involved in an electronic resonance, this mode hopping can cause dramatic spectral changes (Chapter 3).

2.C YAG Harmonic Generation

For all experiments discussed in this work, the second harmonic of the YAG laser was used as the primary ω_1 beam. The photofragmentation work on benzene also required the generation of either the third or fourth harmonic (at 355 or 266 nm respectively) as the photolysis source. The third harmonic also served to pump a dye laser and investigate the tuning ranges of a number of laser dyes [25]. These three harmonics were achieved using KD*P crystals oriented in the appropriate phase matching geometries [13, 15, 26]. All crystals were mounted in sturdy mirror mounts fitted with micrometer adjustment screws allowing fine tuning of the phase matching angle. Even though these crystals are hygroscopic, it was found that they need not be housed in a sealed cell fitted with windows and filled with an index matching fluid [27]. Water vapor fogging and other deterioration of the crystal faces is easily rectified by polishing on a soft pitch plate (Apiezon W) using cerium oxide abrasive powder and dry ethylene glycol as lubricant [27]. The excess ethylene glycol may be removed by wiping with a xylene soaked "Kleenex"* tissue.

All experiments not involving the third harmonic (355 nm) used the crystal orientation shown in Figure (2.4) for

*"Kleenex" brand facial tissue was found to be least abrasive to the crystal.

generation of ω_1 . This crystal is a 10 x 10 x 30 KD*P (87% deuterium) cut for type II phase matching ($\theta = 55^\circ$) and a conversion efficiency of about 30% is obtained. The remaining 1064 nm radiation is passed through a similar crystal (KD*P type II, 10 x 15 x 30 mm, $\theta = 53^\circ$) to extract more green to pump a dye laser. The efficiency of this doubling process is much reduced since the 1065 nm radiation after the first doubler is elliptically polarized. Because the doubling process is nonlinear and depends on the square of the incident intensity, the ω_1 pulse is narrowed in time to about 10 ns (FWHM).

Third harmonic generation, to produce 355 nm radiation, is achieved by placing a second KD*P type II crystal (10 x 15 x 30 mm) summing 1064 and 532 nm, immediately after the first doubling crystal. The orientations of these crystals are shown in Figure (2.5) along with the polarization of the beams. Approximately 35 mJ of 355 nm radiation may be obtained for photolysis and dye laser pumping. For photolysis applications, a 1.1X quartz telescope placed in the 355 nm beam provided adjustment of the common focus at the sample.

The fourth YAG harmonic at 266 nm is produced by doubling the frequency of the main 532 nm beam with a KD*P type I crystal (10 x 15 x 30 mm, $\theta = 90^\circ$) housed in a heated and well regulated cell. Approximate phase matching is achieved by maintaining the crystal at about 39°C. Temperature

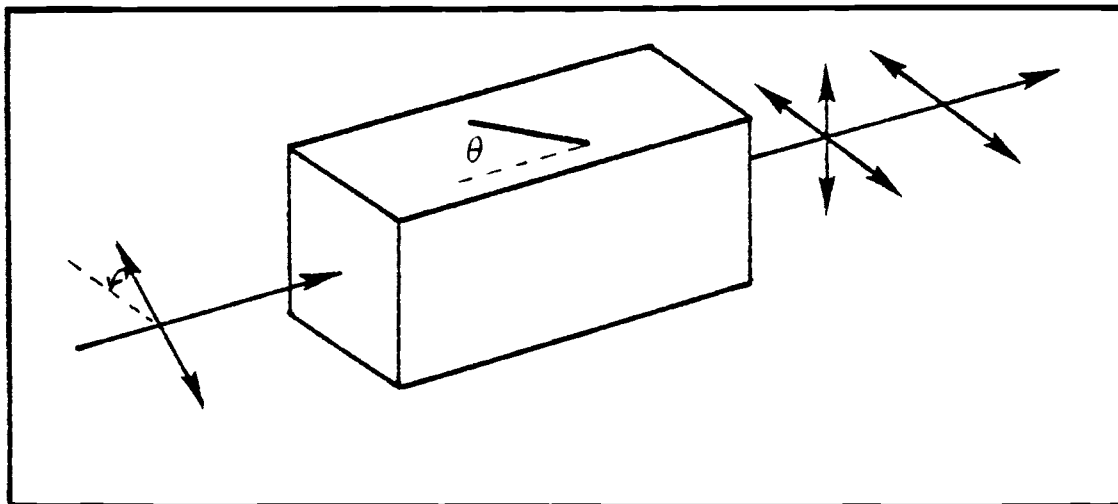


Figure 2.4. Orientation of KD*P type II crystal for second harmonic generation, SHG, at 532 nm.

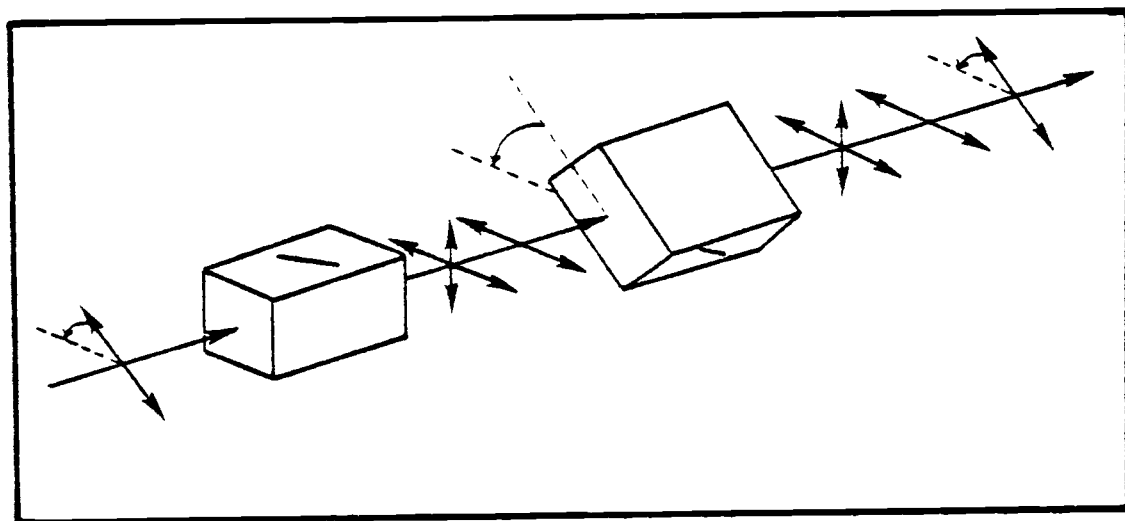


Figure 2.5. Orientation of KD*P type II crystal for third harmonic generation, THG, at 355 nm.

regulation was found to be insufficient for phase matching due to local heating in the crystal. As a consequence, fine angle tuning during an experiment was necessary to maintain constant UV intensities. The crystal housing was made of aluminum and wrapped with a small heater element. This was then enclosed in a delrin cylinder, for insulation, and attached to a large mirror mount. A thermistor, embedded in the aluminum, sensed the temperature which was controlled by a Yellow Springs Model 72 temperature controller. With this system, 10-20 mJ of 266 nm radiation could be maintained during an experiment. The UV intensity was monitored on an oscilloscope using a photo-voltaic diode as the detector. A 1.1X telescope placed in the ω_1 beam allowed the foci of the green and 266 nm beams to be matched in the sample.

Commercial optical grade quartz was found to be unsuitable for elements which handled the 266 nm beam. The blue fluorescence produced in this material interfered with detection of the blue CARS signal. UV grade quartz optics were necessary to eliminate this problem. Also, a non-fluorescing UV filter (Corning 3-144) was used immediately before the sample collimating lens to attenuate the photolysis beam and prevent another source of blue fluorescence.

2.D Dye Laser

The source of ω_2 radiation was provided by a ND-YAG pumped dye laser employing flowing dye cells. Small electric pumps (Micropump model 12A-40-303) connected to a variac allowed control of the flow rates. Many dye laser designs were investigated in order to minimize the ω_2 linewidth, $\Delta\omega_2$. It was found that no one dye laser design proved entirely satisfactory for all applications. Important performance factors such as tuning ranges, polarization, beam quality, output stability and ease of operation were considered along with minimal linewidth in evaluating each design. The dye laser components were mounted on a small optical table (1 ft x 5 ft) drilled with 1 in bolt pattern to allow for maximum flexibility. The remaining parts of this section describe the basic designs employed along with discussions of their associated advantages and disadvantages.

Two optical pumping schemes, transverse and semi-longitudinal, were used to excite the dye and are diagrammed in Figures (2.6) and (2.7). Transverse pumping is achieved by focusing the pump beam with a cylindrical lens ($f = 400$ mm) to a horizontal line image slightly behind (~ 2 mm) the front face of a wedged flowing dye cell. The wedged shape insures that broadband lasing will not occur due to reflections in the cell picking up gain. A telescope, before the

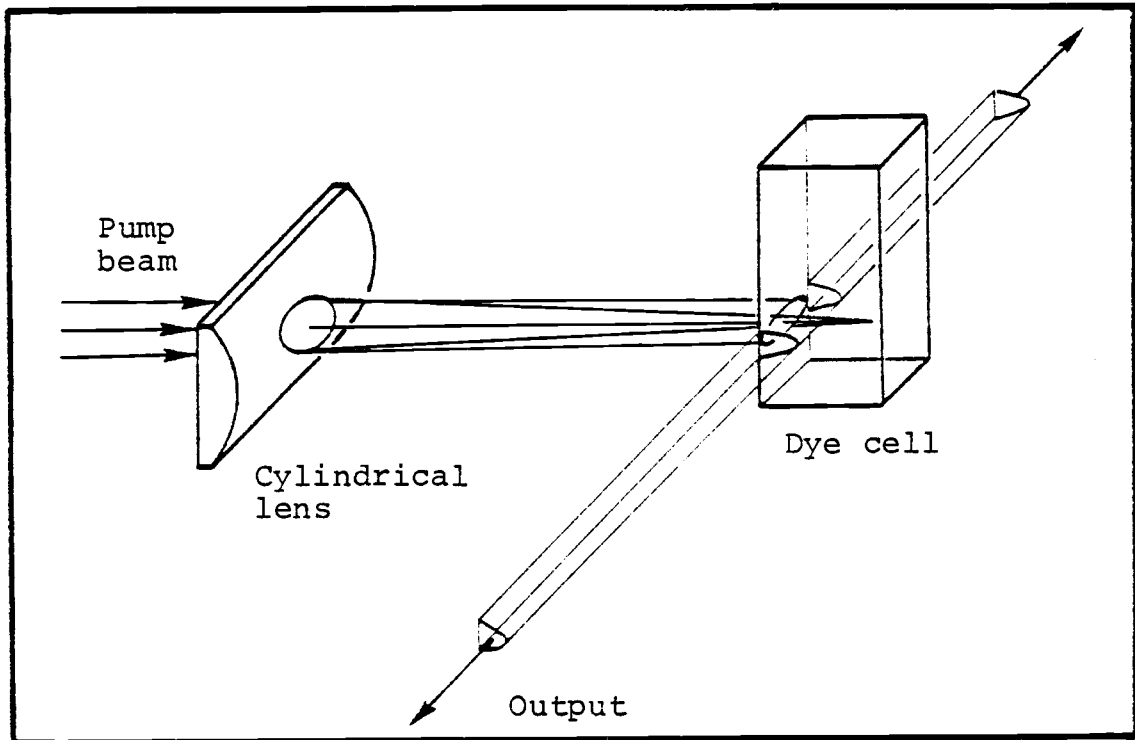


Figure 2.6. Transverse optical pumping.

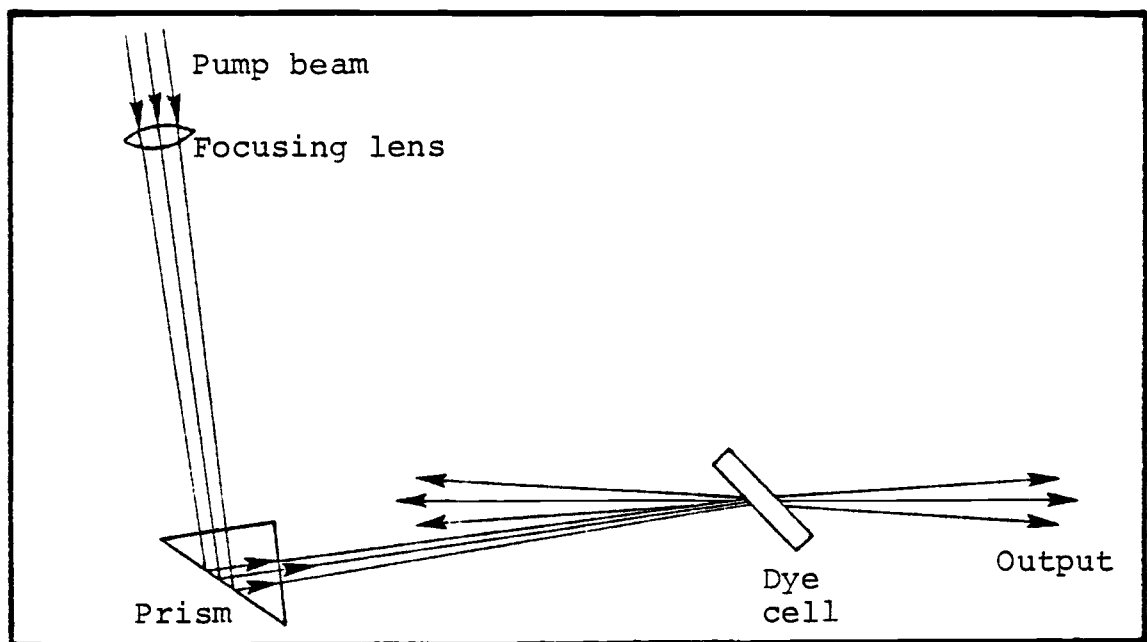


Figure 2.7. Semilongitudinal optical pumping.

cylindrical lens, matches the pump beam diameter to the dye cell width. Pump beam powers greater than about 6 mJ were found to burn the quartz dye cell. The dye concentration is adjusted so as to absorb all of the pump beam energy within the first 1-2 mm of the cell. The beam emerges from this pumping scheme with a slightly wedged shape, Figure (2.6), which did not overlap very efficiently, in the sample region, with the focused doughnut from ω_1 . This problem can be alleviated by semilongitudinal pumping of the dye laser amplifiers. Transverse pumping worked well to pump all dyes tested with both 532 and 355 nm sources.

Semilongitudinal optical pumping, Figure (2.7), involves bringing the pump beam into the dye cell at a small angle to the lasing axis. A spherical converging lens ($f = 280 \text{ mm}$) focuses the pump beam and a small 90° prism deflects the beam towards the cell. The flowing dye cell was constructed from delrin and fitted with quartz windows separated by about 2 mm of dye solution [27]. Orienting the cell near Brewster's angle to the lasing axis prevents internal reflections from forming a broadband cavity and also favors the transmission of the desired horizontally polarized dye laser output. When used in the laser oscillator, the lens is positioned to give about a 1.5 mm diameter pump beam at the dye cell (with the focus behind the cell). Dye concentrations are adjusted to allow the slightest amount of pump energy to exit the cell. This

pumping scheme did not work for 355 nm pumping of coumarin dyes but it was very satisfactory for all 532 nm pumping.

Two basic cavity designs were employed to generate the tunable ω_2 source. A high resolution stepper motor (Aero-tech model ATS-302-MMS-50 motor and model ASM-200-1 driver) served to scan the dye laser. Both designs relied upon diffraction gratings to achieve wavelength selection. Dye laser conversion efficiencies ranged from 1-10% depending upon type of dye and solvent, linewidth, polarization and wavelength (to name a few). Most of the experimental work was performed using a Hänsch type laser oscillator [28] with a diffraction grating as the back mirror. A second design utilizing a diffraction grating at grazing incidence as a beam expander [29-32] offers narrower linewidths but does not have the red tuning range of the first system.

Figure (2.8) shows the basic components of the Hänsch dye laser cavity. The output coupler is coated for partial reflectivity in the visible and varies from $\sim 5\%$ at 400 nm to $\sim 30\%$ at 700 nm. A 20X telescope beam expander magnifies the small ($\sim 1-2$ mm diameter) stimulated emission beam from the dye cell to fill the diffraction grating. A 316 μ/mm echelle grating, blazed at 63.5° , fitted with a cosecant arm, and mounted in a modified Lansing gimbal mirror mount in Littrow configuration, is the tuning element. This

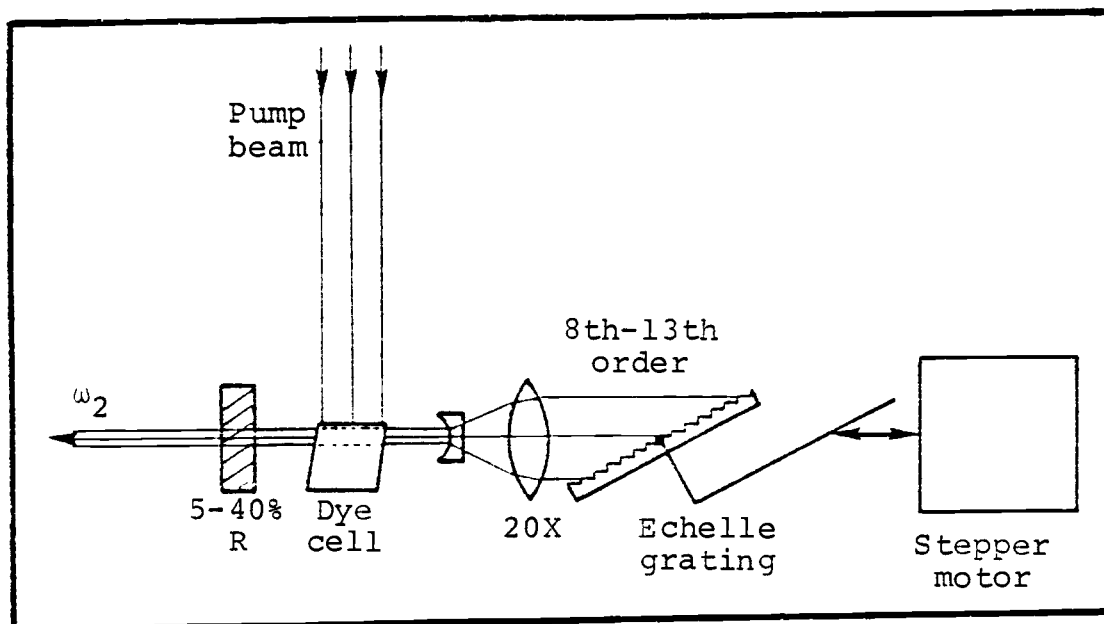


Figure 2.8. Schematic drawing of the Hänsch dye laser cavity used in this work.

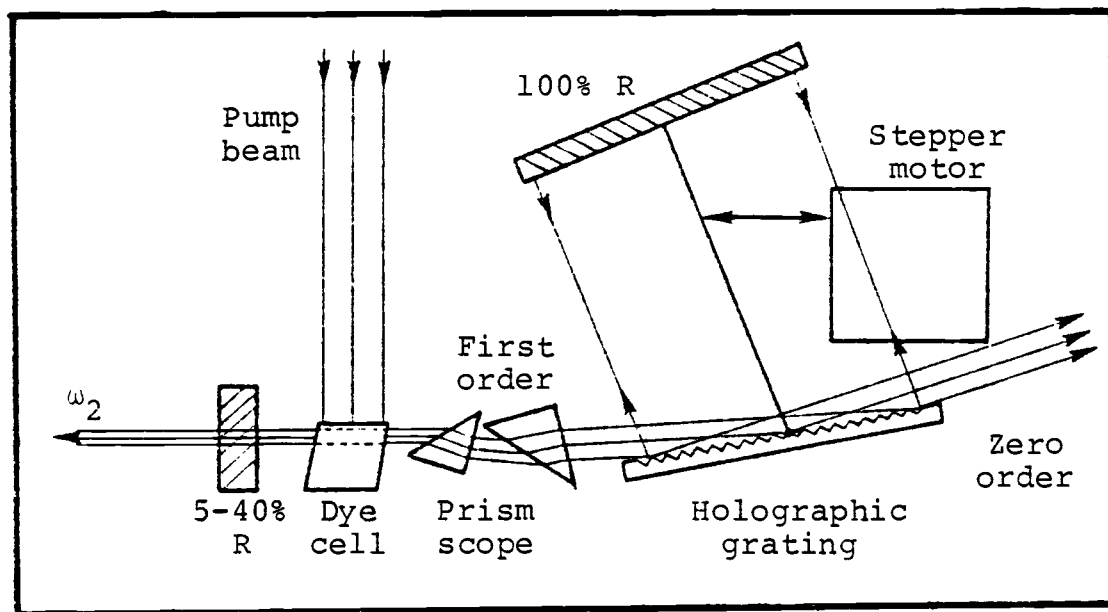


Figure 2.9. Schematic diagram of the grazing incidence dye laser used in this work.

geometry provides wavenumber tuning from displacements of the stepper motor. The two telescope lenses are housed in individual x-y translation stages for precise optical adjustment. The performance of this cavity depends on the proper alignment of the telescope and grating. Initial set up is made with the telescope removed and the grating tilt is adjusted to return the zero order reflection back to the He-Ne alignment laser. Next, the grating rotation is varied so that all negative and positive orders are similarly reflected. Final alignment involves installing the telescope and repeating the above procedures. This complicated and tedious alignment is one of the more frequent criticisms of the Hänsch cavity [28-33]. At times, a four prism (right angle) expander, similar to reference [34], with $\sim 30X$ magnification was substituted for the telescope. Since magnification only occurs in one direction, the grating rotational alignment was not as critical. This arrangement also provided improved transmission of the desired output polarization. When transverse pumping, the dye cell is attached to a translation stage allowing for alignment of the lasing axis. The overall cavity length was about 33 cm.

The echelle grating is operated in eighth to thirteenth order, near its blaze angle, and typical linewidths are $0.2-0.3 \text{ cm}^{-1}$. Room was provided between the dye cell and telescope for insertion of a calcite Glan-Thompson polarizer.

This cavity design proved successful for generating radiation from 400-750 nm, and a typical set of laser dye tuning curves is included in Appendix D. One minor inconvenience of this system was the occasional simultaneous output of two lasing wavelengths. This resulted from overlap of two grating orders diffracting two wavelengths which also happened to fall within the laser dye tuning range. Changing the laser dye rectified this annoyance. For broadband operation, a plane front surface mirror is placed in front of the diffraction grating.

The dye laser linewidth can be narrowed to about 0.15 cm^{-1} with the cavity design shown in Figure (2.9). A two prism (right angle) beam expander provides one dimensional magnification of about 7X [34]. The diffraction grating (1800 $\text{\AA}/\text{mm}$ holographic grating) is operated near grazing incidence, $\sim 88^\circ$ [29-32], and the first order diffraction is intercepted by a plane mirror. The grazing angle is adjusted to fill the grating with light. The rear mirror is mounted to an arm which rotates from a point in the center of (and in) the grating plane. Stepper motor displacements result in wavelength tuning [29]. The zero order output is used to monitor the dye laser performance with an analyzing etalon. This design enjoys many advantages over the Hänsch cavity such as narrower linewidth, simpler setup and operation, more stable frequency and intensity output and better polarization discrimination. The tuning range

is limited, however, since the longer red ($\lambda < 730$ nm) wavelengths are diffracted back into the grating grooves.

The dye laser output polarization was adjusted before amplification with a double rhomb prism polarization rotator. The two internal reflections in the input prism results in circularly polarized light [35] and the second prism reverses this process to again produce linearly polarized light. A rotation of the prism assembly through an angle, θ , rotates the output polarization through 2θ . Two advantages of this device over $\lambda/2$ polarization rotators are that it will work for all wavelengths, and it is rather inexpensive to construct.

One or two dye laser amplifiers, pumped semilongitudinally, are used to increase the dye laser output to typically 0.3-2 mJ in a 7-8 nsec (FWHM) pulse. The amplifier pump beam diameters are matched to the dye laser diameter by movement of the pump beam focusing lenses. Saturation of the dye, in the amplifier cells, smooths out oscillator intensity fluctuations and typical shot to shot intensity fluctuations less than 20% are obtained even through ω_1 intensity fluctuations of 30% are common.

The amplified dye laser output is passed through a 3X telescope to match the diameter of the ω_1 beam. This telescope is also necessary to achieve a common focus of the two beams in the sample. Initial alignment of the common focus in the sample involves passing the beams through a

pinhole ($\sim 70 \mu\text{m}$ diameter) drilled by the focused dye laser beam.

2.E Broadband CARS

In some experiments, the ω_3 spectrum was recorded in one laser pulse with an optical multichannel analyzer (Princeton Applied Research model OMA-2). For this experiment, the broadband dye laser output was focused into the sample cell as previously described. For low resolution studies, the ω_3 spectrum is dispersed with a 1200 \AA/mm grating, operating in first order, and then focused in the detector surface plane. This arrangement allows about a 400 cm^{-1} spectrum (typical broadband ω_2 output) to be recorded.

For higher resolution broadband studies, the OMA-2 was mated to the output of a Spex-1402 spectrometer fitted with 1800 \AA/mm diffraction gratings and equipped with a remote digital wavelength readout (Spex model 1734). The ω_3 beam is focused at the entrance slit with the appropriate lens to match the F number of the monochromator to ensure maximum resolution and light throughput. The proper focal length, $f\ell$, lens for a collimated CARS beam of diameter, d , is given by

$$f\ell = dF$$

where F is the F number of the spectrometer. The output port of the Spex contains a swing out mirror for using two detectors as shown in Figure (2.10). With the mirror positioned for OMA detection, the focus of the spectrometer is at the detector image plane. The spectrometer image plane is slightly curved and dispersion as a function of detector channel number was measured by carefully scanning several Hg and Ne emission lines and Ar^+ laser lines across the detector using the digital wavelength readout. Final wavelength calibration was performed during an experiment by determining the channel position of a convenient emission line. This, coupled with the appropriate dispersion curve, enabled the OMA-2 wavelength calibration software to present the spectrum as a function of wavelength. The final spectral displays were presented as a function of vacuum wavenumbers on an x-y recorder (Houston model 2000). The resolution of this system is limited by the detector channel separation ($\sim 25 \mu\text{m}$). In the blue region this corresponds to about $0.32 \text{ cm}^{-1}/\text{channel}$ ($\sim 0.07 \text{ \AA}/\text{channel}$). The spectral range covered by the detector is thus about 160 cm^{-1} .

Although the OMA is capable of obtaining a single laser pulse spectrum, it is also well suited for multiple pulse data acquisition and background subtraction. By gating the image intensifier (PAR model #1211) at the laser repetition rate, weak signal integration for a few minutes is possible.

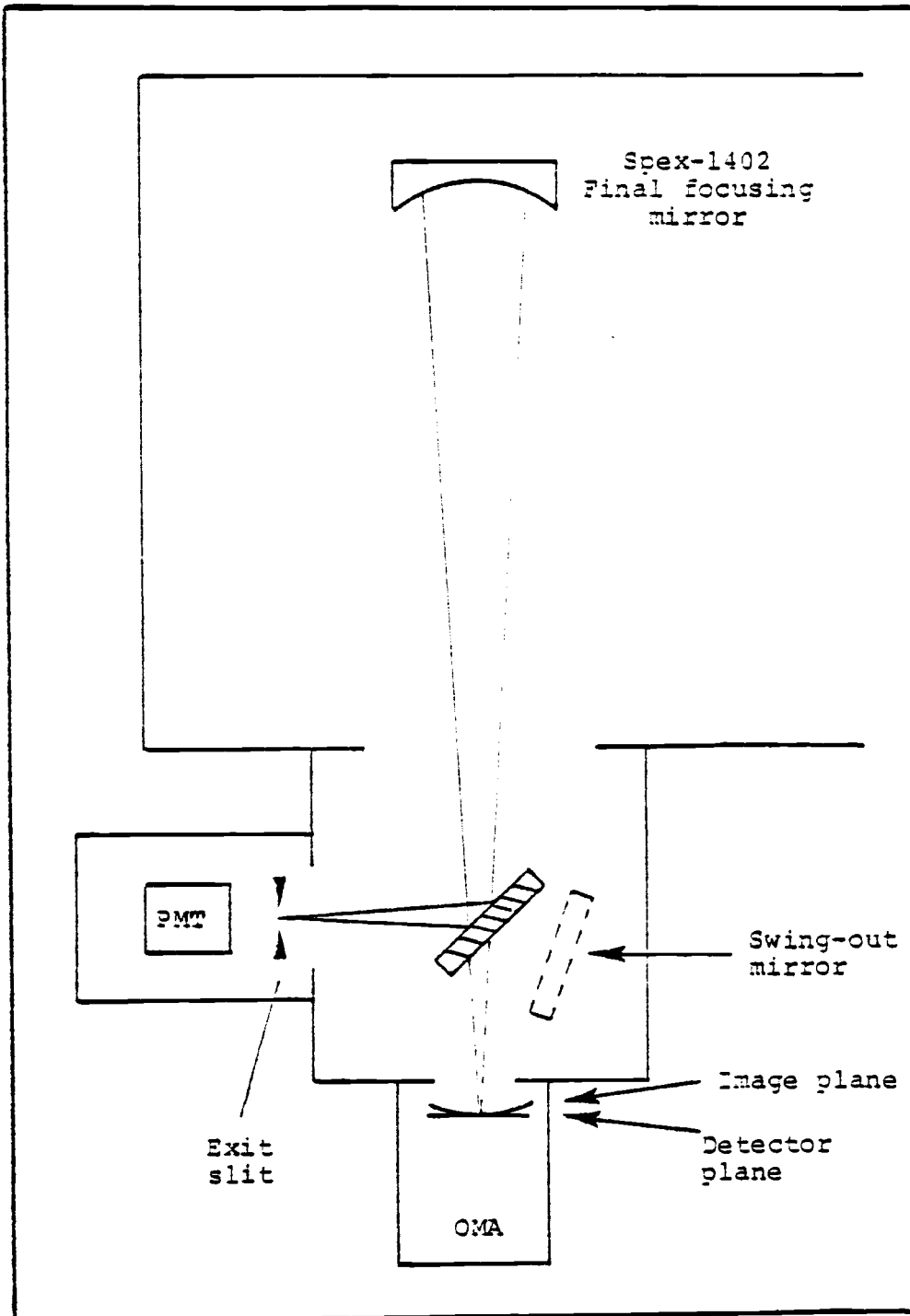


Figure 2.10. Diagram showing the orientation of the two detectors mounted to the Spex-1402 spectrometer. The swing-out mirror permits use of either the PMT or OMA. Curved image plane results in nonlinear dispersion at detector plane.

The signal averaging capabilities are further improved, however, by cooling the detector to greatly minimize the dark count of the vidicon. Consequently, a dry ice cooler was constructed to house the OMA-2 detector. The detector is contained in a sealed aluminum can which is in contact with the dry ice. The can is fitted with cable feedthroughs and a dry N₂ purge system. The can is surrounded by a double plexiglass wall box. The space between the walls is filled with urethane foam insulation. The entire box assembly is mounted on rails and fitted with fine translation and rotation adjustment screws. Within about 30 minutes of cooling, the dark count was negligible.

CHAPTER 3
RESONANT CARS SPECTRA OF NO₂*

3.A Introduction

In Chapter 1 the effects of possible resonant enhancement of a CARS signal was discussed in terms of one and two photon absorption schemes (Figure 1.1). Several examples of resonant CARS spectra of liquids have appeared [38-41] and Taran et al. [42, 43] observed the first resonant CARS in gases. In Taran's work, they report the resonant signal of 0.1% I₂ in air to be approximately twice as intense as the Q branch of the 20% O₂ constituent and expect resonance enhancements of about 100 for I₂ and other colored gases. Although NO₂ has extensive visible absorptions they were unable to obtain a 2ν₂ CARS signal using either dye or ruby laser sources for ω₁ [43]. Using a doubled YAG laser source for ω₁ (at 532 nm), however, a very rich and strong CARS spectrum of NO₂ results. On close inspection, the spectral features are found to be very sensitive to the ω₁ frequency and apparently derive from several resonant processes briefly described in Chapter 1. Some of the general features of the resonant CARS spectra of NO₂ are discussed in the following sections of this chapter.

*This chapter is abstracted from the published results appearing in reference [37].

3.B Experimental

The basic experimental arrangement is discussed in Chapter 2. The NO_2 was taken directly from a lecture bottle (Matheson) and introduced into a 15 cm cell fitted with O-ring sealed quartz windows. Initial pressures of 1-20 torr were used and measured with a 100 torr Validyne pressure head. As noted by others [44], a slow decrease in signal was observed after irradiation over a period of an hour. As a consequence, the cell was evacuated and refilled periodically or a slow flow through the cell was maintained.

Absorption measurements were made in ω_1 and ω_3 regions by passing the emission of a tungsten light source through a 10 cm cell filled with 40 torr NO_2 . The transmitted signal was recorded with a Cary 82 spectrometer at 0.5 cm^{-1} resolution. High resolution absorption traces in the ω_2 region were available from reference [45].

The ω_1 frequency was varied by slightly changing the tilt of the thick etalon inside the ND-YAG laser cavity. The frequency change was monitored by noting the ω_1 interference fringes produced by a 0.4 cm^{-1} free spectral range Burleigh etalon with a finesse of 30.

3.C Results and Discussion

Figure (3.1) displays the general features of the CARS spectrum of 20 torr NO_2 . This spectrum was recorded using

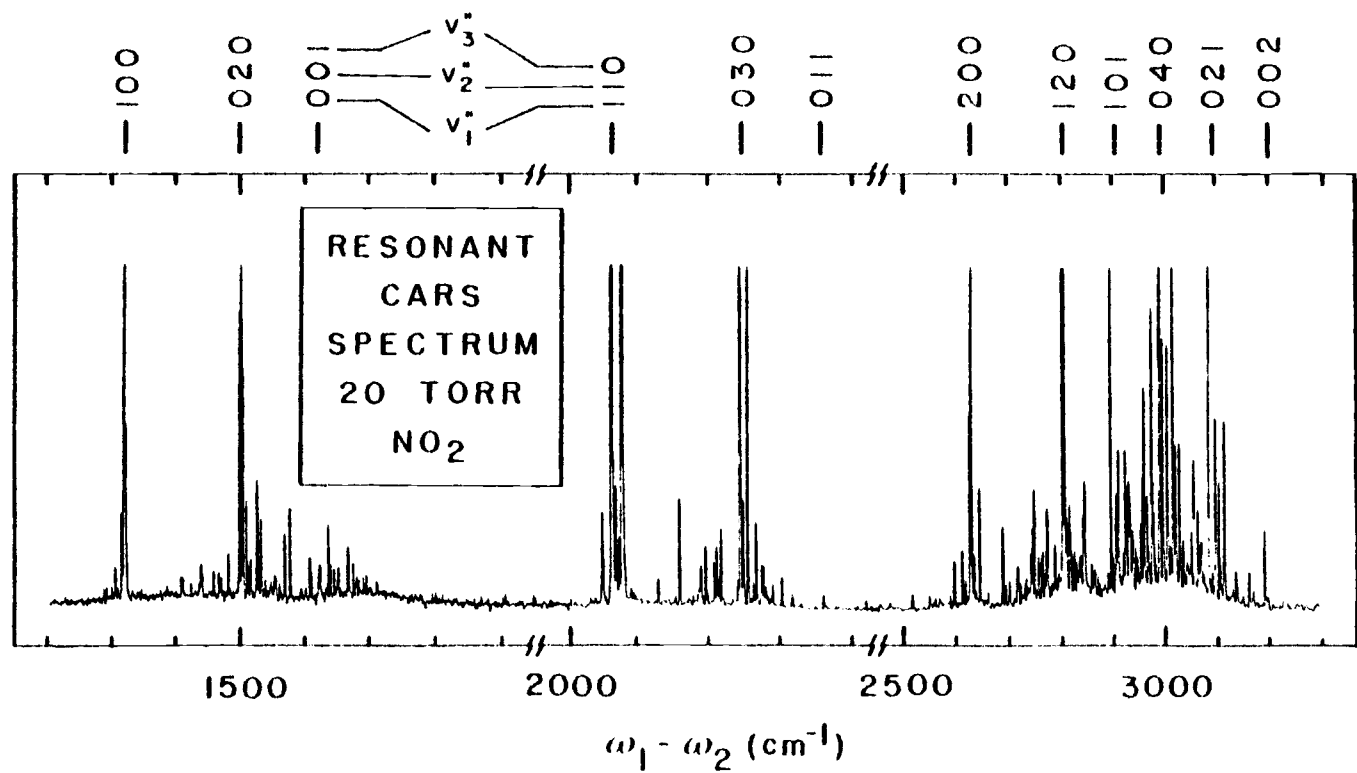


Figure 3.1. Resonant CARS spectrum of 20 torr NO₂.

three dye mixtures and no intensity corrections have been made for dye intensities or filter factors. Since these are slowly varying corrections, the relative intensities within each dye range should not change by more than a factor of two. All spectral features disappeared if either ω_1 or ω_2 beams are blocked.

Further confirmation that these anti-Stokes features derive from a CARS process came from analysis of the ω_3 signal with a 0.45 m McKee-Pederson spectrometer at $\sim 5 \text{ cm}^{-1}$ resolution. When the difference, $\omega_1 - \omega_2$, was tuned to any of the strong features of Figure (3.1), only emission at $\omega_3 = 2\omega_1 - \omega_2$ was detected. This excludes the possibility that part of the spectrum could arise from excited state fluorescence resulting from simultaneous or sequential ω_1 , ω_2 absorption.

The frequencies of all fundamental and combination transitions of NO_2 were calculated from the ground electronic state constants of Lafferty and Sams [46]. These pure vibrational transitions are indicated in Figure (3.1) and the close correspondence to the observed spectrum suggests that most, if not all, features arise from such transitions in the ground electronic state, 2A_1 (point group C_{2v}). The spectrum is dominated by totally symmetric transitions (A_1 type) and the high intensity of overtone and combination bands is characteristic of normal resonance Raman or fluorescence spectra. Polarization measurements

were made below 2000 cm^{-1} and, as expected, ω_3 had the same polarization as ω_2 . The ω_3 intensity dropped by a factor $\sim 1/2$ when the polarization of ω_2 was made orthogonal to ω_1 . This is near the value of $(3/4)^2$ predicted for a depolarized CARS transition [8]. Under comparable conditions, the intensity ratio for the polarized Q branch of O_2 was zero. Thus, ν_1 and $2\nu_2$ transitions of ground state NO_2 are, at the most, only slightly polarized.

The CARS spectrum of NO_2 is very similar to the 532 nm Stokes fluorescence spectrum recently reported by Donnelly and Kaufman [47] but it possesses two important advantages. First, much improved resolution (0.3 cm^{-1} versus $20\text{-}30 \text{ cm}^{-1}$) is obtained since the CARS linewidth is only dependent on the laser linewidths (Chapter 1). Also, Taran has shown that Doppler width limitations do not apply in the case of resonant CARS [42]. The second advantage is the absence of pseudo-continuous fluorescence emitted from states other than those pumped by the excitation source. Most of this emission is produced by collisional quenching during the fluorescent lifetime of NO_2 (~ 1 to $100 \text{ }\mu\text{sec}$ depending on the state) [45] and, in the work of Donnelly and Kaufman, this fluorescence dominates the spectrum at NO_2 pressures above 10 mtorr (collision time $\sim 9 \text{ }\mu\text{sec}$). Since the CARS process is "instantaneous" (inelastic scattering), these complications do not occur and discrete spectra are obtained from 1 to 100 torr.

The ω_3 intensity did not scale with the square of NO_2 pressure, as expected for CARS, but was actually five times weaker at 100 torr NO_2 than at 20 torr. This is most likely due to absorption at one or more of the ω_1 , ω_2 , or ω_3 frequencies along with collisional broadening. Further evidence of collisional broadening comes from a factor of five decrease in ω_3 intensity when 50 torr N_2 was added to 2 torr NO_2 . As was mentioned in Chapter 1, collisional broadening is known to reduce ordinary CARS signal strengths because of the inverse dependence on the square of the Raman transition linewidth [3, 45].

The possibility that some of the spectral features arise from the colorless dimer, N_2O_4 , is slim since, under experimental conditions (room temperature, 20 torr pressure), N_2O_4 is more than 96% dissociated. Lacking chances of resonance enhancement, and being a dilute solute, the likelihood of observing CARS signals from N_2O_4 is expected to be negligible.

Figure (3.2) shows the effect of ω_1 variation on spectra in the $2\nu_2$ region near 1500 cm^{-1} . Dramatic changes occur as ω_1 (linewidth $\sim 0.04 \text{ cm}^{-1}$) is decreased a total of about 0.2 cm^{-1} from Figures (3.2a) to (3.2c). The precise frequency of ω_1 is unknown but it is about 18789.5 cm^{-1} . Such changes with ω_1 are more characteristic of resonance fluorescence than of resonance Raman scattering and similar variations have been observed by Abe in

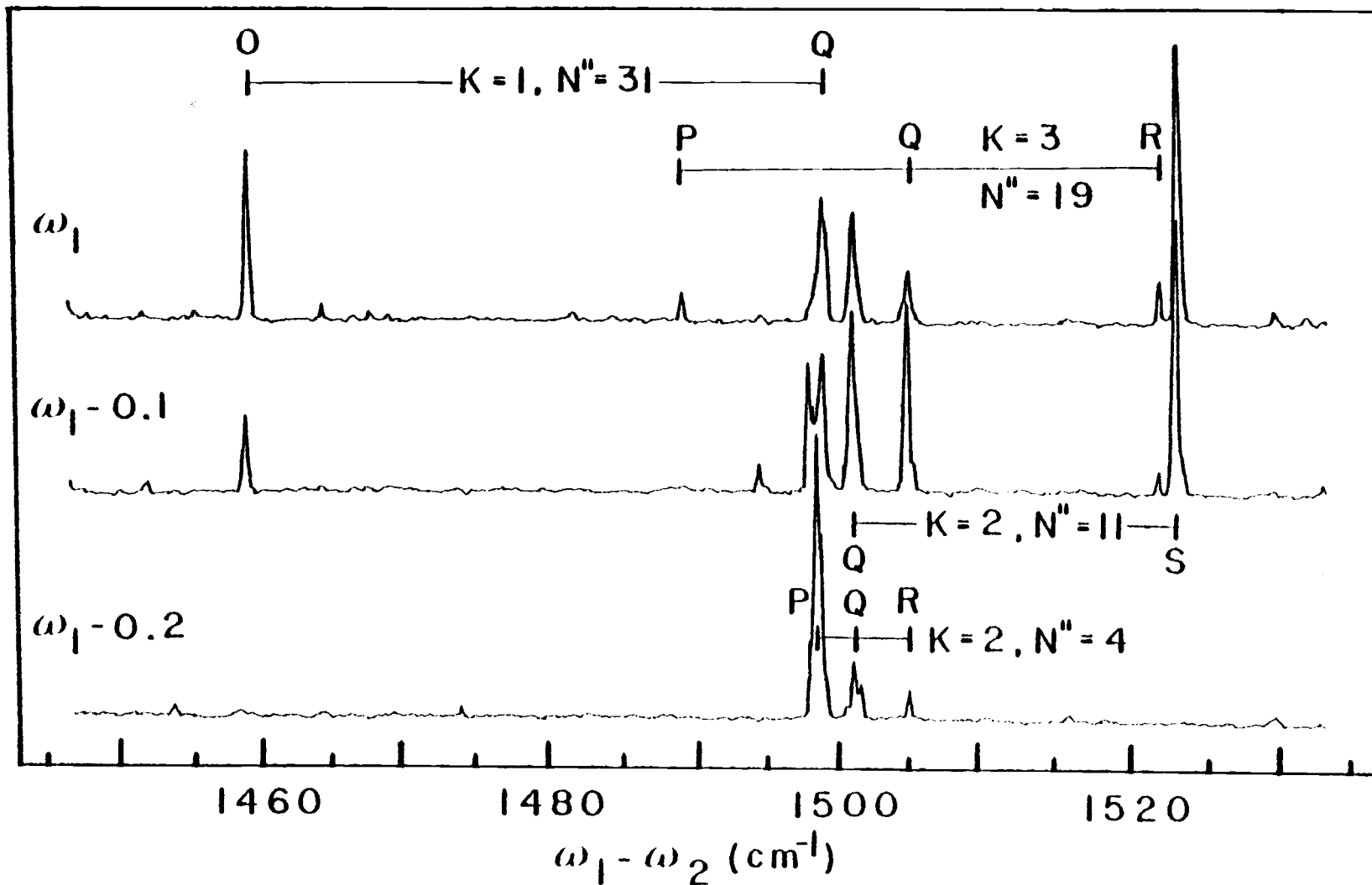


Figure 3.2. Effect of slight ω_1 frequency variations on the $2\nu_2$ spectrum of NO_2 . $\omega_1 \approx 18789.5 \text{ cm}^{-1}$. ω_1 decreases 0.2 cm^{-1} in going from (a) to (c).

the usual Stokes region [49]. In fact, "true" resonance Raman spectra have been obtained from NO_2 only in cases where resonant fluorescence is inhibited by addition of high pressures of a quenching gas (e.g., 10 atm of SF_6) [50] or in solid matrices.

Many of the general features of the CARS spectrum can be understood in terms of the energy levels shown in Figure (3.3). NO_2 is very close to a prolate symmetric top ($A > B \cong C$, $B - C = 0.023 \text{ cm}^{-1}$) and the ground electronic state energy levels are accurately calculated by conventional functions of N and K quantum numbers [42, 43, 46, 47]. K is the vibronic angular momentum quantum number and is the resultant of vibrational angular momentum and electronic angular momentum about the internuclear axes. N is the total rotational angular momentum quantum number excluding electron spin ($N = J - S$). If ω_1 plays a role in an electronic resonance from a level (N'' , K'') in the ground state (2A_1), the excitation selection rules can be summarized by [51]:

For $X^2A_1 \rightarrow {}^2B_2$ excitation

$$\Delta K = 0, \Delta N = 0, \pm 1 \text{ if } K \neq 0$$

$$\Delta K = 0, \Delta N = \pm 1 \text{ if } K = 0$$

For $X^2A_1 \rightarrow {}^2B_1$ excitation

$$\Delta K = \pm 1, N = 0, \pm 1 .$$

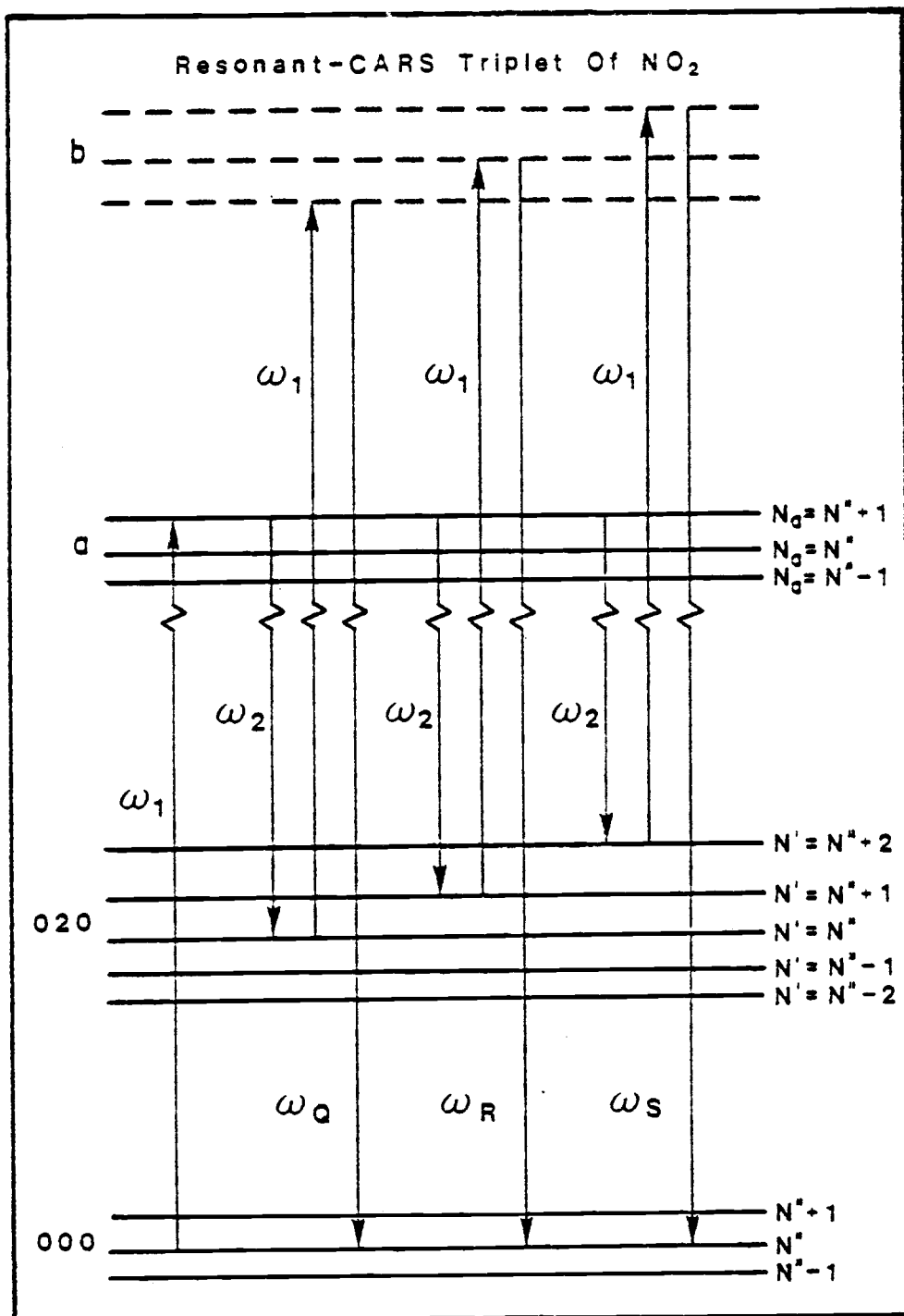


Figure 3.3. Energy level diagram for a possible "resonant" CARS triplet of NO_2 . ΔK is assumed to be zero. Drawing is not to scale, (a) and (b) represent higher electronic levels.

Both 2B_1 and 2B_2 states (and an 2A_2 state) are thought to overlap through most of the visible region but $\Delta K \neq 0$ transitions are rare and have only been reported at lower 514.5 and 488.0 nm excitation wavelengths [50, 52]. Further evidence of the unimportance of the $X^2A_1 - {}^2B_1$ transitions is provided by a fluorescence excitation study by Smalley et al. [53], of NO_2 cooled by expansion through a nozzle to 3K (rotational temperature). The resulting simplified spectrum contained no features that could be assigned to ${}^2A_1 - {}^2B_1$ fluorescence. Assuming $\Delta K = 0$, only one of the upper 2B_2 levels $N_a = N'', N'' + 1, N'' - 1$ will be excited for a given ω_1 frequency. If level $N_a = N'' + 1$ is accessed, tuning of ω_2 will stimulate a return via $N'' + 2, N'' + 1, \text{ or } N''$ in a ground state vibrational level such as (020). These three lines will coincide with S, R, and Q branch transitions in a normal Raman spectrum but would have different relative intensities. If the upper state is N'' , the triplet R, Q, P is predicted, while for $N'' - 1$ the triplet is O, P, Q. In all three cases, the spacing between the outermost members of the triplet is $2\bar{B}(2N_a + 1)$, where $\bar{B} = 1/2(B'' + C'')$.

For resonant fluorescence, the observed relative intensities of the triplets agree with those calculated from Honl-London line strengths $A_{N_a K_a N' K'}$ [51, 52]. The relative intensities in the CARS case would differ from those of resonant fluorescence because one must "return" from the

intermediate $(020)'$ level to the original $(000)''$ state. The relative probabilities for this step can be obtained from the Raman line strengths $b_{N''K''N'K'}$ [54, 55], so that the overall intensities of the CARS bands should scale as the product $A_{N_aK_aN'K'} \times b_{N''K''N'K'}$. This result predicts zero intensity for the central member of the CARS triplet if $K'' = 0$ and low intensity if N'' is large compared to K'' . The two outer members should be comparable in intensity.

From such intensity considerations and from the position and spacing of various pairs of the stronger lines in the spectra, possible N'' , K'' assignments can be calculated. For example, Table (3.1) displays the frequencies measured for the spectra of Figure (3.2) and also gives an assignment which gives very good agreement between observed and calculated frequencies. Unfortunately, this close frequency fit is not sufficient to establish these assignments since several other possible resonance conditions could exist which would complicate the spectra. Some of these possibilities are displayed in Figure (3.4) where, for simplicity, the rotational levels are not shown. In each case, at least two pairs of real levels are resonantly coupled by ω_1 , ω_2 , or ω_3 . In contrast to case a (same as Figure (3.3)), b would not yield simple triplets since simultaneous ω_1 and ω_3 resonances are not easily achieved by simply tuning ω_2 . However, with the high density of NO_2 states in

Table 3.1. CARS transitions (cm^{-1}) observed in $2\nu_2$ region for NO_2 .

| a* | | b | | c | | K'' | N'' | N' | |
|--------------------|----------|--------------------|----------|--------------------|----------|-----|-----|----|----|
| ν_{obs} | Δ | ν_{obs} | Δ | ν_{obs} | Δ | | | | |
| 1447.3 w | 0.5 | | | | | O | 1 | 31 | 29 |
| 1498.7 m | 0.5 | | | | | Q | 1 | 31 | 31 |
| 1459.0 s | -0.4 | 1458.7 m | (-0.7) | | | O | 2 | 25 | 23 |
| 1501.0 m | 0.4 | 1500.7 s | (0.1) | | | Q | 2 | 25 | 25 |
| 1488.9 w | -0.1 | | | | | P | 3 | 19 | 18 |
| 1505.0 m | 0 | | | | | Q | 3 | 19 | 19 |
| 1521.7 w | -0.1 | | | | | R | 3 | 19 | 20 |
| | | 1494.1 w | -0.3 | | | O | 3 | 7 | 5 |
| | | 1504.7 s | 0.6 | | | Q | 3 | 7 | 7 |
| | | 1498.7 m | -0.3 | | | Q | 1 | 12 | 12 |
| | | 1521.5 w | -0.3 | | | S | 1 | 12 | 14 |
| | | | | 1498.4 vs | 0.5 | P | 2 | 4 | 3 |
| | | | | 1501.0 m | -0.2 | Q | 2 | 4 | 4 |
| | | | | 1505.0 w | -0.5 | R | 2 | 4 | 5 |
| | | | | 1501.6 w | | Q | 2 | ? | ? |
| 1501.0 m | -0.3 | 1500.7 s | -0.7 | | | Q | 2 | 11 | 11 |
| | | 1522.7 vs | 0.3 | | | S | 2 | 11 | 13 |
| | | 1504.7 s | -0.6 | | | Q | 3 | 9 | 9 |
| | | 1522.7 vs | -0.3 | | | S | 3 | 9 | 11 |
| | | 1498.7 m | 0.3 | | | Q | 1 | 28 | 28 |
| | | 1548.1 w | 0 | | | S | 1 | 28 | 30 |
| | | 1504.7 s | -0.1 | | | Q | 3 | 24 | 24 |
| | | 1548.1 w | 0.5 | | | S | 3 | 24 | 26 |

*Spectra a, b, c as in Figure 3; ν_{calc} obtained using constants of reference [18] for $\Delta K = 0$ and the indicated values of K'' , N'' , N' .

$$\Delta = \nu_{\text{obs}} - \nu_{\text{calc}}$$

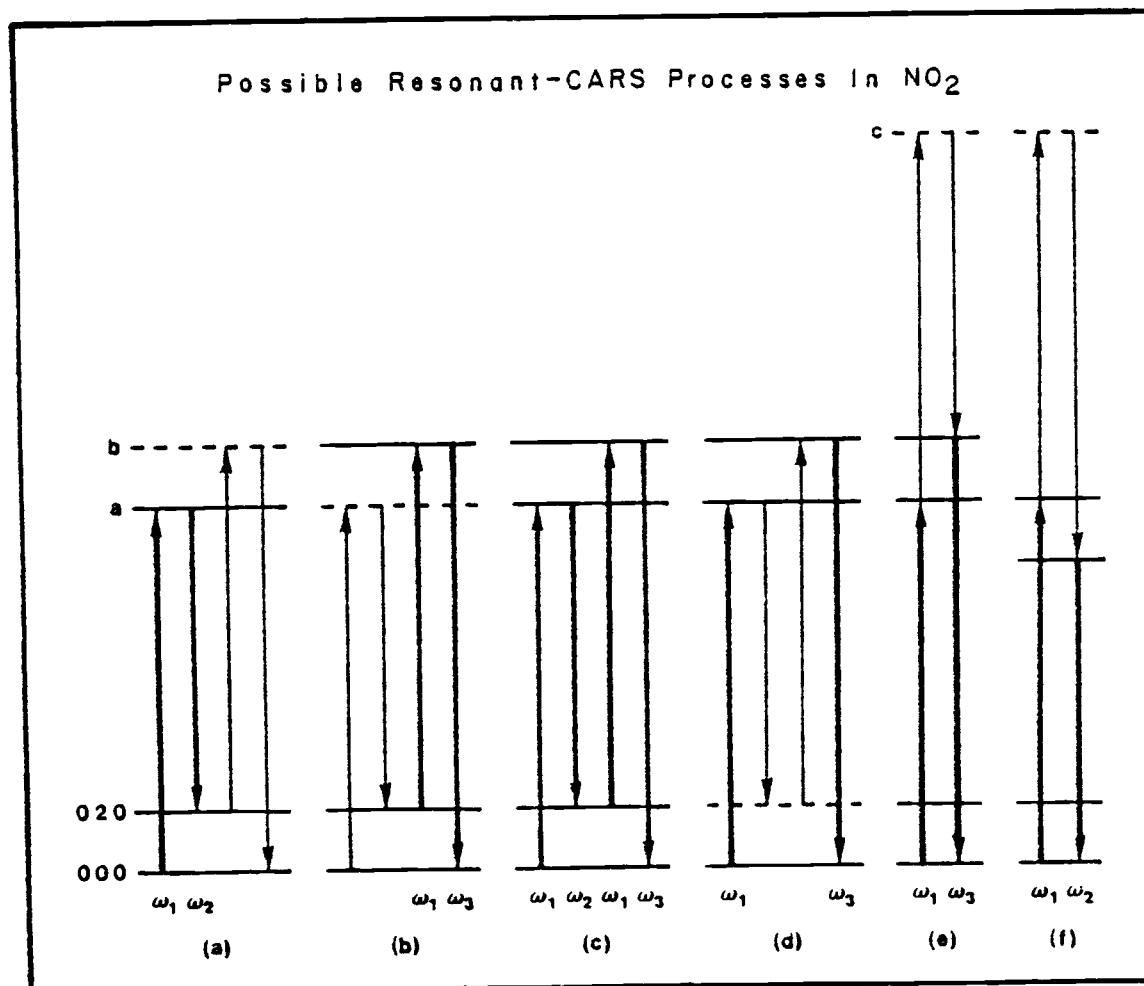


Figure 3.4. Possible resonant processes which could contribute to the CARS spectra of NO_2 . One photon resonances are indicated below the 000 level.

the ω_3 region, some double resonances might occur and the resultant spectrum should correspond to selectively enhanced bands in the ordinary absorption spectrum in the ω_3 (blue) region. It may be noted that process b should be less favorable than a because b requires resonance in ω_1 and ω_3 for the same subgroup of molecules within the Doppler profile. Such a constraint would be even greater in c, the case of maximum resonance, but this might be compensated in part by additional intensity enhancement.

The importance of processes b-f was tested by examining the correlation between the $2\nu_2$ and $3\nu_2$ spectra. If ω_1 is resonant, as in case a, one would expect similar triplets in both regions. Analysis of each region should give identical sets of K'' , N'' , and N' quantum numbers. On the other hand, processes b-f would produce different spectral patterns, in the two regions, and analysis would require detailed knowledge of both vibrational and electronic states. Because of the marked variations in spectra with ω_1 frequency, great care was taken to allow the YAG laser to stabilize. The $2\nu_2$ region was scanned twice, then the dye changed, and the $3\nu_2$ spectrum was recorded. Immediately afterward, the original dye was replaced and $2\nu_2$ scanned again to confirm that the spectrum was unchanged. It was found that the $3\nu_2$ spectrum was very much richer than that of $2\nu_2$ and there were many features which were uncorrelated. From this, and from some frequency and

intensity inconsistencies for assignments of other $2\nu_2$, $3\nu_2$ scans, it is clear that not all spectral features can be attributed to resonant CARS case a.

Evidence against a significant role by processes d-f is provided in Figure (3.5). Here the CARS features in the region near $\omega_3 = 22100 \text{ cm}^{-1}$ ($\omega_1 - \omega_2 \sim 3300 \text{ cm}^{-1}$) are compared with the corresponding absorption spectra in ω_3 and ω_2 regions. Processes d and e should yield a CARS trace similar to the blue ω_3 absorption spectrum while processes f should duplicate the red ω_2 absorption. However, examination shows no significant correlation between these spectra and certainly many of the strongest ω_3 and ω_2 absorptions are completely missing in the CARS spectrum.

For cases b and c, the CARS ω_3 resonance should coincide with some of the ω_3 absorptions. Such coincidences cannot be eliminated, or confirmed, from Figure (3.5) because of the high density of absorptions and because of frequency uncertainties. However, the fact that the $2\nu_2$ and $3\nu_2$ CARS spectra are not correlated is strong evidence that processes b and/or c do contribute to some extent. The dramatic spectral variations when ω_1 is changed very slightly clearly indicates that most, if not all, features are resonantly enhanced. Further evidence

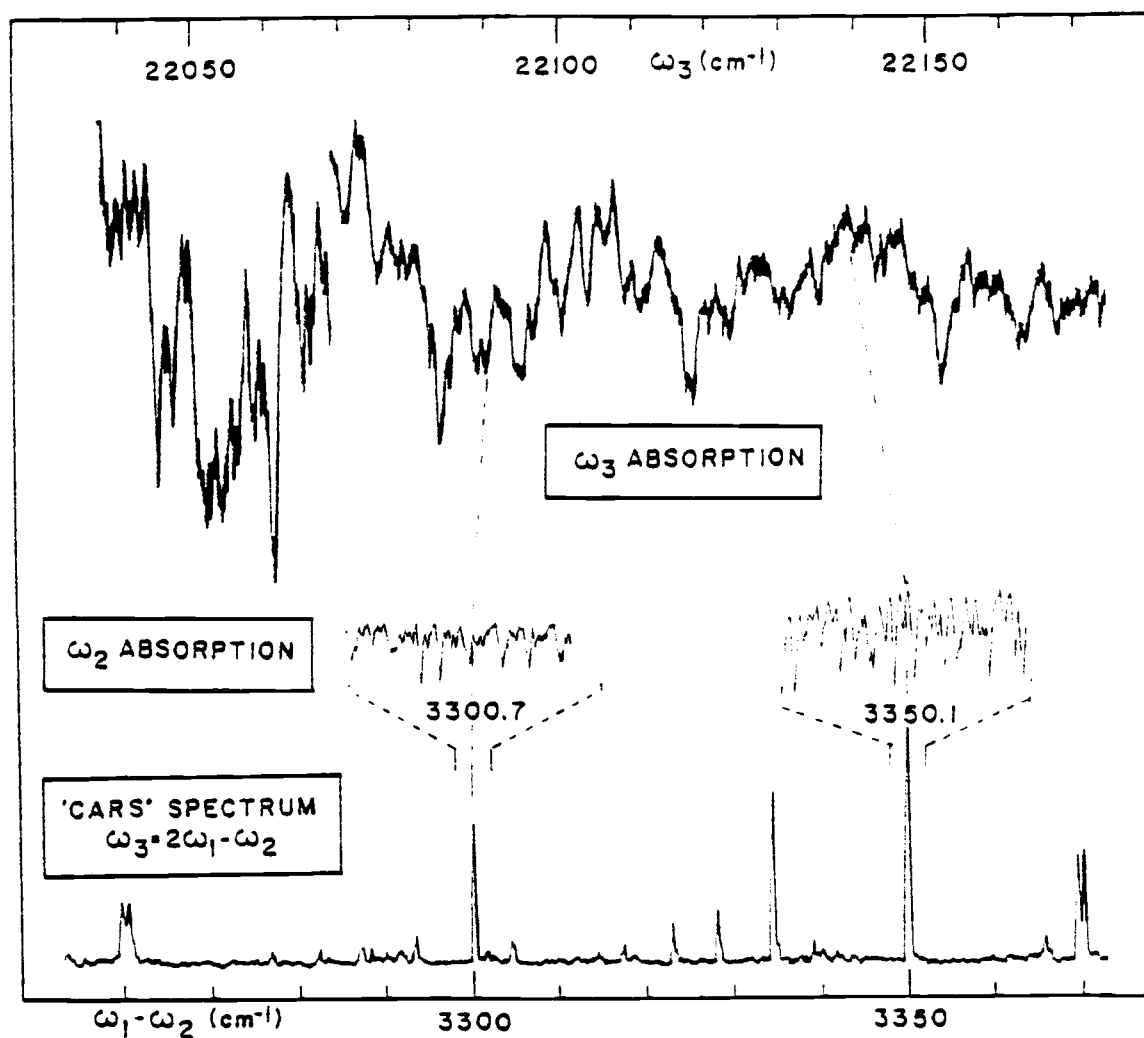


Figure 3.5. Comparison of CARS and ω_2 , ω_3 absorption spectra of NO_2 . NO_2 pressure of ~ 2.5 torr for CARS spectra, and ~ 6 torr for ω_3 absorption spectrum. ω_2 spectrum taken from ref. [45] and shown for a 4 cm^{-1} interval around CARS feature.

for this is the absence of line shape distortions for weak features (caused by χ_{NR} in normal CARS).*

A slight argument against a major role by the "completely resonant" case c can be developed from semiquantitative intensity measurements. The stronger $2\nu_2$ bands of NO_2 (2 torr) appeared with peak intensities which were comparable to the Q branch intensity of 2 torr of O_2 . This result can be contrasted with Taran's observations for I_2 where, for equal pressure, the I_2 signal would be $\sim 10^4$ times that of the Q branch of O_2 . The resonant enhancement process in I_2 must be more effective than in NO_2 . Part of this may be due to a greater dilution of the NO_2 molecules among the many polyatomic vibration-rotation states (compared to diatomic I_2). However, it is also important to note that I_2 has a continuum state which overlaps the discrete ${}^2\Pi_{ou}^+$ state in the visible region. This could ensure complete resonance as in case c and thereby account for the large enhancement. By the same token, the lower enhancement factor observed for NO_2 would imply that process c does not contribute significantly to the CARS spectrum.

*This effect of χ_{NR} on a weak CARS signal is discussed in Chapter 1 and shown in Figure (1.4).

3.D Summary

In summary, a rich vibrational-rotational CARS spectrum for low pressure NO_2 under high resolution conditions was observed. The intensity and dramatic changes as ω_1 frequency is shifted slightly are evidence for a strong resonance enhancement. Comparisons of $2\nu_2$ and $3\nu_2$ spectra show that more than one resonant process contributes the poor correlation between CARS and ω_1, ω_3 absorption spectra allows the elimination of three of the six likely processes. Comparison of the CARS intensity of NO_2 with that of I_2 suggests that "complete" resonance in $\omega_1, \omega_2,$ and ω_3 is not as likely for NO_2 as for I_2 . The resonance enhancement should be beneficial for low-pressure studies (and possibly low concentrations) of NO_2 . In contrast to resonant fluorescence, relaxed emission is not a problem in CARS spectra. The constraints added by the resonance requirements make the spectra sensitive to vibrational-rotational levels in both ground and electronic states. This added information is of dubious gain, however, because of the difficulty in analyzing the resulting irregular pattern of spectral lines.

CHAPTER 4

ELECTRONIC THREE WAVE MIXING SPECTRA OF
TRANSIENT SPECIES PRODUCED BY UV
LASER PHOTOLYSIS OF BENZENE

4.A Introduction

The three wave mixing (3WM) process which describes CARS has already been shown to offer large increases in sensitivity when one and two photon electronic resonance enhancement occurs [42, 30]. Because of the efficiency and short duration of the 3WM process when using pulsed lasers, the technique holds promise for the study of transient species such as those generated by laser or flash discharges. With intense excitation sources, 3WM spectra of excited molecular states or of photofragments should be feasible at low and subtorr pressures, i.e. in a collision free regime. The principal limitation in such applications is likely to be the nonresonant contribution produced at ω_3 in all media because of the response of electrons to the incident laser fields. This requires that the fraction of molecules in a particular molecular state be at least $\sim 0.1\%$ even though the absolute concentration can be quite low. With high intensity lasers, such product concentrations are realizable. Moreover, substantial resonance

*This chapter is abstracted from the published report, with this title, appearing in reference [56]. Additional and more detailed investigations of possible spectral assignments have been included in this chapter.

enhancement of transient signals can occur in many cases and this can lower the relative concentration requirements by several orders of magnitude.

Nibler et al. recently reported the first observation of a CARS spectrum of a transient species [5b]. A 266 nm laser beam was used to photolyze benzene and an intense CARS spectrum was observed in the 2900-3300 cm^{-1} frequency shift region. This corresponds to the CH stretching region and the spectrum was interpreted as due to vibrational resonances of various unknown photoproducts. In the present study, we have extended this work and we report here experiments on a variety of aromatic compounds, all of which undergo efficient photofragmentation of UV laser excitation at 266 or 355 nm. The spectra are extremely intense and appear to involve electronic resonant processes rather than a simple vibrational CARS process. Efforts to identify the transient species and to understand the optical mixing process will be discussed.

4.B Experimental

The basic CARS experimental setup is described in Chapter 2. In addition, fluorescence measurements were made $\sim 5 \text{ cm}^{-1}$ resolution at 90° to the sample with a 0.45 m McKee-Pederson spectrometer equipped with a 1P28A photomultiplier and an f/2 collection lens of 50 mm diameter.

The integrated signal is displayed by a chart recorder as the monochromator is scanned.

Samples of benzene (Mallinckrodt), benzene- d_6 (Norell), toluene (Baker) and chlorobenzene and bromobenzene (Baker) were degassed prior to use. The acetone stabilizer present in the acetylene, was removed by vacuum distillation over a pentane slush trap at -129°C . Spectra from this purified acetylene were identical to spectra from the acetylene-acetone mixture and consequently, the acetylene was taken directly from the lecture bottle for most experiments. These sample gases were introduced through a metering valve into a 15 cm cell fitted with quartz windows. As noted by others [57], prolonged UV photolysis of benzene results in carbonaceous deposits and these were minimized by flowing the benzene at pressures of 1 to 10 torr. Pressures were monitored with a 100 torr Validyne variable reluctance gauge.

4.C General Spectral Characteristics

Figure (4.1) shows the 3WM spectrum obtained for 2.5 torr of benzene vapor when a UV laser excitation beam (termed ω_{266} hereafter) is made collinear with ω_1 and ω_2 beams. The scan covers the region from 800 to 3100 cm^{-1} and the spectrum near 3000 cm^{-1} is essentially the same as that reported earlier [5b]. The spectrum is quite rich and only the major spectral features are listed in Table 4.1. Almost all of the studies to be described have concentrated

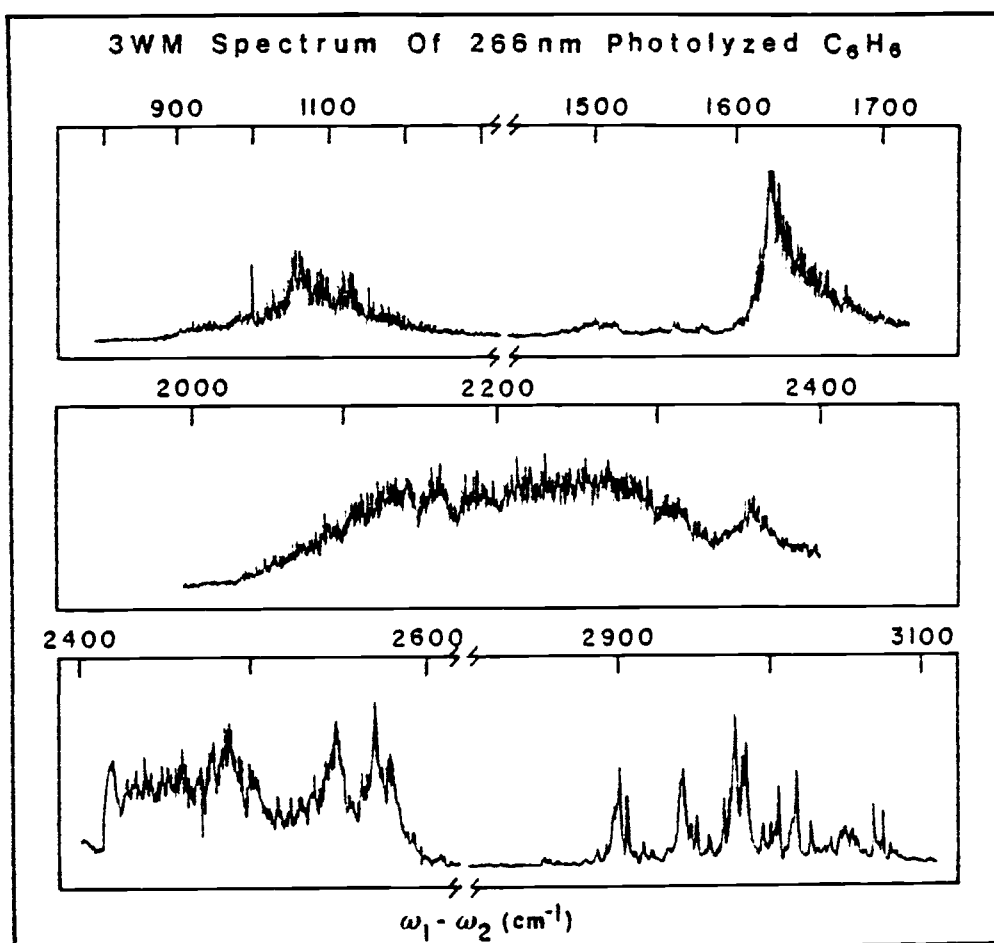


Figure 4.1. 3WM spectrum produced by 266 nm photolysis of 2.5 torr benzene.

Table 4.1. General features of 3WM resonances ($3100-2800 \text{ cm}^{-1}$) of 266 nm photolysis fragments of C_6H_6 , C_6D_6 and C_2H_2 .

| $\text{C}_6\text{H}_6^{\text{a}}$ $\omega_1-\omega_2 \text{ (cm}^{-1}\text{)}$ | $\text{C}_6\text{D}_6^{\text{b}}$ $\omega_1-\omega_2 \text{ (cm}^{-1}\text{)}$ | $\text{C}_6\text{D}_6^{\text{c}}$ $\omega_1-\omega_2 \text{ (cm}^{-1}\text{)}$ | $\text{C}_2\text{H}_2^{\text{d}}$ $\omega_1-\omega_2 \text{ (cm}^{-1}\text{)}$ |
|---|---|---|---|
| 3073 m (ν_1) | 3080 w 3070 m | | |
| 3067 m | | | |
| 3047 w, brd | | | |
| 3038 w | | | 3038 w, brd |
| | 3029 m | | 3026 w |
| 3026 w | | | |
| 3016 s | 3020 m | 3017m 3014 sh | 3016 w |
| | 3008 w | 3005 m | |
| 3004 s | 3003 w | | |
| 2999 w | 2997 w | 2996 m brd | |
| 2993 w | 2993 w | | 2994 m, brd |
| | 2987 vs | 2989 m | 2989 s |
| 2984 s | 2984 s | 2984 vs | 2984 s |
| 2981 s | 2980 vs | 2981 s | 2981 s |
| 2979 vs | 2979 vs | 2975 vs | 2973 s |
| 2971 m | 2972 s | 2969 s | 2968 s |
| | 2963 w | | |
| 2960 w | 2960 m | | |
| 2952 w | 2954 m | 2952 s | 2951 vs |
| 2947 w | 2945 vs | 2946 s, brd | 2946 s |
| 2942 s, brd | 2942 s, brd | 2939 s, brd | 2937 s, brd |
| | 2926 w, brd | | |
| | 2919 w | | |
| | 2913 w, brd | | |
| 2906 m | 2908 m | | |
| | 2903 sh | | |
| 2899 sh | 2900 s, brd | | 2900 w |

Table 4.1 (continued)

| $\text{C}_6\text{H}_6^{\text{a}}$ $\omega_1 - \omega_2$ (cm^{-1}) | $\text{C}_6\text{D}_6^{\text{b}}$ $\omega_1 - \omega_2$ (cm^{-1}) | $\text{C}_6\text{D}_6^{\text{c}}$ $\omega_1 - \omega_2$ (cm^{-1}) | $\text{C}_2\text{H}_2^{\text{d}}$ $\omega_1 - \omega_2$ (cm^{-1}) |
|--|---|---|---|
| 2893 sh | 2888 w | 2895 | 2895 w |
| 2887 w | 2879 w | | |
| 2878 w | 2871 w | | |
| | 2861 w | | |
| | 2851 w, brd | | |
| | 2823 w | | |
| | 2815 w | | |
| $\text{C}_6\text{H}_6^{\text{a}}$ fragment resonances below 2800 cm^{-1} | | | |
| 2580 m | 2356 w, brd | 1690- | sh, brd |
| 2569 s | 2339 w, brd | 1630 | |
| 2562 m | | | |
| 2554 sh | 2300- | 1628 sh | |
| 2550 s | m, vbrd 2200 | 1621 vs 1621 vs | |
| 2545 sh | | 1618 sh | |
| 2502 m, brd | 2186 m, brd | 1614 sh | |
| 2486 s, brd | 2141 m, brd | | |
| 2478 m | 2127 m, brd | 1115 m, brd | |
| 2470 m | 2105 w, brd | 1085 m, brd | |
| 2447 m, vbrd | 2090 w, brd | 1060 m, brd | |
| 2418 m | | 1050 m, brd | |
| | | 995 m (ν_2) | |

$\omega_1 = 18789 \text{ cm}^{-1}$; w = weak; m = medium; s = strong, v = very, sh = shoulder; brd = broad.

^a4-8 mj ω_{266} , P ~ 2-6 torr; ^b4-5 mj ω_{266} , P ~ 2.5 torr; ^c10-12 mj ω_{266} , P ~ 2.5 torr; ^d8 mj ω_{266} , P ~ 10 torr.

on the 2800-3100 cm^{-1} region. Even though benzene does not absorb significantly at 266 nm, nearly complete extinction of the strong ν_1 CARS feature of benzene (3073 cm^{-1}) was observed when ω_{266} was turned on. At the same time the complex spectrum of Figure (4.1) was produced.

The possibility was considered that part of the spectrum of Figure (4.1) might arise from the S_1 state of benzene, populated by 266 nm excitation. This was rejected for several reasons. First, absorption into this state at 266 nm would be very weak and could only occur by hot band absorption. Second, no significant feature was present at the known S_1 symmetric CH stretching frequency of 3135 cm^{-1} , although this band should dominate the CARS spectrum. Finally, spectra of substituted benzenes showed nearly identical features in the CH stretching region (Figure (4.2)), indicating a common fragmentation product.

To probe further the identity and mechanism of production of the species responsible for the spectra shown in Figures (4.1) and (4.2) a number of experiments were conducted. First, it was confirmed that all three beams were required for signal production. Spectral examination of the signal beam in the forward direction showed that, for each choice of ω_2 , a coherent beam was generated only at $\omega_3 = 2\omega_1 - \omega_2$. This eliminated the possibility that the signal was a frequency dependent fluorescence and established the 3WM character of the spectrum. Next, it was demonstrated that

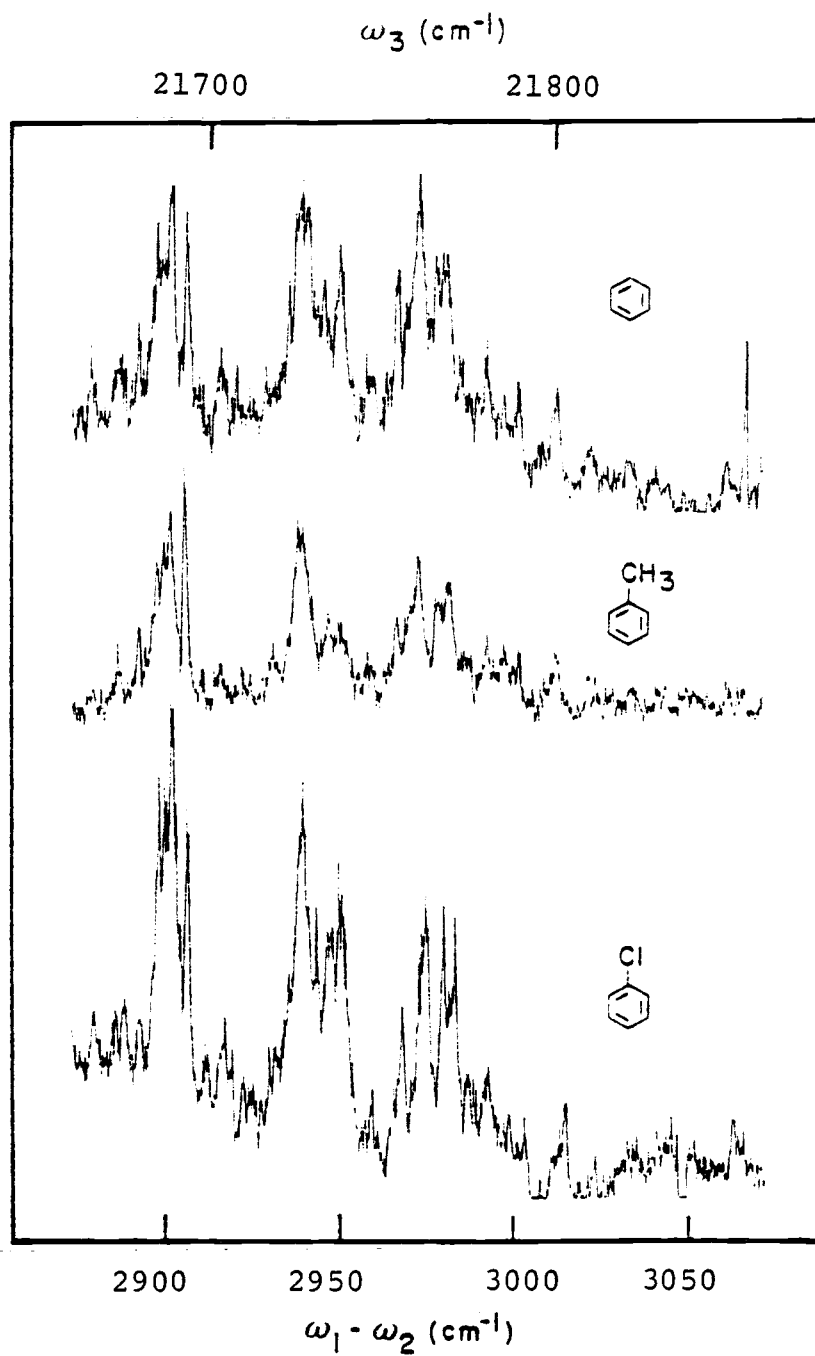


Figure 4.2. 3WM spectra produced by 266 nm photolysis of 2.5 torr benzene, toluene, and chlorobenzene.

ω_{266} served only to generate the fragments and did not somehow mix with ω_1 and ω_2 in producing the spectrum. For example, the 3WM spectrum near 3000 cm^{-1} was unchanged on rotating the ω_{266} polarization by 90° relative to parallel polarizations of ω_1 and ω_2 . Reversing the direction of ω_{266} propagation relative to ω_1 and ω_2 also had no effect. Most convincing however, was the observation that the spectrum remained unaltered when the 10 nsec ω_1 and ω_2 beams were optically delayed 15 nsec to eliminate any temporal overlap with ω_{266} .

4.D Photolysis Behavior

It is believed that the fragmentation process must involve more than one 266 nm photon since no photochemistry has been reported for benzene for wavelengths above 250 nm. Slight variations in relative ω_3 band intensities were observed as the power of the ω_{266} beam was changed. Intensity measurements of several lines were made to try to determine whether two or three ω_{266} photons were involved in generating these features. Unfortunately the results were not very reproducible because of variable thermal focusing produced by ω_{266} , ω_1 and ω_2 with the quartz attenuators available. This resulted in large signal variations due to changes in the critical overlap of the beams in the focal volume. At high powers, problems with signal saturation also can affect intensity measurements and, finally, the multi-shot averaging process can lead to

complications for a nonlinear signal (e.g. $\bar{P}_3 = \overline{kP_1^2 P_2^n} \neq k\bar{P}_1^2 \bar{P}_2^n$). For these reasons, all that can be said at this point is that the photolysis process is not inconsistent with either two (133 nm) or three photon (89 nm) absorption. It may also be noted that a 355 nm photolysis source produced similar, though not identical (and much weaker), spectra in the 2800-3100 cm^{-1} region even though benzene definitely does not absorb at 355 nm.

Since ω_{266} has a duration of only ~ 8 nsec, multi-photon fragmentation at low pressures (1-2 torr) must be a unimolecular process (at one torr, the C_6H_6 collision time is ~ 90 nsec). The spectra are thus believed to be characteristic of newly born fragments with energy distributions which are unaltered by molecular collisions. Of course, it might be argued that the spectra are not due to primary photofragments produced by a given ω_{266} flash but are rather due to secondary products resulting from earlier ω_{266} photolysis pulses. That such was not the case was confirmed by several experiments. First, the C_6H_6 was allowed to flow through the cell at a rate such that most secondary products were removed between flashes. In addition it was observed that the CARS signal of the prominent feature near 2942 cm^{-1} was produced immediately on one pulse of all beams. An even more convincing demonstration of this is provided in the broadband spectrum shown in Figure (4.3). This trace was obtained in a single laser pulse of a fresh sample by

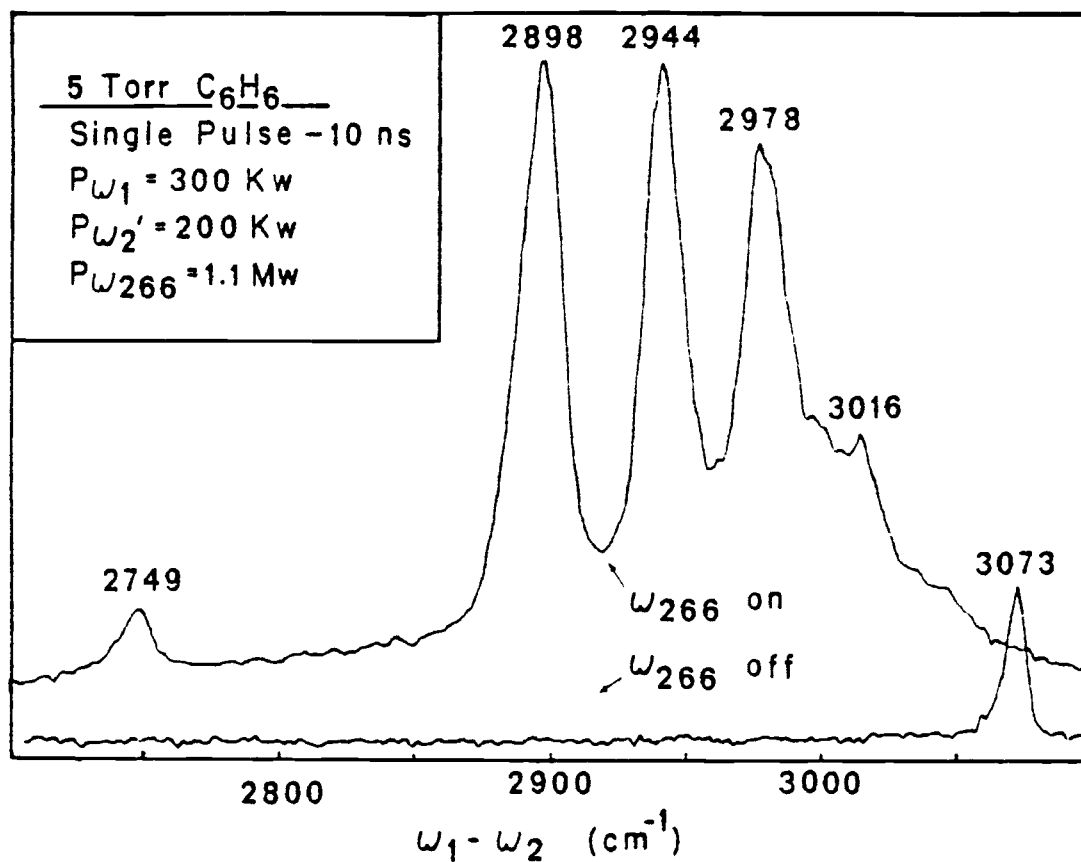


Figure 4.3. Single pulse broadband 3WM spectrum of 5 torr benzene. Upper trace with ω_{266} present, lower trace ω_{266} absent. Both traces with same intensity scale.

using an intensified optical multichannel analyzer and a ω_2 dye laser beam of $\sim 400 \text{ cm}^{-1}$ width. The lower trace shows the 3073 cm^{-1} benzene feature in the absence of ω_{266} while the top spectrum displays the intense 3WM fragment spectrum at low resolution. The general features of Figure (4.1) are adequately reproduced and there can be no doubt that most, if not all, of the spectral bands are due to primary products.

4.E Photolysis of Substituted Benzenes

Vacuum UV absorption is known to occur for benzene from one photon photochemical studies and observed products include excited states of C_6H_6 , C_6H_6^+ , isomers of benzene which result from ring opening, C_6H_5 and smaller fragments [57-59]. Nothing is known about the species produced by two photon absorption since the parent C_6H_6 states cannot be accessed by one photon, but it is likely that similar products should result. To identify some of these, studies were made of several substituted benzenes.

Figure (4.2) displays the fragment spectra of benzene, toluene and chlorobenzene in the $2800\text{-}3100 \text{ cm}^{-1}$ region. The general features are quite similar although the intensities for the latter compounds were noticeably higher at comparable conditions. This could be due to increased photolysis efficiency because of better overlap of ω_{266} and the S_1 states of $\text{C}_6\text{H}_5\text{CH}_3$ and $\text{C}_6\text{H}_5\text{Cl}$. The spectra

strongly suggest that a common fragment is formed and detected for all three parents. The phenyl radical, C_6H_5 , would thus seem to be a likely candidate since it is known to be produced from conventional flash photolysis studies of such compounds [58]. That such is not the case became apparent from studies of deuterated benzene.

3WM spectra of the 266 nm photofragments of C_6D_6 are shown in Figure (4.4a and b) at low (4-5 mj) and high (10-12 mj) ω_{266} energies and $\omega_1 - \omega_2$ frequencies are given in Table (4.1) for the region above 2800 cm^{-1} . As can be seen, the low power spectrum is nearly identical to the spectrum of undeuterated benzene in the corresponding "CH stretching" region (see Figures (4.1) and (4.2)). Though not shown, the spectrum in the CD stretching region near 2200 cm^{-1} resembles that for C_6H_6 in Figure (4.1) and there is no isotope effect of the spectral features in the 'CH' region. This result is compelling evidence against a contribution by a C_6H_5 fragment and, moreover, argues strongly that the fragments responsible for the spectrum must not contain CH bonds.

The rich structure in the "CH region" is also difficult to understand in terms of any fundamental, vibrational frequency of a C_n fragment. Only overtone and combination bands of C-C stretching would be so high in frequency. Consequently, it seems likely that most, if not all, of the 3WM bands do not correspond to simple

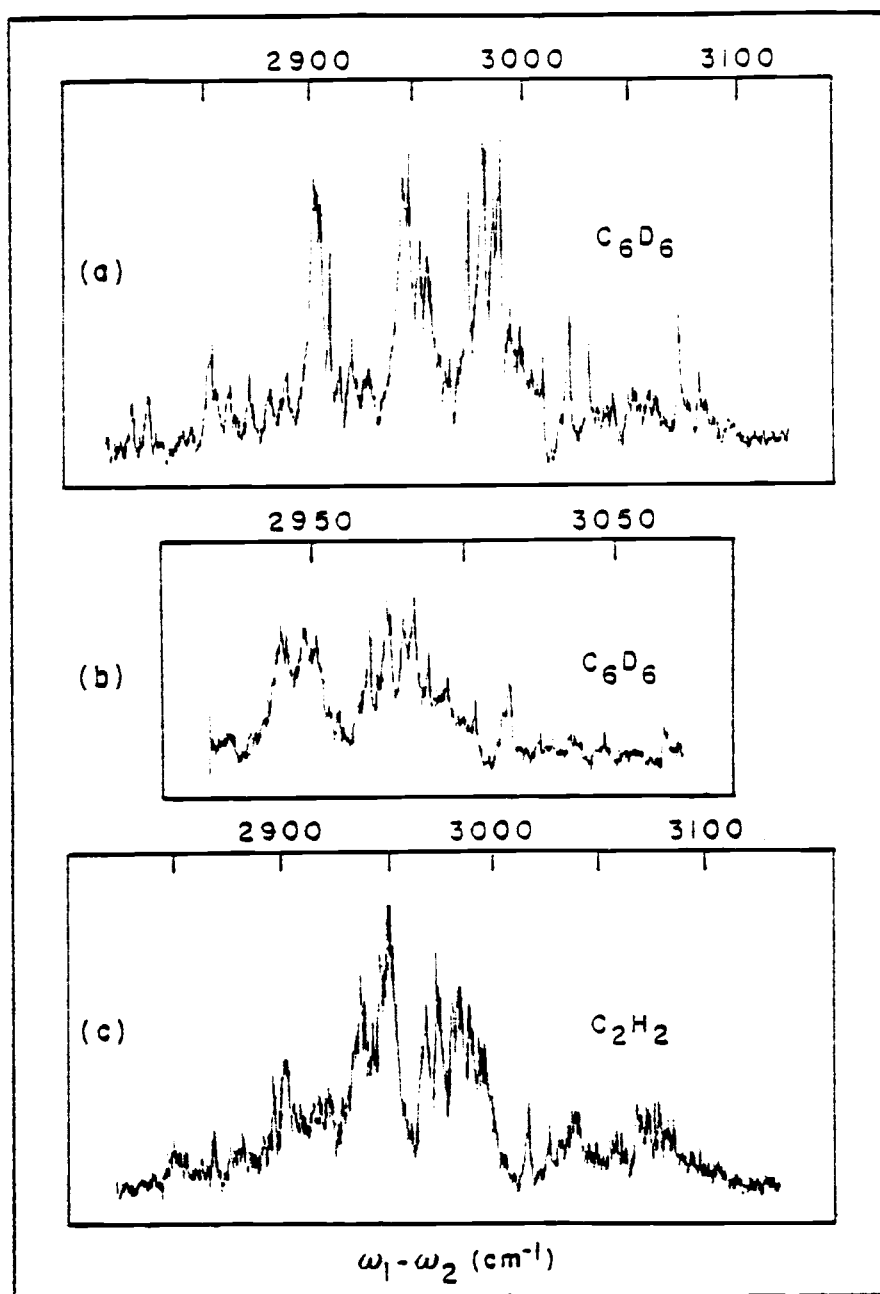


Figure 4.4. 3WM spectra produced by 266 nm photolysis of C_6D_6 and C_2H_2 . (a) and (b) show the effects of ω_{266} energy [~ 5 mJ for (a) and ~ 12 mJ for (b)] on 5 torr C_6D_6 . In spectrum (c) the pressure was ~ 10 torr and ω_{266} energy ~ 8 mJ.

vibrational CARS resonances unless electronic enhancement occurs. After describing other experiments aimed at identifying some of the fragmentation products, the consideration of resonant 3WM processes will be returned to

4.F Identification of Photofragments

The C_6D_6 results imply that a C_n fragment is responsible for the spectrum in the 3000 cm^{-1} region and hence several simpler precursors were examined to determine n . A spectrum of CH_4 showed no indication of the fragment spectra, even under high pressure-power conditions where some slight discharge breakdown occurred and the ν_1 CH stretching band of CH_4 was reduced in intensity. However, 266 nm photolysis of acetylene occurred quite readily and Figure (4.4c) displays the resultant spectrum. It is apparent that this spectrum is similar to those shown for the benzene derivatives in Figures (4.1, 4.2, and 4.4a, b). The correspondence is particularly good with spectrum (4.4b) since both were run under similar conditions of high ω_{266} power. Because the time duration is too short to allow extensive aggregation following the fragmentation step, these results point to C_2 as the fragment responsible for the 3WM spectra in at least the 3000 cm^{-1} region. Different fragment states could occur for different precursors and photolysis powers and hence the relative intensity variations of Figures (4.4a, b, and c) are not

unreasonable. It may also be noted that McDonald and co-workers have recently shown that C_2 (and CH) are 193 nm multiphoton fragmentation products of acetylene [60].

Confirmation of the production of C_2 in the fragmentation of C_6H_6 was obtained by examining the emission produced on 266 nm excitation. Figure (4.5) shows the 90° fluorescence spectrum which is unmistakably due to Swan band transitions in the region near 470 nm. This establishes that C_2 in the $d\ 3\pi_g$ state ($v' = 0-4$) is produced by ω_{266} photolysis, either by direct fragmentation or by secondary absorption of an intermediate. In addition, fluorescence was observed from other states of C_2 ($e\ 3\pi_g$, $a\ 3\pi_g$ and $C, C'\ 1\pi_g$, $A\ 1\pi_u$). Comparable emission from products such as CH and C_3 was not found in their characteristic band systems near 400 nm. However, 90° fluorescence excitation spectra of the $v''=2$ level of the $a\ 3\pi_u$ state were easily obtained using the ω_2 source which was coincident in time and duration with ω_{266} . This identifies the $a\ 3\pi_u$ state as one of the primary photofragments of C_6H_6 . It is less certain whether the higher electronic states of C_2 are primary products since secondary excitation of lower states by ω_{266} , ω_1 or ω_2 could occur. It may be noted that collisional processes do not seem to be responsible in the production of the $d\ 3\pi_g$ state since the Swan band emission was not detectably delayed (<10 nsec) relative to the ω_{266} pulse.

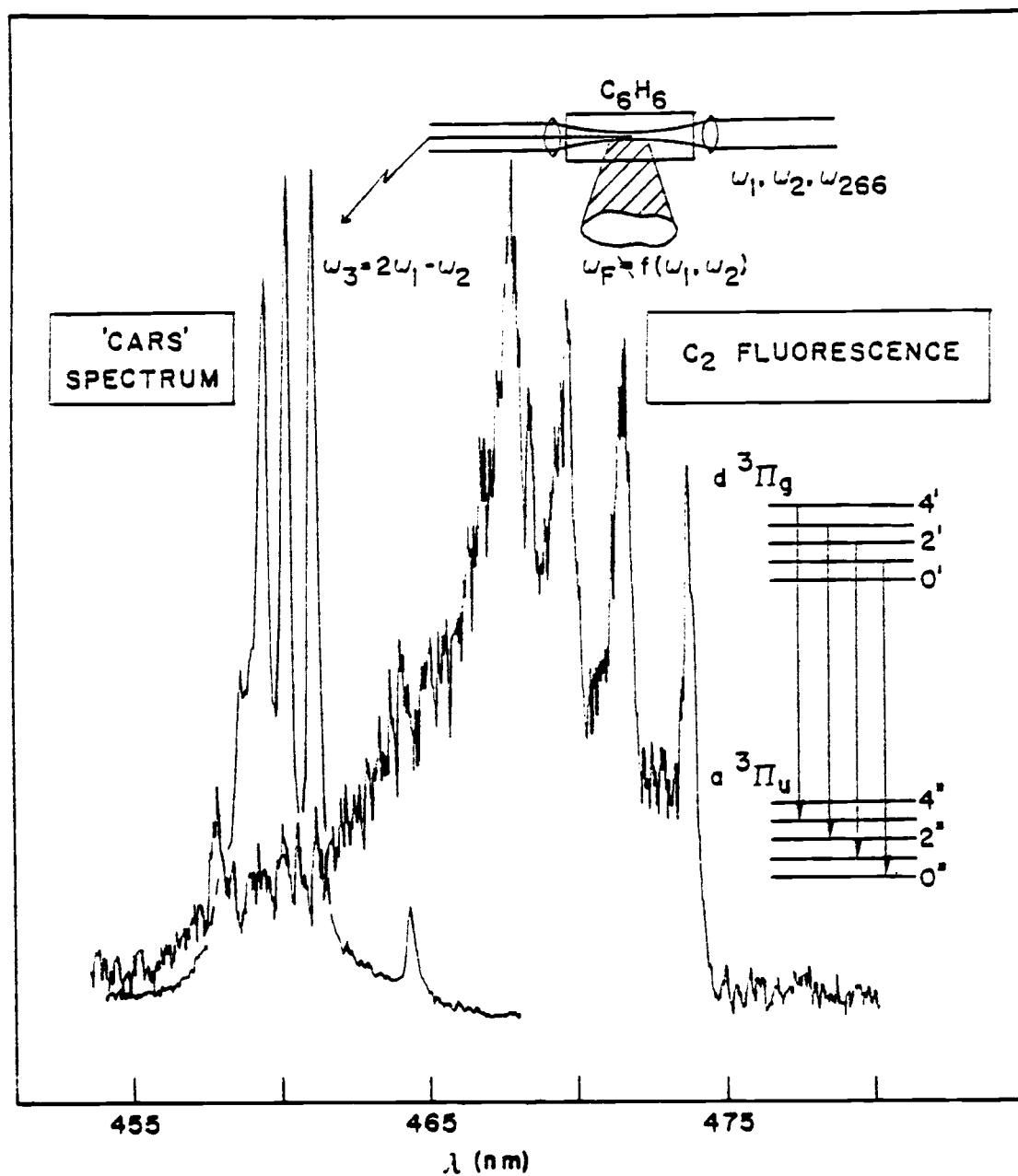
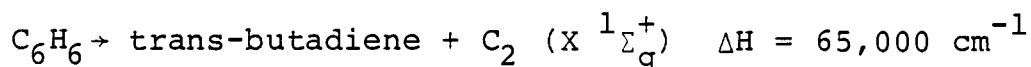


Figure 4.5. Comparison of the 3WM and the C_2 Swan band fluorescence spectra produced by 266 nm photolysis of benzene.

4.G Fragmentation Process

Although this work reveals few details regarding the precise photochemistry involved in producing C_2 , some observations can be made from energetic considerations. One photon at 266 nm is equal to $37,575 \text{ cm}^{-1}$ so that $2\omega_{266} = 75,152 \text{ cm}^{-1}$ and $3\omega_{266} = 112,728 \text{ cm}^{-1}$. The minimum energy requirement for production of C_2 from benzene would appear to occur for the reaction.



Other C_4H_6 isomeric products would raise ΔH by $\sim 3000 \text{ cm}^{-1}$ while further fragmentation would require additional energy. Of course, it should be stressed that no direct observation of any C_4H_6 isomer was made (infrared examination of a cell with a static C_6H_6 pressure of 10 torr showed only C_2H_2 and C_6H_6 after extended 266 nm photolysis). Nonetheless, if butadiene (unexcited) is assumed to be a primary product, then the following energy requirements exist for production of the observed excited states of C_2 :

| | | | |
|----|-----------|---------------|--|
| a | $^3\Pi_u$ | (v = 2) | $\Delta H = 75,400 \text{ cm}^{-1}$ |
| d | $^3\Pi_g$ | (v = 1-5) | $\Delta H = 93,300 - 98,400 \text{ cm}^{-1}$ |
| c | $^1\Pi_g$ | (v = 0, 1) | $\Delta H = 105,800 - 107,600 \text{ cm}^{-1}$ |
| c' | $^1\Pi_g$ | (v = 1, 2) | $\Delta H = 110,700 - 112,400 \text{ cm}^{-1}$ |
| e | $^3\Pi_g$ | (v = 0, 1, 2) | $\Delta H = 112,000 - 114,000 \text{ cm}^{-1}$. |

Two ω_{266} photons thus contain enough energy to produce C_2 only in low vibrational levels of the $X^1\pi_g^+$ and a $^3\pi_u$ state. In fact, spin conservation would require a triplet C_4H_6 counterpart with the a $^3\pi_u$ state and this extra energy would probably necessitate an additional ω_{266} photon. Thus, it appears most likely that all the C_2 states observed in the fluorescence experiments arise from a minimum of three photons of ω_{266} (88.7 nm). The one photon vacuum UV spectrum shows a strong continuum absorption in this region [61] but the primary photofragments have not been reported. It is also possible the photolysis involves two photon excitation of C_6H_6 to produce $C_6H_6^*$ or a C_6H_6 isomer such as fulvene [57-60]. These products could then absorb an additional photon at ω_{266} and fragment to yield C_2 in its various states. A choice between these alternate fragmentation mechanisms is not possible from the present results.

In fact, a third mechanism for fragmentation of C_6H_6 must also be considered. One photon ionization of C_6H_6 is known to occur for excitation above 74575 cm^{-1} and it is quite possible that photoelectrons could result from absorption of either two or three photons of ω_{266} . Such electrons can extract energy from the radiation fields by inverse-Bremsstrahlung absorption [62, 63]. At high pressures, these energetic electrons produce collisional fragmentation and ionization of other molecules in the focal

volume. Gas breakdown can thus occur by cascade ionization, resulting in a plasma with broad visible emission and an acoustic 'snap'. Such plasmas were observed in benzene and other gases at pressures above ~ 50 torr but not at the 1-10 torr conditions used in these experiments. However, it is possible that electron energies may be sufficient for efficient collisional fragmentation of C_6H_6 even though the lower pressures may inhibit cascade ionization. To test this fragmentation mechanism, the 3WM spectra were recorded for mixtures of C_6H_6 and CH_4 . The intensity of the ν_1 CH_4 CARS band was found to be only slightly reduced at ω_{266} excitation powers which drastically reduced the ν_1 CARS feature for C_6H_6 . Since the electron collision fragmentation process is not expected to discriminate appreciably against CH_4 , most of the photoproducts detected in this work are believed to arise from unimolecular dissociation of excited C_6H_6 . Further experiments would be desirable to ascertain the relative importance of electron collisional fragmentation of molecules such as C_6H_6 and C_2H_2 . The combination of simultaneous 3WM and photoionization current measurements are planned by J. W. Nibler to explore this problem in the near future [64].

4.H Possible 3WM Processes

The fluorescence results establish that C_2 is produced in a variety of electronic states with known vibrational fundamentals [e.g. $e^3\pi_g$ (1028 cm^{-1}), $a^3\pi_u$ (1618 cm^{-1}), $C'^1\pi_g$ (1697 cm^{-1}), $d^3\pi_g$ (1755 cm^{-1}) and $C^1\pi_g$ (1777 cm^{-1})] [56]. It also seems reasonable to assume that the C_2 fragments populate the multitude of vibrational and rotational states contained in these electronic states. With such a dilution of population, most of the observed features are not expected to result from simple vibrational-rotational CARS of diatomic C_2 . It is tempting, however, to examine possible fundamental, combination, and overtone bands of C_2 to account for at least part of the 3WM spectrum. For example, it is conceivable that the strong 3WM band near 1620 cm^{-1} is a vibrational CARS spectrum to be associated with the $a^3\pi_u$ state and some of the shoulder extending to 1700 cm^{-1} could derive from hot band CARS transitions involving C' , d , and C states. However, closer examination shows that the spectra do not fit the pattern expected for a simple diatomic molecule and, even more important, the intensities are much too strong for the small amounts of C_2 which are produced in any given state (contrast in Figure (4.4), for example, the ν_1 CARS intensity of pure, unphotolyzed benzene at 3073 cm^{-1} with that observed on fragmentation into a multitude of states).

For spectral features above 2000 cm^{-1} , a simple vibrational explanation is even less tenable. For example, one might attempt to assign the bands near 3000 cm^{-1} as overtone transitions of some of the C_2 states which have energies that could permit added electronic resonance enhancement. Figure (4.6) shows the C_2 energy levels below $40,000\text{ cm}^{-1}$. Resonance cases (4.6a) and (4.6b) represent favorable instances, for such an interpretation, involving overtones of the higher levels of the $A\ ^1\pi_u$ and a $^3\pi_u$ states, respectively. From a crude first examination, the fit to the observed frequencies is not particularly good and there is no reason not to expect similar enhancement for the (unobserved) fundamental bands near 1500 cm^{-1} . The possibility of selected electronic resonance enhancement, however, cannot be so quickly dismissed and a more careful consideration of such assignments is in order. Since the strongest 3WM features occur near the Swan band emission, Figure (4.5), a detailed investigation of possible resonances in this region was undertaken.

Figure (4.7) shows two possible resonance processes involving transitions within the triplet Swan system. One photon resonance in ω_1 , Figure (4.7a), or in ω_3 , Figure (4.7b), are considered. The selection rules governing one photon transitions between states $a\ ^3\pi_u$ and $d\ ^3\pi_g$, for the light diatomic C_2 , depend on the degree of coupling of the total electronic spin, S , to the angular momentum along

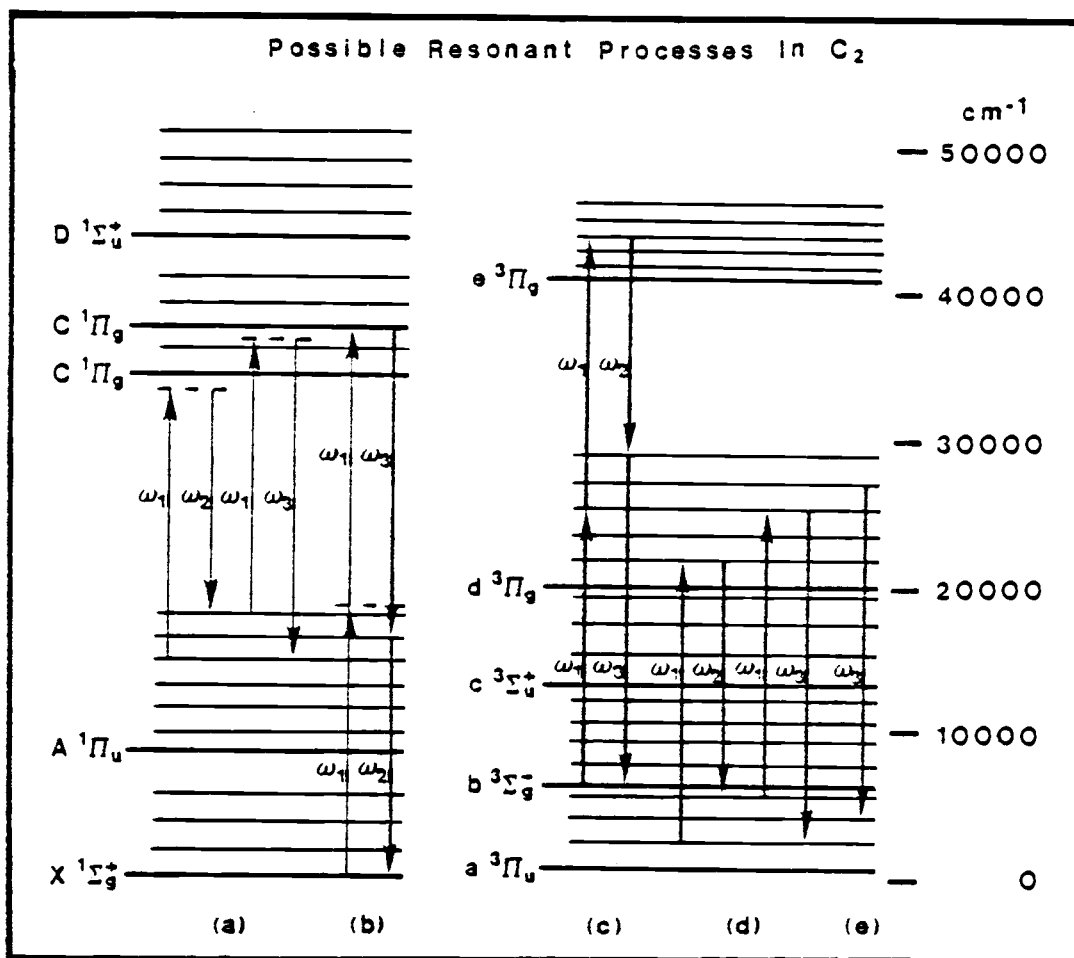


Figure 4.6. Energy level diagram of singlet and triplet states of C_2 . (a) 3WM process involving a vibrational resonance with electronic enhancement due to C and C' singlet states; (b,c) 3WM processes involving one photon electronic resonances in ω_2 or ω_3 with additional enhancement because of $2\omega_1$ and ω_1 resonances; (d) 3WM process involving a vibrational resonance with electronic enhancement due to a and d triplet states; (e) stimulated emission process for excited C_2 which might be produced by the non-resonant 3WM field at ω_3 .

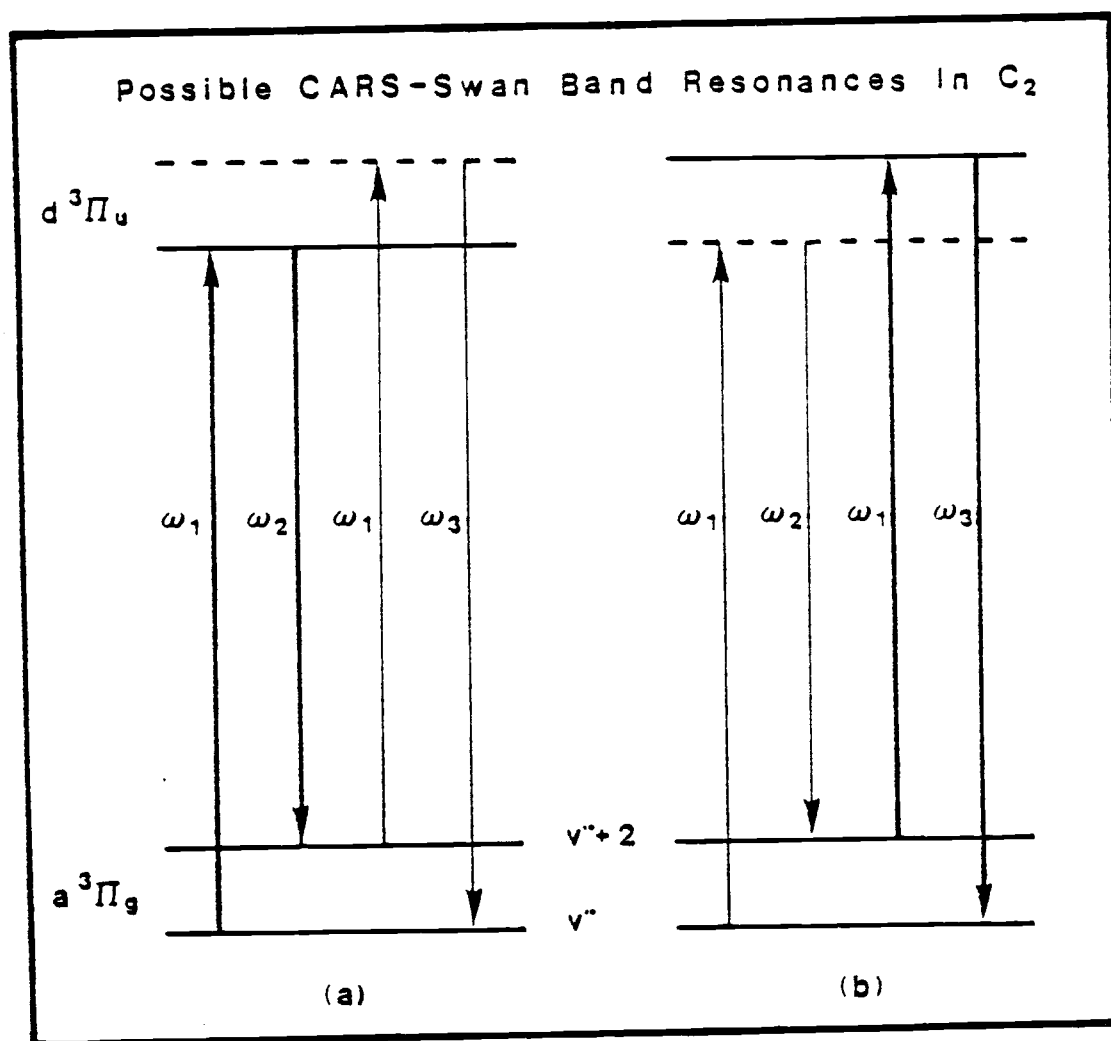


Figure 4.7. Energy level diagram of the a and d triplet states of C_2 . Two possible 3WM processes involving a vibrational overtone resonance, $\Delta v = 2$, with electronic enhancement due to multiple Swan band resonances in either ω_1 and ω_2 , (a), or in ω_1 and ω_3 , (b).

the internuclear axis. C_2 undergoes a rapid transition from Hund's case a to case b with increasing total rotational angular momentum, J

$$J = K + S$$

where K is the resultant total angular momentum excluding spin. For case a $^3\Pi$ states, $S = 1$, $L = 1$ and the $2S + 1$ values of the resultant angular momentum, Ω , about the internuclear axis are

$$\Omega = |\Lambda + \Sigma| = 0, 1, 2$$

where Λ and Σ are the quantum numbers for the projections of L and S on the internuclear axis. These values of Ω give three $^3\Pi$ sublevels designated as $^3\Pi_0$, $^3\Pi_1$, and $^3\Pi_2$. For Hund's case b, S is only weakly coupled to the internuclear axis (making Ω no longer a "good" quantum number), and these three sublevels correspond to angular momentum relationships between K and J of $K = J - 1$, $K = J$, and $K = J + 1$ respectively. The Hund's case b selection rules for $^3\Pi - ^3\Pi$ transitions can be summarized by [54]

$$\Delta J = 0, \pm 1 \quad \text{if } J \neq 0$$

$$\Delta J = \pm 1 \quad \text{if } J = 0$$

$$\Delta K = 0, \pm 1$$

and

$$\Delta J - \Delta K = 0, \pm 1 .$$

If either ω_1 or ω_3 are involved in a resonance between states $a^3\pi_u(v'', J'')$ and $d^3\pi_g(v', J')$ the possible values of J' are

$$J' = J'', J'' + 1, J'' - 1$$

corresponding to Q, R, and P branch Swan transitions, respectively. The intermediate state, $a^3\pi_u(v'' + 2, J''')$ is then coupled to the upper state, $d^3\pi_g(v', J')$, by either ω_3 , Figure (4.7a), or by ω_1 , Figure (4.7b). Since this process is also governed by the same selection rules, the possible values of J''' are

$$J''' = J', J' + 1, J' - 1 .$$

Thus, for a given Swan band resonance, three Raman transitions are possible. For example, if the resonance involves a Swan R branch transition, $J' = J'' + 1$, the three values for J''' , in terms of the initial state J'' value, would be

$$J''' = J'', J'' + 1, J'' + 2$$

corresponding to Raman Q, R, and S branch transitions, respectively. Similarly, a Swan Q branch resonance would yield a Raman P, Q, and R triplet and a Swan P branch resonance would result in a O, P, and Q branch Raman triplet. A computer program was written to calculate these possible resonances which could account for Raman features in the 2800-3100 cm^{-1} region. The energies of the $a^3\pi_u$ and $d^3\pi_g$ electronic states were calculated by conventional functions of vibrational quantum numbers, $v = 0 - 10$, and rotational quantum numbers, $J = 3 - 175$, using the vibrational and rotational constants given by Phillips and Davis [66]

In searching for possible ω_1 resonances, Figure (4.7a), all Swan transitions

$$\omega_1 = d^3\pi_g(v', J') - a^3\pi_u(v'' + 2, J''')$$

within $\sim 5 \text{ cm}^{-1}$ of ω_1 (18789 cm^{-1}) were tested to see if energies involved in the return to the intermediate state by ω_2 ,

$$\omega_2 = d^3\pi_g(v' J') - a^3\pi_u(v'' + 2, J''') ,$$

satisfied the requirement that $\omega_1 - \omega_2$ be within the region of interest (2800-3100 cm^{-1}). A similar search was carried out for possible ω_3 resonances, Figure (4.7b), with the range $\omega_3 = \omega_1 + (2800-3100 \text{ cm}^{-1})$. The Swan resonance in ω_3 is given by

$$\omega_3 = d \ ^3\pi_g(v', J') - a \ ^3\pi_u(v'', J'') ,$$

All such ω_3 transitions need to be coupled to the intermediate state by resonance within $\sim 5 \text{ cm}^{-1}$ of ω_1 such that

$$\omega_1 = d \ ^3\pi_g(v', J') - a \ ^3\pi_u(v'' + 2, J''') .$$

These calculations were carried out for all possible transitions within each triplet sublevel ($\Delta J - \Delta K = 0$), and for some of the many possible transitions between adjacent sublevels ($\Delta J - \Delta K = \pm 1$). The results of these calculations are listed in Table (4.2).

Also listed in Table (4.2) are the measured $\omega_1 - \omega_2$ frequencies of high resolution 3WM spectra from the 266 nm photolysis of C_6H_6 and C_2H_2 , Figure (4.8). These spectra were obtained with a broadband ω_2 source and an intensified optical multichannel analyzer (OMA) mated to a Spex model 1402 spectrometer as detailed in Chapter 2. Great care was taken to maintain constant UV intensity and ω_1 frequency stability during these experiments. The obvious striking similarity of the spectral features can be taken as strong evidence that a common photofragment is responsible for both sets of spectra.

In describing the possible resonances, in Table (4.2) all attempts were made to abide by the conventional labeling scheme for electronic transitions [54]. However, it was found useful to expand upon this in order to keep track

Table 4.2. Observed high resolution 3WM spectral features (2800-3100 cm^{-1}) of 266 nm photolyzed C_6H_6 and C_2H_2 , and calculated Swan band resonances.

| C_6H_6^a ($\omega_1 - \omega_2$) cm^{-1} | C_2H_2^b ($\omega_1 - \omega_2$) cm^{-1} | Calc. ($\omega_1 - \omega_2$) cm^{-1} | Assignment | | | Res. ^c case |
|--|--|---|---|---|------|---------------------------|
| | | | $R_{m,n}S_{w,n}^d$ | (J) | Band | |
| | | 3081.1 | $S_{32}R_3$ | (56) | 5-4 | b |
| | | 3079.9 | $Q_{23}R_2$ | (57) | 5-4 | b |
| 3073.8 (ν_1) | 3074.7 | 3074.0 | S_3R_3 | (143) | 3-3 | b |
| 3072.6 | 3073.5 | 3072.7 | S_2R_2 | (120) | 6-6 | b |
| | | 3054.4 | $Q_{23}P_2$ | (90) | 2-3 | a |
| | | 3052.0 | Q_1R_1 | (70) | 1-0 | b |
| | | 3051.3 | $\left\{ \begin{array}{l} Q_3R_3 \\ Q_2R_2 \end{array} \right.$ | $\left. \begin{array}{l} (68) \\ (69) \end{array} \right\}$ | 1.0 | b |
| 3042.8 | | 3042.8 | $S_{21}R_2$ | (51) | 4-5 | a |
| | | 3042.2 | $Q_{12}P_1$ | (94) | 4-3 | b |
| 3041.5 | | 3041.9 | $Q_{12}R_1$ | (52) | 4-5 | a |
| | | 3041.3 | $Q_{23}R_2$ | (51) | 4-5 | a |
| 3040.3 | | | | | | |
| 303.92 | 3040.2 | 3039.4 | $S_{32}R_3$ | (50) | 4-5 | a |
| 3038.2 | 3039.0 | 3038.2 | $Q_{12}P_1$ | (91) | 2-3 | a |
| 3037.1 | 3037.9 | 3037.7 | $S_{21}R_2$ | (57) | 6-5 | b |
| 3036.0 | 3036.8 | | | | | |
| 3035.0 m | 3035.6 m | | | | | |
| 3033.7 | 3034.7 | 3034.0 | $Q_{12}R_1$ | (58) | 6-5 | b |
| 3032.7 | 3033.4 | 3032.4 | $S_{32}R_3$ | (56) | 6-5 | b |
| 3031.6 | 3032.3 | | Q_2R_2 | (63) | | |
| | | | $\left\{ \begin{array}{l} Q_3R_3 \\ Q_1R_1 \end{array} \right.$ | $\left. \begin{array}{l} (62) \\ (64) \end{array} \right\}$ | 2-1 | b |
| 3028.2 | 3029.1 | | | | | |
| 3027.2 | 3028.0 | | | | | |
| 3026.2 | 3026.8 | | | | | |
| 3024.9 s | 3025.9 s | | | | | |
| 3023.9 | 3024.5 | | | | | |
| 3022.6 | 3023.6 | | | | | |

Table 4.2 (continued)

| $C_6H_6^a$ ($\omega_1 - \omega_2$) cm^{-1} | $C_2H_2^b$ ($\omega_1 - \omega_2$) cm^{-1} | Calc. ($\omega_1 - \omega_2$) cm^{-1} | Assignment | | | Res. ^c case |
|---|---|--|-------------------|-------|------|---------------------------|
| | | | $R_{mn} S_{wn}^d$ | (J) | Band | |
| 3021.6 | | | | | | |
| 3020.6 | 3021.3 | | | | | |
| 3019.3 | | | | | | |
| 3018.2 | | | | | | |
| 3017.2 | | | | | | |
| 3015.8 | | | | | | |
| 3014.7 | 3015.7 | | | | | |
| | | 3001.6 | $Q_{12}P_1$ | (86) | 5-4 | b |
| 2997.8 | | 2998.5 | S_2R_2 | (133) | 8-6 | b |
| 2996.5 | | 2996.9 | $Q_{23}P_2$ | (86) | 3-4 | a |
| 2995.5 | 2996.2 | | | | | |
| 2994.2 | 2995.0 | 2994.4 | $Q_{12}P_1$ | (97) | 9-7 | b |
| 2993.2 | 2993.9 | | | | | |
| 2992.0 | 2992.9 | | | | | |
| 2990.9 | 2991.9 | | | | | |
| 2989.6 | 2990.6 | 2989.5 | $R_{23}R_2$ | (118) | 3-5 | a |
| 2988.9 s | 2989.6 vs | | | | | |
| 2987.6 vs | 2988.5 s | 2987.7 | $Q_{23}P_2$ | (85) | 5-4 | b |
| 2986.6 | 2987.3 | | | | | |
| 2985.3 | | | | | | |
| 2984.0 | | 2984.5 | Q_1R_1 | (52) | 4-3 | b |
| 2983.0 | 2983.8 | 2983.7 | Q_3R_3 | (50) | 4-3 | b |
| 2982.0 | | 2982.7 | $Q_{12}P_1$ | (87) | 3-4 | a |
| | | 2981.8 | Q_2R_2 | (51) | 4-3 | b |
| 2981.0 | | 2980.8 | $Q_{23}P_2$ | (78) | 4-5 | a |
| 2979.7 | 2980.6 | 2979.6 | $Q_{12}P_1$ | (79) | 4-5 | a |
| 2978.7 | 2979.3 | | | | | |
| 2977.6 | 2978.3 | | | | | |
| 2976.4 | 2977.2 | 2977.0 | $Q_{23}P_2$ | (96) | 9-7 | b |
| | | 2975.0 | S_2R_2 | (125) | 4-4 | b |

Table 4.2 (continued)

| $C_6H_6^a$ $(\omega_1 - \omega_2) \text{ cm}^{-1}$ | $C_2H_2^b$ $(\omega_1 - \omega_2) \text{ cm}^{-1}$ | Calc. $(\omega_1 - \omega_2) \text{ cm}^{-1}$ | Assignment | | | Res. ^c case |
|---|---|--|--|--|------|---------------------------|
| | | | $R_{mn} S_{wn}^d$ | (J) | Band | |
| 2975.1 | 2975.8 | 2974.9 | $Q_1 R_1$ | (76) | 0-1 | a |
| 2974.1 | 2974.7 | 2974.6 | $\begin{Bmatrix} Q_2 R_2 \\ Q_3 R_3 \end{Bmatrix}$ | $\begin{matrix} (75) \\ (74) \end{matrix}$ | 0-1 | a |
| | | 2973.8 | $Q_{23} R_2$ | (68) | 7-6 | b |
| 2973.1 vs | 2973.7 s | 2973.2 | $Q_{12} R_1$ | (69) | 7-6 | b |
| 2971.8 | 2972.5 | 2971.9 | $\begin{Bmatrix} Q_{12} R_1 \\ S_{21} R_2 \end{Bmatrix}$ | $\begin{matrix} (70) \\ (68) \end{matrix}$ | 7-6 | b |
| 2970.8 | | 2971.3 | $S_{32} R_3$ | (67) | 7-6 | b |
| 2969.7 | | | | | | |
| 2968.4 | | | | | | |
| 2967.2 | | | | | | |
| 2966.2 | 2966.8 | 2966.4 | $Q_{23} R_3$ | (167) | 8-7 | a |
| 2965.1 | | | | | | |
| 2964.1 | | | | | | |
| 2962.9 | | | | | | |
| 2961.9 | | | | | | |
| | | 2959.2 | $Q_{23} R_2$ | (45) | 6-7 | a |
| | | 2958.6 | $Q_{12} R_1$ | (46) | 6-7 | a |
| | 2956.8 | 2957.9 | $Q_1 R_1$ | (70) | 1-2 | a |
| | 2955.8 | 2955.8 | $S_{32} R_3$ | (44) | 6-7 | a |
| | | 2955.3 | $\begin{Bmatrix} Q_3 R_3 \\ Q_2 R_2 \end{Bmatrix}$ | $\begin{matrix} (68) \\ (69) \end{matrix}$ | 1-2 | a |
| 2954.8 | 2954.5 | 2954.6 | $Q_3 P_3$ | (77) | 4-3 | b |
| 2953.0 | 2953.4 | | | | | |
| 2951.7 | 2952.3 | | | | | |
| 2950.7 | 2951.2 | 2951.2 | $Q_1 R_1$ | (48) | 5-4 | b |
| 2949.4 | 2950.1 | | | | | |
| 2948.5 | 2949.0 | 2948.7 | $Q_3 R_3$ | (46) | 5-4 | b |
| 2947.2 | 2947.8 | 2948.2 | $S_{21} R_2$ | (45) | 6-7 | a |
| 2946.2 | 2946.5 | 2947.0 | $Q_2 R_2$ | (47) | 5-4 | b |

Table 4.2 (continued)

| $C_6H_6^a$ $(\omega_1 - \omega_2) \text{ cm}^{-1}$ | $C_2H_2^b$ $(\omega_1 - \omega_2) \text{ cm}^{-1}$ | Calc. $(\omega_1 - \omega_2) \text{ cm}^{-1}$ | Assignment | | | Res. ^c case |
|---|---|--|--|--|------|---------------------------|
| | | | $Rmn_n Swn_n^d$ | (J) | Band | |
| 2945.3 | 2945.6 | 2946.0 | S_2R_2 | (141) | 5-6 | b |
| 2944.0 | 2944.6 | | | | | |
| 2942.7 | 2943.3 | 2942.3 | $Q_{12}P_1$ | (88) | 6-5 | b |
| 2941.7 | 2942.4 | | | | | |
| 2940.5 | 2941.1 | 2940.9 | $Q_{23}P_2$ | (87) | 6-5 | b |
| 2939.5 | 2939.9 | | | | | |
| 2938.5 | 2938.8 vs | 2938.6 | Q_1R_1 | (64) | 2-3 | a |
| 2937.2 vs | 2937.9 | 2936.9 | Q_2R_2 | (62) | 2-3 | a |
| 2936.3 | 2936.6 | 2935.8 | S_1R_1 | (153) | 8-5 | b |
| 2935.0 | 2935.6 | | | | | |
| 2934.0 | 2934.3 | | | | | |
| 2933.0 | 2933.3 | 2932.7 | Q_2R_2 | (63) | 2-3 | a |
| 2931.7 | 2932.2 | | | | | |
| 2930.7 | 2931.1 | | | | | |
| 2929.5 | 2930.1 | | | | | |
| 2928.5 | 2929.0 | | | | | |
| 2927.2 | 2927.8 | | | | | |
| 2926.2 | 2926.8 | | | | | |
| 2925.2 | 2925.5 | 2925.7 | $S_{23}R_2$ | (158) | 4-5 | b |
| 2923.9 | | | | | | |
| 2922.9 | 2923.3 | | | | | |
| 2921.8 | 2922.2 | | | | | |
| 2920.6 | 2921.0 | | | | | |
| 2919.3 | | | | | | |
| 2917.4 | 2917.7 | | | | | |
| 2916.1 | 2916.4 | | | | | |
| 2915.1 | 2915.4 | | | | | |
| | | 2909.3 | Q_1P_1 | (96) | 1-0 | b |
| | | 2908.5 | $\{ \begin{matrix} Q_2R_2 \\ Q_3R_3 \end{matrix} \}$ | $\begin{matrix} (45) \\ (44) \end{matrix}$ | 6-5 | b |

Table 4.2 (continued)

| $C_6H_6^a$ $(\omega_1 - \omega_2) \text{ cm}^{-1}$ | $C_2H_2^b$ $(\omega_1 - \omega_2) \text{ cm}^{-1}$ | Calc. $(\omega_1 - \omega_2) \text{ cm}^{-1}$ | Assignment | | | Res. ^c case |
|---|---|--|---|---|------------|---------------------------|
| | | | $R_{m_n} S_{w_n}^d$ | (J) | Band | |
| | | 2907.4 | $Q_1 R_1$ | (47) | 6-5 | b |
| | | 2905.6 | $Q_{23} P_2$ | (165) | 9-7 | a |
| 2903.3 | 2903.6 | | | | | |
| 2902.6 s | 2903.6 vs | | | | | |
| 2901.3 | 2901.7 | | | | | |
| 2900.1 | 2900.4 | | | | | |
| 2899.0 | 2899.4 | | | | | |
| | | 2899.3 | $\left\{ \begin{array}{l} Q_{32} R_3 \\ Q_{21} R_2 \end{array} \right.$ | $\left. \begin{array}{l} (54) \\ (54) \end{array} \right\}$ | 2-1 | b |
| | 2898.3 | | | | | |
| 2896.7 | 2897.1 | | | | | |
| 2895.5 | 2896.1 | 2895.6 | $Q_3 Q_3$ | (146) | 4-7 | a |
| 2894.4 | 2894.8 | | | | | |
| 2893.3 | 2893.7 | 2892.7 | $Q_{31} R_2$ | (48) | 3-2 | b |
| 2892.2 | 2892.5 | 2892.3 | $Q_{32} R_3$ | (47) | 3-2 | b |
| 2891.2 | 2891.5 | | | | | |
| | | 2891.4 | $\left\{ \begin{array}{l} Q R \\ Q P \end{array} \right.$ | $\left. \begin{array}{l} (52) \\ (91) \end{array} \right\}$ | 4-5 2-1 | a b |
| 2890.0 | | 2890.7 | $\left\{ \begin{array}{l} Q P \\ Q P \end{array} \right.$ | $\left. \begin{array}{l} (89) \\ (90) \end{array} \right\}$ | 2-1 | b |
| 2888.9 | | | | | | |
| | | 2887.8 | $Q_3 R_3$ | (51) | 4-5 | a |
| 2887.8 | 2888.1 | 2887.5 | $Q_2 R_2$ | (51) | 4-5 | a |
| 2886.6 | 2886.9 | | | | | |
| 2885.3 | 2885.6 | | | | | |
| 2884.3 | 2884.6 | 2884.3 | $Q_2 R_2$ | (137) | 4-7 | a |
| 2883.3 | 2883.7 | 2883.5 | $Q_{21} R_2$ | (42) | 4-3 | b |
| 2882.1 | 2882.5 | 2882.4 | $Q_{32} R_3$ | (41) | 4-3 | b |
| 2879.7 s | 2880.1 | | | | | |
| 2878.7 | 2879.1 s | 2878.9 | $S_{21} R_2$ | (118) | 2-4 | a |
| 2877.8 | 2877.9 | | | | | |
| 2876.5 | 2876.9 | | | | | |

Table 4.2 (continued)

| $C_6H_6^a$ ($\omega_1 - \omega_2$) cm^{-1} | $C_2H_2^b$ ($\omega_1 - \omega_2$) cm^{-1} | Calc. ($\omega_1 - \omega_2$) cm^{-1} | Assignment | | | Res. ^c case |
|---|---|--|---|---|------|---------------------------|
| | | | $Rmn_n Swn_n^d$ | (J) | Band | |
| 2875.5 | 2875.6 | | | | | |
| 2874.2 | 2874.5 | | | | | |
| 2873.2 | 2873.4 | | | | | |
| 2871.9 | 2872.2 | | | | | |
| 2870.9 | 2871.1 | | | | | |
| | | 2869.2 | $Q_1 P_1$ | (87) | 3-2 | b |
| 2864.0 | 2864.1 | 2863.7 | $Q_2 P_2$ | (78) | 4-3 | b |
| | | 2863.1 | $Q_2 P_2$ | (86) | 3-2 | b |
| | | 2860.7 | $Q_{21} R_2$ | (38) | 5-4 | b |
| | | 2859.1 | $Q_{32} R_3$ | (37) | 5-4 | b |
| 2846.5 | 2846.8 | | | | | |
| 2845.2 | 2845.5 | 2844.4 | $\left\{ \begin{array}{l} Q_3 R_3 \\ Q_1 R_1 \end{array} \right.$ | $\left. \begin{array}{l} (50) \\ (51) \end{array} \right\}$ | 7-6 | b |
| 2844.2 | 2844.4 | 2844.1 | $Q_2 R_2$ | (51) | 7-6 | b |
| 2843.0 | 2843.1 | | | | | |
| 2841.9 | 2842.0 | 2841.7 | $S_{21} R_2$ | (131) | 3-3 | b |
| 2840.6 | 2840.8 | | | | | |
| 2839.5 | 2839.6 | | | | | |
| | | 2837.8 | $Q_3 P_3$ | (72) | 5-4 | b |

$\omega_1 = 18789.3 \text{ cm}^{-1}$; ω = weak; m = medium, s = strong, v = very

^a $\sim 8 \text{ mJ } \omega_{266}$, P = 10 torr

^b $\sim 8 \text{ mJ } \omega_{266}$, P = 60 torr

^c Resonant case refers to Figure (4.7a, b) with case (a) involving ω_1 and ω_2 resonance, case (b) involving ω_1 and ω_3 resonances.

^d n refers to triplet sublevels involved in resonant case (see Figure (4.9) and discussion in text).

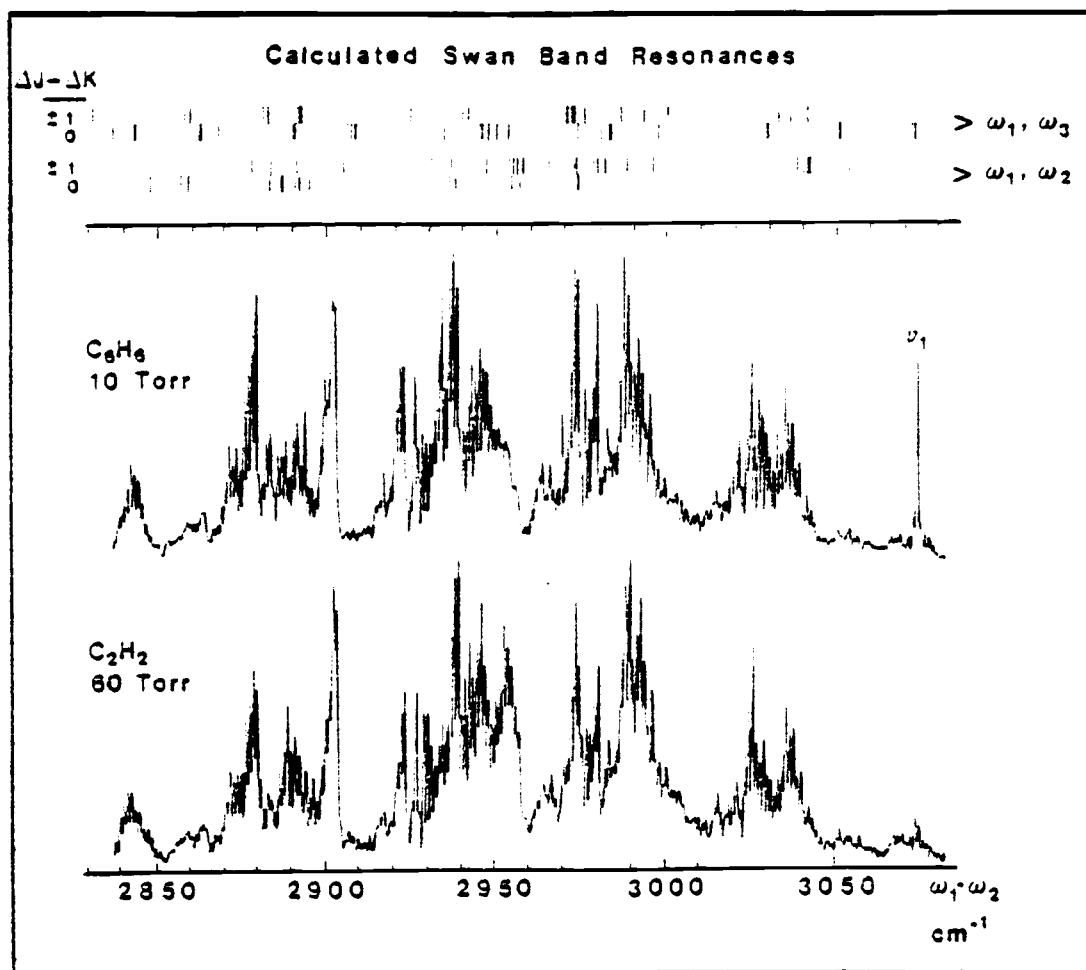


Figure 4.8. High resolution ($\sim 3 \text{ cm}^{-1}$) broadband 3WM spectra produced by 266 nm photolysis of 10 torr C_6H_6 , upper trace, and 60 torr C_2H_2 , lower trace. ω_1 frequency was held fairly constant at 18789.29 cm^{-1} for both scans as was the ω_{266} intensity ($\sim 7 \text{ mJ}$). The positions of possible multiple Swan band resonances, Table (4.2), are indicated.

of the Raman transitions involved. Consequently, the results in Table (4.2) appear in the following form:

$$\text{Ram}_n \text{Sw}_n(J''), v' - v'' .$$

Ram and Sw_n are the Raman and Swan branch transitions designators (depending on J), n = 1, 2 or 3 (corresponding to ³π₀, ³π₁, and ³π₂ respectively) and denotes the particular triplet sublevel (or levels) involved, J'' is the rotational quantum number of the lower state, and v' - v'' are the upper and lower state vibrational quantum numbers describing the band system (emission notation) to which the Swan transition belongs. This notation is perhaps best understood with the aid of Figure (4.9) which shows the two triplet states, including sublevels, and examples of the labeling scheme. The resonant 3WM process shown in the ³π₀ sublevel involves the resonant Swan P branch transition

$$d \text{ } ^3\pi_{g_0} (v'=1, J'=3) - a \text{ } ^3\pi_{u_0} (v''=0, J''=4)$$

in the 1-0 emission band and the resulting Raman Q branch transition (relative to the initial state)

$$a \text{ } ^3\pi_{g_0} (v''=0, J''=4) - a \text{ } ^3\pi_{g_0} (v''=2, J''=4)$$

for the lower (a) state vibrational overtone band with Δv = 2. Using the notation previously developed, this

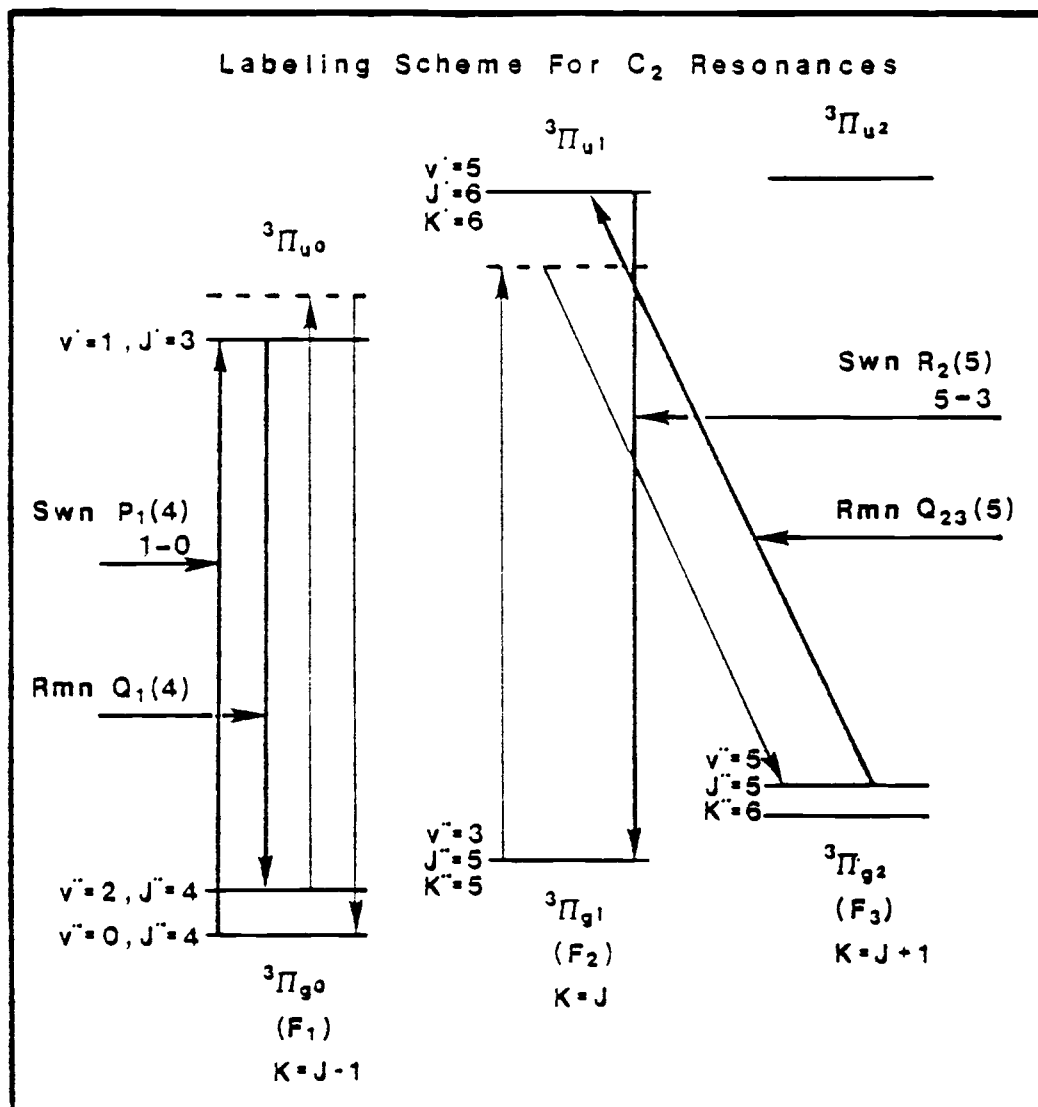


Figure 4.9. Energy level diagram of the a and d triplet states of C_2 including the three sublevels for $K = J - 1, J$ and $J + 1$. Two possible resonance processes are shown to demonstrate the labeling scheme used in Table (4.2).

process would have the designation

$$Q_1 P_1(4), 1-0 .$$

The second process shown in Figure (4.8) depicts transitions between sublevels 2 and 3 ($\Delta K - \Delta J = 1$). Here, the electronic resonance is in ω_3 and contained in the $^3\pi_1$ sublevel with $J' = J'' + 1$. This R branch transition

$$d \ ^3\pi_{g_1} (v'=5, J'=6) - a \ ^3\pi_{u_1} (v''=3, J''=5)$$

would be in the 5-3 emission band. The Raman transition shown

$$a \ ^3\pi_{g_1} (v''=3, J''=5) - a \ ^3\pi_{g_2} (v''=5, J''=5)$$

is between sublevels $n=2$ and $n=3$. The designation for this resonant process would thus be

$$Q_{23} P_2(5), 5-3 .$$

From elementary intensity considerations, it is possible to predict the most likely set of Raman and resonant Swan transitions. The most intense features in the Swan band emission spectra correspond to transitions involving $\Delta J = \pm 1$ and $\Delta J - \Delta K = 0$ (P and R branches within a given sublevel) [66]. From Raman transition selection rules, $\Delta J = 0, \pm 2, O, Q,$ and S branch Raman bands are expected to be observable. Since the assignments depend on

simultaneous electronic and Raman resonance, the most intense 3WM features are expected for P and R branch resonant Swan band transitions coupled with O, Q, and S branch Raman lines. Only these "most likely" sets of transitions are included in Table (4.2).

What at first appears strange, for these assignments, is the large distribution of C_2 fragments among the vibrational and rotational levels. The fluorescence results demonstrated that C_2 is born in many electronic states (not just a $^3\Pi_u$) and these assignments suggest that the fraction of molecules in any given vibronic level is exceedingly small. If these assignments can be believed, then C_2 is being detected at very low (sub torr) pressures. Although the number of possible resonances, in this region, cannot account for all of the observed features, there is no doubt that more complete calculations in the Swan system and similar calculations involving the other electronic states, of C_2 detected, would result in many more resonant assignments. Experiments to reduce the complexity of the observed spectrum would be of great help in interpreting the results. For example, if the photofragments could be rotationally cooled by free jet expansion into a supersonic molecular beam, the resulting 3WM spectrum would be significantly altered due to depletions in the populations of higher rotational levels.

In order to further test the possibility that ω_1 is involved in resonant processes, an experiment was carried out with the OMA which involved changing very slightly the ω_1 frequency. Figure (4.10) shows the ω_1 effects on the 3WM spectra obtained from 266 nm photolyzed C_6H_6 . The change in ω_1 frequency, $\Delta\omega_1 \approx .3 \text{ cm}^{-1}$, was determined by noting the position of the residual ν_{CH} band of C_6H_6 . Both scans were taken with equivalent pressures of C_6H_6 and UV power intensities. Attempts to account for the spectral changes, in terms of resonance intensity considerations using the assignments listed in Table (4.2), were limited by observed and calculated frequency uncertainties of about 0.5 and 2.0 cm^{-1} , respectively, along with the close spacing ($\sim 1 \text{ cm}^{-1}$) of the observed transitions. Further experiments, under higher resolution conditions, may result in a more definite assignment.

An alternate possibility is that the spectrum results from one photon electronic resonances in ω_2 or ω_3 . Such resonances contribute to the 3WM at ω_3 and the intensities could be appreciable in the event of additional resonances in $2\omega_1$ and ω_1 as indicated in Figures (4.6a) and (4.6c). Indeed, from the previous consideration of processes similar to Figure (4.6d), it may be concluded that multiple resonances must be essential from the comparison of the 3WM and the fluorescence spectra of Figure (4.5). This statement is based on the fact that the 3WM spectrum

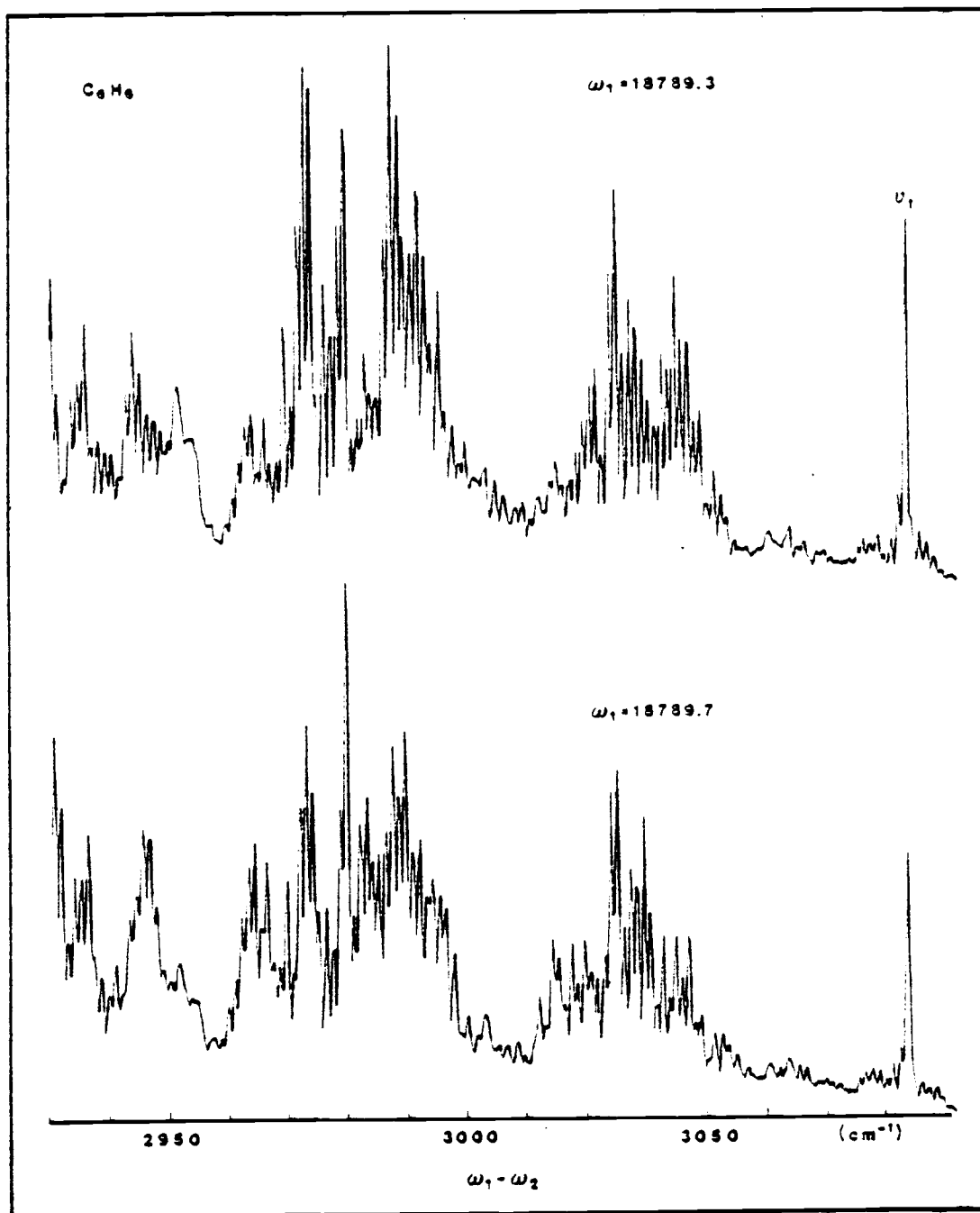


Figure 4.10. Effect of ω_1 frequency on the 3WM spectra produced by 266 nm photolysis of 10 torr benzene. The top trace is part of the spectrum shown in Figure (4.8) with $\omega_1 = 18789.3$ cm^{-1} . The bottom trace was recorded under similar conditions with $\omega_1 = 18789.7$ cm^{-1} .

(corresponding to the 2700-3100 cm^{-1} region of Figure (4.3)) contains no indication of the intense Swan band near 467 nm although a process of the type of Figure (4.6d) should produce such a resonance. Further evidence that a simple one photon resonance is insufficient comes from other studies of colored species such as NO_2 (Chapter 3) where the ω_3 CARS spectrum does not correlate closely with the absorption spectra of NO_2 in the ω_2 or ω_3 regions [37].

It is conceivable that the signals which are detected in these experiments do not correspond to parametric 3WM processes involving zero net change in molecular energy level. Since the fluorescence results establish that excited states of C_2 are produced, it is possible that the presence of the driving field at $\omega_3 = 2\omega_1 - \omega_2$ could stimulate coherent emission at ω_3 in the direction of the ω_1, ω_2 beams (Figure 4.6e). As evidence against this, it is pointed out that no such coherent emission occurs for the Swan band at 467 nm even though strong spontaneous emission is observed at 90° (Figure (4.5)). Also, the weakness of 90° fluorescence in the region of 3WM bands near 460 nm (Figure (4.5)) does not seem to be consistent with a simple stimulated emission process. For these reasons the most favorable explanation is based on vibrational and electronic resonances for C_2 with the probable further requirement of at least one additional electronic resonance

such as indicated in Figure (4.6a-d). That such multiple resonances could occur for C_2 is not unreasonable in view of the plethora of low lying electronic states.

Unfortunately, it is not possible at present to make a more detailed assignment of the spectral features. Alternate methods of production of C_2 (e.g. by laser pyrolysis of graphite or in C_2H_2 flames) could be helpful in this regard since different C_2 product distributions should result. From corresponding changes in the 3WM spectra, it may then be possible to associate specific transitions with given electronic states. These, and some additional experiments on alternate colored species, are planned by J.W.N. to better characterize the C_2 fragment states and the nonlinear processes involved in generating these transient 3WM spectra.

4.I Summary

This work has shown that efficient vacuum UV photolysis of species such as C_2H_2 , C_6H_6 and other benzene derivatives can be achieved by multiphoton absorption of UV laser photons at 266 nm. Fluorescence spectra establish that C_2 is a major primary fragment which is produced in various electronic states. Energetic considerations and ω_{266} power dependence measurements indicate that at least two or three photons are necessary for C_2 production. The case of two photon photolysis is particularly novel since the

dissociative state of C_6H_6 cannot be accessed by one photon method. The time scale and C_6H_6 pressures correspond to collision free conditions and an intense 3WM spectrum is obtained of the transient fragments born during the 8 nsec photolysis period. Single pulse broadband 3WM spectra taken with an optical multichannel analyzer establish that the 3WM spectra are due to primary photoproducts. C_6D_6 and C_2H_2 results strongly indicate that C_2 is also responsible for the 3WM spectra but the observed bands are not those of a simple CARS vibrational spectrum. A preliminary investigation of possible multiple resonances involving some of the Swan band electronic transitions and Raman transitions suggests that these types of 3WM processes could account for many of the observed spectral features. If such is the case, very small numbers of C_2 molecules in any given state are being detected. A more detailed assignment of this unique and extremely intense 3WM spectrum was not possible but the process is thought to involve a combination of vibrational-electronic or electronic-electronic resonances.

REFERENCES

1. R. W. Terhune, *Bull. Am. Phys. Soc.* 8, 359 (1963).
2. P. D. Maker and R. W. Terhune, *Phys. Rev.* 137, A801 (1965).
3. W. G. Rado, *Appl. Phys. Lett.* 11, 123 (1967).
4. P. Regnier and J-P.E. Taran, Laser Raman Gas Diagnostics, edited by M. Lapp and C. M. Penney, Plenum Press, N.Y. (1974).
- 5a. J. W. Nibler, J. R. McDonald and A. B. Harvey, *Opt. Commun.* 18, 371 (1976).
- 5b. J. W. Nibler, W. M. Shaub, J. R. McDonald, and A. B. Harvey, "Coherent Anti-Stokes Raman Spectroscopy," Fundamentals and Applied Laser Physics, Vibrational Spectra and Structure, Vol. 6, Chap. 3, Elsevier, N.Y. (1977).
6. W. M. Tolles, J. W. Nibler, J. R. McDonald, and A. B. Harvey, *J. Appl. Spectrosc.* 31, 253 (1977).
7. H. C. Anderson and B. S. Hudson, "Coherent Anti-Stokes Raman Scattering," Vol. 5 in Molecular Spectroscopy, edited by D. A. Long (Chemical Society, London, England, 1978).
8. J. W. Nibler and G. V. Knighten, "Coherent Anti-Stokes Raman Spectroscopy," Topics in Current Physics, edited by A. Weber, Vol. 11, Chap. 7, Springer-Verlag, Berlin (1979).
9. S. Druet and J-P. Taran, "Coherent Anti-Stokes Raman Spectroscopy," in Chemical and Biochemical Applications of Lasers, Vol. IV, edited by C. B. Moore, Academic Press, N.Y. (1978).
10. A. C. Eckbreth and P. W. Schreiber, "Coherent Anti-Stokes Raman Spectroscopy Applications to Combustion and Gas Phase Diagnostics," Chemical Applications of Nonlinear Spectroscopy, Vol. , Chap. 2, Academic Press, N.Y. (1980).

11. H. Lotem, R. T. Lynch, Jr., and H. Bloembergen, Phys. Rev. A 14, 1748 (1976).
12. J. J. Song, G. L. Eesley, and M. D. Levenson, Appl. Phys. Lett. 29, 567 (1976).
13. N. Bloembergen, Nonlinear Optics, Benjamin Inc., N.Y. (1965).
14. R. W. DeWitt, A. B. Harvey, and W. M. Tolles, "Theoretical Development of Third Order Susceptibility as Related to Coherent Anti-Stokes Raman Spectroscopy," NRL Memor. Rpt. No. 3260 (1976).
15. G. R. Fowles, Introduction to Modern Optics, Holt, Rinehart and Winston, N.Y. (1968).
16. M. Born and E. Wolf, Principles of Optics, Pergamon Press, N.Y. (1959).
17. E. Garmire, F. Pandarese, and C. H. Townes, Phys. Rev. Lett. 11, 160 (1973).
18. P. Huber-Wälchli, D. M. Guthals, and J. W. Nibler, Chem. Phys. Lett. 67, 233 (1979).
19. M. A. Yuratich and D. C. Hanna, Mol. Phys. 33, 671 (1977).
20. R. F. Bagley, A. B. Harvey, and R. L. Byer, Appl. Phys. Lett. 25, 387 (1974).
21. P. Regnier, "Applications of Coherent Anti-Stokes Raman Scattering to Gas Concentration Measurements and to Flow Visualization," Eng. translation by European Space Agency tech. trans. ESA TT-200 (1973).
22. M. A. Yuratich, Molec. Phys. 38, 625 (1979).
23. P. Huber-Wälchli, Private communication (1980).
24. P. Huber-Wälchli, D. M. Guthals, and J. W. Niber, results to be published (1980).
25. D. M. Guthals and J. W. Nibler, Opt. Commun. 29, 322 (1979).
26. Lasermetrics, Inc., Technical Memoranda 751 and 763 (TM-751, TM-763), Teaneck, N.J. (1975).
27. G. Massey and J. Johnson, Private communication (1977).

28. T. W. Hänsch, *Appl. Opt.* 11, 895 (1972).
29. M. Littman and H. Metcalf, *Appl. Opt.*, 17, 2224 (1978).
30. I. Shoshan, N. Danon, and U. Oppenheim, *J. Appl. Phys.* 48, 4495 (1977).
31. I. Shoshan and U. Oppenheim, *Opt. Commun.* 25, 375 (1978).
32. M. Littman, *Opt. Lett.* 3, 138 (1978).
33. G. Klauminzer, U. S. Pat. 4,016,504 (Apr., 1977).
34. L. Nair, *Opt. Commun.* 23, 273 (1977).
35. F. Jenkins and H. White, Fundamentals of Optics, McGraw-Hill, N.Y. (1976).
36. Burleigh Instruments Inc., "Fabry-Perots," Technical Memorandum No. FP-140-475, Fishers, N.Y. (1976).
37. D. M. Guthals, K. P. Gross, and J. W. Nibler, *J. Chem. Phys.* 70, 2393 (1979).
38. I. Chabay, G. Klauminzer, and B. S. Hudson, *Appl. Phys. Lett.* 28, 27 (1976).
39. J. Nestor, T. Spiro, and G. Klauminzer, *Proc. Natl. Acad. Sci. U.S.A.* 73, 3329 (1976).
40. L. A. Carrieria, L. P. Goss, and Thomas B. Malloy, Jr., *J. Chem. Phys.* 66, 2762, 4360 (1977).
41. A. Lau, W. Werncke, J. Kelin and M. Pfeiffer, *Opt. Commun.* 21, 399 (1977).
42. B. Attal, O. Schnepp, and J. P. Taran, *Opt. Commun.* 24, 77 (1978).
43. J-P. E. Taran, Laser Spectroscopy, edited by J. L. Hall and J. L. Carlson, Springer, Berlin (1977), Vol. 7.
44. H. D. Bist and J. C. D. Brand, *J. Mol. Spectrosc.* 62, 60 (1976).
45. D. K. Hsu, D. L. Monts, and R. N. Zare, "Spectral Atlas of NO₂, 5530 to 6480 Å, Academic, New York (1978).
46. W. J. Lafferty and R. L. Sams, *J. Mol. Spectrosc.* 66, 478 (1977).

47. V. M. Donnelly and F. Kaufman, *J. Chem. Phys.* 67, 4768 (1977).
48. W. B. Roh, "CARS of Molecular Gases," Technical Report AFAPL-TR-77-47, Wright-Patterson Air Force Base.
49. K. Abe, *J. Mol. Spectrosc.* 48, 395 (1973).
50. H. D. Bist, J. C. D. Brand, and R. Vasudev, *J. Mol. Spectrosc.* 66, 399 (1977).
51. G. Herzberg, Molecular Spectra and Molecular Structure, Van Nostrand, Princeton (1966), Vol. III.
52. K. Abe, F. Myers, T. K. McCubbin, Jr., and S. R. Polo, *J. Mol. Spectrosc.* 50, 413 (1974).
53. R. E. Smalley, L. Wharton, and D. H. Levy, *J. Chem. Phys.* 63, 4977 (1975).
54. G. Herzberg, Molecular Spectra and Molecular Structure, Van Nostrand, Princeton (1945), Vol. II.
55. I. Chabay, G. Klauminzer, and G. S. Hudson, in The Raman Effect, Vol. 2, edited by A. Anderson, Marcel Dekker, Inc., New York (1973).
56. K. P. Gross, D. M. Guthals, and J. W. Nibler, *J. Chem. Phys.* 7, 4673 (1971).
57. J. G. Calvert and J. N. Pitts, Jr., Photochemistry, Wiley, New York (1967), pp. 515-518.
58. G. Porter and B. Ward, *Proc. R. Soc. A.* 287, 457 (1965).
59. J. B. Birks, Photophysics of Aromatic Compounds, Wiley, New York (1970).
60. J. R. McDonald, A. P. Baronwski, and V. M. Donnelly, *Chem. Phys.* 33, 161 (1978).
61. S. M. Bunch, G. R. Cook, M. Ogawa, and A. W. Ehler, *J. Chem. Phys.* 28, 740 (1958).
62. J. F. Ready, Effects of High Power Laser Radiation, Academic, New York (1971).
63. C. Grey Morgan, *Sci. Prog. Oxf.* 65, 31 (1978).

64. J. W. Nibler, Private communication (1980).
65. S. N. Suchard and J. E. Melzer, *Spectrosc. Data* 2, 103 (1976).
66. J. G. Phillips and S. P. Davis, "The Swan System of the C₂ Molecule," Univ. of Calif. Press, Berkeley (1968).
67. K. P. Huber and G. Herzberg, Molecular Spectra and Structure, Van Nostrand, New York (1979), Vol. IV.

APPENDICES

Appendix A: Fourier Transformations of the Wave Equation.

The Fourier transformations on $\bar{E}(t)$ and $\bar{P}(t)$ can be written

$$\bar{E}(t) = \int_{-\infty}^{+\infty} \bar{E}(\omega) e^{-i\omega t} d\omega \quad \checkmark \quad (\text{A.1})$$

$$\bar{P}(t) = \int_{-\infty}^{+\infty} \bar{P}(\omega) e^{-i\omega t} d\omega \quad \checkmark \quad (\text{A.2})$$

and the inverse transformations

$$\bar{E}(\omega) = \frac{1}{2\pi} \int_{-\infty}^{+\infty} \bar{E}(t) e^{i\omega t} dt \quad (\text{A.3})$$

$$\bar{P}(\omega) = \frac{1}{2\pi} \int_{-\infty}^{+\infty} \bar{P}(t) e^{i\omega t} dt . \quad (\text{A.4})$$

From equation 16

$$\nabla \times \nabla \times \bar{E} = -\frac{1}{c^2} \frac{\partial^2 \bar{E}(t)}{\partial t^2} - \frac{4\pi}{c^2} \frac{\partial^2 \bar{P}(t)}{\partial t^2} \quad \checkmark \quad (\text{A.5})$$

$$\begin{aligned} \nabla \times \nabla \times \int_{-\infty}^{+\infty} \bar{E}(\omega) e^{-i\omega t} d\omega &= -\frac{1}{c^2} \frac{\partial^2}{\partial t^2} \int_{-\infty}^{+\infty} \bar{E}(\omega) e^{-i\omega t} d\omega \\ &- \frac{4\pi}{c^2} \frac{\partial^2}{\partial t^2} \int_{-\infty}^{+\infty} \bar{P}(\omega) e^{-i\omega t} d\omega \quad \checkmark \quad (\text{A.6}) \end{aligned}$$

This may be rewritten as

Appendix A (continued)

$$\int_{-\infty}^{+\infty} d\omega e^{-i\omega t} [\bar{\nabla} \times \bar{\nabla} \times \bar{E}(\omega) - \frac{\omega^2}{c^2} \bar{E}(\omega) - \frac{4\pi\omega^2}{c^2} \bar{P}(\omega)] = 0 \quad (A.7)$$

In order for the above relationship to hold, the quantity in brackets must be zero. Thus,

$$\bar{\nabla} \times \bar{\nabla} \times \bar{E}(\omega) - \frac{\omega^2}{c^2} \bar{E}(\omega) = \frac{4\pi\omega^2}{c^2} \bar{P}(\omega) \quad (A.8)$$

Appendix B: Linear Electronic Susceptibility

From [10]:

$$\bar{P}_{(\omega)}^L = \chi_{(\omega)}^L \bar{E}_{(\omega)} \quad (B-1)$$

Assume a damped harmonic oscillator approximation for $\bar{P}_{(\omega)}$ induced by the applied field $\bar{E}_{(\omega)}$.

$$\frac{\partial^2 \bar{q}_{(\omega, t)}}{\partial t^2} + \Gamma \frac{\partial \bar{q}_{(\omega, t)}}{\partial t} + \omega_0^2 \bar{q}_{(\omega, t)} = \frac{-e\bar{E}_{(\omega, t)}}{m} \quad (B-2)$$

\bar{q} is the dipole displacement vector, Γ is the damping constant due to friction, ω_0 is the natural frequency of the oscillating dipole due to its spring constant, m is the dipole mass, and $-e\bar{E}_{(\omega)}$ is the force of the applied field which induces the dipole to oscillate.

The electric field can be expressed in complex notation as

$$\bar{E}_{(\omega, t)} = \frac{E^0}{2} e^{i(k \cdot r - \omega t)} + \frac{E^{0*}}{2} e^{-i(k \cdot r - \omega t)} \quad (B-3)$$

where k is the wave propagation vector in r direction, ω is the frequency of the field, and $*$ denotes complex conjugate (c.c.).

Assume \bar{q} may be written in the same form as \bar{E}

Appendix B (continued)

$$\bar{q}_{(\omega, t)} = \frac{q^0}{2} e^{i(k \cdot r - \omega t)} + \frac{q^{0*}}{2} e^{-i(k \cdot r - \omega t)} \quad (\text{B-4})$$

or

$$\bar{q}_{(\omega, t)} = \frac{q^0}{2} = \frac{q^0}{2} e^{i(k \cdot r - \omega t)} + \text{c.c.}$$

The first and second time derivatives of \bar{q} are:

$$\frac{\partial \bar{q}_{(\omega, t)}}{\partial t} = \frac{-i\omega q^0}{2} e^{i(k \cdot r - \omega t)} + \frac{i\omega q^{0*}}{2} e^{-i(k \cdot r - \omega t)}$$

$$\frac{\partial^2 \bar{q}_{(\omega, t)}}{\partial t^2} = \frac{-\omega^2}{2} q^0 e^{i(k \cdot r - \omega t)} - \frac{\omega^2}{2} q^{0*} e^{-i(k \cdot r - \omega t)}$$

Substitution into (B-2) yields

$$\begin{aligned} (\omega_0^2 - \omega^2 - i\Gamma\omega) \frac{q^0}{2} e^{i(k \cdot r - \omega t)} + \text{c.c.} \\ = \frac{-e}{m} \left[\frac{E^0}{2} e^{i(k \cdot r - \omega t)} + \text{c.c.} \right] \end{aligned} \quad (\text{B-5})$$

and

$$\frac{q^0}{2} = \frac{-eE^0}{2m(\omega_0^2 - \omega^2 - i\Gamma\omega)} \quad ; \quad \frac{q^{0*}}{2} = \frac{-eE^0}{2m(\omega_0^2 - \omega^2 + i\Gamma\omega)} \quad (\text{B-6})$$

If $\chi_{(\omega)}^L$ is assumed to have a complex form, (B-1) becomes

$$P_{(\omega)}^L = -NE \left[\frac{q^0}{2} + \frac{q^{0*}}{2} \right] = \chi_{(\omega)}^L E_{(\omega)} + \chi_{(\omega)}^{L*} E_{(\omega)}^* \quad (\text{B-7})$$

and the linear electric susceptibility is

Appendix B (continued)

$$\chi_{(\omega)}^L = \frac{Ne^2}{m} \left(\frac{1}{\omega_0^2 - \omega^2 - i\Gamma\omega} \right) . \quad (B-8)$$

$\chi_{(\omega)}^L$ can be separated into its real and imaginary parts.

$$\chi_{(\omega)}^L = \frac{Ne^2}{m} \left(\frac{\omega_0^2 - \omega^2}{(\omega_0^2 - \omega^2)^2 + \Gamma^2 \omega^2} + \frac{i\Gamma\omega}{(\omega_0^2 - \omega^2) + \Gamma^2 \omega^2} \right) \quad (B-9)$$

If a complex form for the index of refraction is introduced into (24)

$$N = n + i\alpha = (1 + 4\pi\chi_{(\omega)}^L) \quad (B-10)$$

where n is now the real part of N and α corresponds to the absorption coefficient due to the decrease in the electric field amplitude as a function of thickness. Equating real and imaginary parts of $\chi_{(\omega)}^L$ to n and α leads to the following forms for the index of refraction and absorption coefficient:

$$n^2 = 1 + \frac{4\pi Ne^2}{m} \left(\frac{\omega_0^2 - \omega^2}{(\omega_0^2 - \omega^2)^2 + \Gamma^2 \omega^2} \right) \quad (B-11)$$

$$\alpha^2 = \frac{4\pi Ne^2}{m} \left(\frac{i\Gamma\omega}{(\omega_0^2 - \omega^2)^2 + \Gamma^2 \omega^2} \right) . \quad (B-12)$$

Graphs of n and α as a function of ω in the vicinity of ω_0 yield a dispersion curve and a Lorentzian lineshape respectively [15].

Appendix C: CARS Intensity Calculations for Homonuclear gaseous Diatomic Molecules

The following Fortran program calculates the real and imaginary parts of the third order susceptibility at ω_3

$$\chi_{\text{CARS}}^{(3)} = \chi'_{\text{NR}} + \sum_{V,J} (\chi' + i\chi'') \quad (\text{C.1})$$

$$\chi' = \frac{c^4 (N_n - N_k)}{h\omega_2^4} \left(\frac{\delta\sigma}{\sigma\Omega} \right)_{nk} \frac{\omega_{nk} - (\omega_1 - \omega_2)}{[\omega_{nk} - (\omega_1 - \omega_2)]^2 + \gamma_{nk}^2} \quad (\text{C.2})$$

$$\chi'' = \frac{c^4 (N_n - N_k)}{h\omega_2^4} \left(\frac{\delta\sigma}{\sigma\Omega} \right)_{nk} \frac{i\gamma_{nk}}{[\omega_{nk} - (\omega_1 - \omega_2)]^2 + \gamma_{nk}^2} \quad (\text{C.3})$$

The observed CARS signal at ω_3 is related to $\chi_{\text{CARS}}^{(3)}$ by

$$P_3 \propto |\chi_{\text{CARS}}^{(3)}|^2 \quad (\text{C.4})$$

The resonance frequencies, ω_{nk} , are calculated by

$$\omega_{nk} = T_k - T_n \quad (\text{C.5})$$

where the total energy, T , is given by [67]

$$T = G_{(v)} + F_{v(J)} \quad (\text{C.6})$$

$G_{(v)}$ is the vibrational term, $F_{v(J)}$ is the rotational term and

$$G_{(v)} = \omega_e (v + \frac{1}{2}) - \omega_e x_e (v + \frac{1}{2})^2 + \omega_e y_e (v + \frac{1}{2})^3 + \omega_e z_e (v + \frac{1}{2})^4 + \dots \quad (\text{C.7})$$

Appendix C (continued)

$$F_{\nu(J)} = B_{\nu}J(J+1) - D_{\nu}J^2(J+1)^2 + H_{\nu}J^3(J+1)^3 + \dots \quad (\text{C.8})$$

$$B_{\nu} = B_e - \alpha_e(v+\frac{1}{2}) + \gamma_e(v+\frac{1}{2})^2 + \dots \quad (\text{C.9})$$

$$D_{\nu} = D_e + \beta_e(v+\frac{1}{2}) + \dots \quad (\text{C.10})$$

$$H_{\nu} = H_e \quad (\text{C.11})$$

The molecular constants are taken directly from Herzberg [67].

The number density for a vibration-rotation state is calculated by

$$N_{\nu,J} = \frac{g_N(2J+1)}{Z} e^{-G(\nu)hc/kT_V} e^{-F(\nu)hc/kT_R} \quad (\text{C.12})$$

where T_V and T_R are the vibrational and rotational temperatures (Kelvin) respectively, g_N is the nuclear degeneracy factor and Z is the partition function.

$$Z = \sum_{\nu=0}^1 \sum_{J=0}^{\text{even}} g_{N_e}(2J+1) e^{-G(\nu)hc/kT_V} e^{-F_{\nu}(J)hc/kT_R} + \sum_{\nu=0}^1 \sum_{J=1}^{\text{odd}} g_{N_o}(2J+1) e^{-G(\nu)hc/kT_V} e^{-F_{\nu}(J)hc/kT_R} \quad (\text{C.13})$$

Appendix C (continued)

The first double sum term is over even J states while the second is over the odd J states. This is necessary to protect the coupling symmetry between the nuclear and rotational wavefunctions.

The Raman cross sections $(\frac{\partial \sigma}{\partial \Omega})_{nk}$, are calculated from the Houll-London factors given by Herzberg [54] for O, Q and S branch Raman transitions.

$$\Delta J = +2: S_J = \frac{3(J+1)(J+2)}{2(2J+3)(2J+1)} \quad \text{S-Branch} \quad (\text{C.14})$$

$$\Delta J=0: S_J = a_0 + \frac{J(J+1)}{(2J-1)(2J+3)} \quad \text{Q-Branch} \quad (\text{C.15})$$

$$\Delta J = -2: S_J = \frac{3(J-1)J}{2(J-1)(2J+1)} \quad \text{O-Branch} \quad (\text{C.16})$$

a_0 is a constant due to trace isotropic scattering and gives the intensity of the Q branch relative to the O and S branches.

The natural Raman linewidth, γ_{nk} (HWHM), is obtained from experimental Raman results [22] and is entered into the program as Γ_{nk} (FWHM). The following pages contain a Fortran listing of the CARS intensity program. Following the listing is a sample run for O_2 . The results of these calculations are shown in Figures (1.5) and (1.7).

Appendix C (continued)

```

C
C
C IN THIS PROGRAM THE CARS SIGNAL FOR A DIATOMIC
C MOLECULE IS CALCULATED.
C
C
      COMMON/DEC/SCALE
      COMMON/YVAL/IXOLD,IYOLD,JCROSS,IPL0T,IVAR
      COMMON/TIC/XMIN,XMAX,XDIM,ADV
      DIMENSION F(35),K(35),WS(35),W0(35),WQ(35),
      2X(35),OLS(35),SLS(35),CLS(35),F1(35),
      3CARSI(2,2410),CON(500)
      IMPLICIT REAL=4(A-H,K,L,N-Z),INTEGER=2(I,J,M)
      TYPE 150
150 FORMAT(' FOR WHICH MOLECULE DO YOU WANT TO CALCULATE A CARS'
      1,/, ' SPECTRUM? (N2, O2, H2, OR D2):(A)',2X$)
      ACCEPT 19,NAME
      DATA CO,UNCON/'C','U'/
      DATA N2,O2,H2,D2,NO,YES,LOR,GAUS/'N2','O2','H2','D2',
      1,'N','Y','L','G'/
      IF(NAME.EQ.N2)GO TO 151
      IF(NAME.EQ.O2)GO TO 152
      IF(NAME.EQ.H2)GO TO 153
      IF(NAME.EQ.D2)GO TO 154
C
C DATA FOR N2 (HERZBERG/HUBER)
C
151 WE=2358.57
      WEXE=14.324
      WEYE=-.30226
      WEZE=-.00024
      BE=1.99324
      ALFA=.017318
      GAMAE=-.20003
      IGE=6
      IGO=3
      IJ=30
      IVMAX=10
      GO TO 155
C
C DATA FOR O2 (HERZBERG/HUBER)
C
152 WE=1580.193
      WEXE=11.981
      WEYE=0.04747
      WEZE=-0.001273
      BE=1.44563
      ALFA=0.0159
      GAMAE=0.
      IGO=1
      IGE=0
      IJ=30
      IVMAX=10
      GO TO 155
C

```

Appendix C (continued)

```

C DATA FOR H2 (HERZBERG/HUBER)
C
153 WE=4401.213
WEXE=121.336
WEYE=0.8129
WEZE=0.
BE=60.853
ALFA=3.0622
GAMAE=0.
IGE=1
IGO=3
IJ=21
IUMAX=3
GO TO 155

C
C DATA FOR D2 (HERZBERG/HUBER)
C
154 WE=3115.5
WEXE=61.82
WEYE=0.562
WEZE=-0.02286
BE=30.4436
ALFA=1.0786
GAMAE=0.
IGO=3
IGE=6
IJ=30
IUMAX=10
155 JMAX=IJ
C
A=7.5
TYPE 92
92 FORMAT(' ENTER A FOR TRACE SCATTERING:(F)',2X$)
ACCEPT 10,A
W1=18790.

C
C CALCULATION OF BV0 AND BV1 (ROTATIONAL CONSTANTS) FOR THE
C GROUND AND FIRST EXCITED VIBRATIONAL STATES.
C
BV0=BE-ALFA/2.+GAMAE/4.
BV1=BE-3.*ALFA/2.+9.*GAMAE/4.

C
C CALCULATION OF THE ROTATIONAL CONSTANT DV REPRESENTING THE
C INFLUENCE OF CENTRIFUGAL FORCE FOR THE GROUND AND FIRST EXCITED
C VIBRATIONAL STATES.
C
DE=4.*(BE**3)/(WE**2)
BETA=DE*(3.*WEXE/WE-5.*ALFA/BE-WE*(ALFA**2)/(24.*(BE**3)))
DV0=DE*(BETA/2.)
DV1=DE*(3.*BETA/2.)

C
C CALCULATION OF THE FUNDAMENTAL VIBRATIONAL FREQUENCY.
C
W0=WE-(2.*WEXE)+(13.*WEYE)/4.+5.*WEZE
TYPE 101,W0,NAME
101 FORMAT (' W0=',F12.5,' WAVENUMBERS FOR ',A2,/)

C
C INPUT PARAMETERS FOR PARTITION FUNCTION CALCULATION AND Q, Q, AND

```

Appendix C (continued)

```

C S-BRANCH TRANSITION CALCULATIONS.
C
  TYPE 15
15 FORMAT (' ENTER ROT. TEMP. IN DEGREES KELVIN:(F)',2X$)
  ACCEPT 10,TEMPR
  TYPE 16
16 FORMAT(' ENTER VIB. TEMP. IN DEGREES KELVIN:(F)',2X$)
  ACCEPT 10,TEMPV
  TYPE 88
88 FORMAT(' I AM NOW CALCULATING THE CRAZY PARTITION FUNCTION',/)
  6 FORMAT (F10.3)
10 FORMAT (F15.5)
17 FORMAT (A1)
18 FORMAT (I3)
19 FORMAT (A8)
21 FORMAT (F5.4)
31 FORMAT (2F10.5)
  CONSTR=1.43879/TEMPR
  CONSTV=1.43879/TEMPV
C
C CALCULATION OF THE PARTITION FUNCTION.
C
  ZE=0.
  ZO=0.
  DO 1 IV=0,IVMAX
  V=IV+.5
  GV=WE*V-WE*E*V*V+WEYE*(V*V*V)+WEZE*(V*V*V*V)-WE/2.
  PV=DEXP(-GV*CONSTR)
  BV=BE-ALFA*V+GAMAE*V*V
  DV=DE+BETA*V
  DO 1 J=0,IJ,2
  I=J
  FV=BV*I*(I+1.)-DV*((I*(I+1.))**2)
  PF=(2*I+1.)*DEXP(-FV*CONSTR)
  ZE=ZE+PV*PF
  I=J+1
  FV=BV*I*(I+1.)-DV*((I*(I+1.))**2)
  PF=(2*I+1.)*DEXP(-FV*CONSTR)
  ZO=ZO+PV*PF
  1 CONTINUE
  Z=IGE*ZE+IGO*ZO
  TYPE 104,Z
104 FORMAT (' PARTITION FUNCTION = ',G13.6,/)
C
C CALCULATION OF J(J+1) AND F(J).
C
  JMN=JMAX+2
  DO 64 J=0,JMN
  I=J+1
  K(I)=J*(J+1)
  F(I)=BV0*K(I)-DV0*(K(I)**2)
  F1(I)=BV1*K(I)-DV1*(K(I)**2)
C
C SELECTION OF APPROPRIATE NUCLEAR DEGENERACY FACTOR.
C
  M=(-1)**J
  IF (M.LT.0) GO TO 200

```

Appendix C (continued)

```

      GN=1.*IGE/(IGE+IGO)
      Z=ZE
      GO TO 210
200 GN=1.*IGO/(IGE+IGO)
      Z=ZO
210 X(I)=GN*(2.*J+1)/Z
      64 CONTINUE
C
C CALCULATION OF THE FREQUENCIES OF THE O, Q, AND S-BRANCH
C TRANSITIONS ALONG WITH THEIR ASSOCIATED NORMAL RAMAN CROSS
C SECTIONS (LINE STRENGTHS) AND NUMBER DENSITY DIFFERENCES.
C
C
C O-BRANCH DELTA J ==-2
C
      W0(I)=0.
      Y0(I)=0.
      DO 108 J=2, JMN
      I=J+1
      W0(I)=W0+F1(I-2)-F(I)
      Y=J.*(J-1)*J
      V=2.*(2*J-1)*(2*J+1)
      NDO=X(I)*DEXP(-F(I)*CONSTR)-X(I-2)*DEXP(-W0*CONSTV
9-F1(I-2)*CONSTR)
      OLS(I)=Y/V*NDO/3.14159
108 CONTINUE
C
C S-BRANCH DELTA J ==+2
C
      DO 118 J=0, JMAX
      I=J+1
      WS(I)=W0+F1(I+2)-F(I)
      Y=J.*(J+1)*(J+2)
      V=2.*(2*J+3)*(2*J+1)
      NDS=X(I)*DEXP(-F(I)*CONSTR)-X(I+2)*DEXP(-W0*CONSTV
6-F1(I+2)*CONSTR)
      SLS(I)=Y/V*NDS/3.14159
118 CONTINUE
C
C Q-BRANCH DELTA J=0
C
      DO 128 J=0, JMAX
      I=J+1
      WQ(I)=W0+F1(I)-F(I)
      Y=J*(J+1.)
      V=(2.*J-1.)*(2.*J+3.)
      NDQ=X(I)*(DEXP(-F(I)*CONSTR)-DEXP(-W0*CONSTV-F1(I)*CONSTR))
      QLS(I)=(A+Y/V)*NDQ/3.14159
128 CONTINUE
      TYPE 129
129 FORMAT(' DO YOU WANT THE O, Q, AND S-BRANCH TRANSITIONS? ', /
2, ' (YES OR NO) ', 2X$)
      ACCEPT 17, ANS
      IF(ANS.EQ.NO) GO TO 131
      TYPE 102
102 FORMAT(' J', 4X, 'W0(J)', 5X, 'WQ(J)', 5X, 'WS(J)')
      DO 132 J=0, JMAX

```

Appendix C (continued)

```

      I=J+1
      TYPE 103,J,W0(I),WQ(I),WS(I)
132 CONTINUE
131 CONTINUE
      TYPE 105
105 FORMAT ( )
103 FORMAT (I3,3F10.3)
C
C INPUT INITIAL AND FINAL FREQUENCIES (WI,WF) AND RESOLUTION
C INCREMENT FOR CARSI CALCULATION.
C
      TYPE 23
23 FORMAT(' ENTER NAT. RAMAN LINE WIDTH (FWHM) IN WAVENUMBERS:(F)'
1,2X$)
      ACCEPT 10,WIDTH
      WIDTH=WIDTH/2.
      TYPE 24
24 FORMAT(' ENTER INITIAL FREQUENCY IN WAVENUMBERS:(F)',2X$)
      ACCEPT 10,WI
      TYPE 25
25 FORMAT(' ENTER FINAL FREQUENCY IN WAVENUMBERS:(F)',2X$)
      ACCEPT 10,WF
      TYPE 26
26 FORMAT(' ENTER RESOLUTION IN WAVENUMBERS:(F)',2X$)
      ACCEPT 10,RES
      TYPE 27
27 FORMAT(' ENTER XNR:(F)',2X$)
      ACCEPT 10,XNR
      TYPE 600
600 FORMAT(' DO YOU WANT THE O- AND S-BRANCH TRANSITIONS INCLUDED',/
1,' ALONG WITH THE Q-BRANCH TRANSITIONS IN THE INTENSITY ',/
2,' CALCULATIONS? (1=O-BRANCH ONLY, -1=S-BRANCH ONLY, '/
3,' 0=BOTH O- AND S-BRANCHES, 2=Q-BRANCH ONLY.) IF YOU ARE',/
4,' NOT SURE ENTER 0 (1)',2X$)
      ACCEPT 18,IANBR
C
C CALCULATION OF THE NUMBER OF DATA POINTS.
C
      MMAX=((WF-WI)/RES)+1
C
C GENERATION OF LINE SHAPE FUNCTIONS
C
      TYPE 50
50 FORMAT(' DO YOU WANT A CONVOLUTION OVER W2? (YES OR NO):(A)',2X$)
      ACCEPT 17,ANCO
      IF(ANCO.EQ.NO) GO TO 55
      ANSS=NO
900 TYPE 59
59 FORMAT(' LINE SHAPE FUNCTION=(F)*GAUS+(1-F)*LOR',/,
1' ENTER F (FOR FRAC. GAUS):(F)',2X$)
      ACCEPT 10,AF
      TYPE 51
51 FORMAT(' ENTER STOKES (DYE LASER) LINE WIDTH (FWHM)',/
1,' IN WAVENUMBERS:(F)',2X$)
      ACCEPT 10,STOKW
60 IWR=STOKW/RES
C

```

Appendix C (continued)

```

C  CALCULATION OF LINE SHAPE
C
      MCON=1.+(4.9-3.4*AF)*STOKW/RES
      AC1=0.78213/IWR
      AC2=2.7726/IWR/IWR
      DO 52 M=1,MCON
      CON(M)=(AC1*DEXP(-AC2*(M-1.)*(M-1.)))=AF
52  CONTINUE
      AC1=0.63662/IWR
      AC2=4./IWR/IWR
      DO 54 M=1,MCON
      CON(M)=(AC1/(1.+(M-1.)*(M-1.)*AC2))*(1.-AF)+CON(M)
54  CONTINUE
      WWI=WI+MCON*RES
      WWF=WF-MCON*RES
      TYPE 57,WWI,WWF
57  FORMAT(' THE CONVOLUTION RANGES FROM ',F3.2,' TO ',F3.2,' /
1.' WAVENUMBERS.'/)
55  CONTINUE
      IF(ANSS.EQ.YES)GO TO 901
C
C  SET SIGMAX=0 FOR UNCONVOLUTED INTENSITY MAXIMUM TEST.
C
      SIGMAX=0.
C
C  CALCULATION OF XREAL,XIMAG, AND UNCONVOLUTED CARS INTENSITY
C (CARSI).
C
      TYPE 56
56  FORMAT('/', ' TABLE OF UNCONVOLUTED CARS INTENSITY MAXIMA:',/)
      WISQR=WIDTH*WIDTH
      DO 500 M=1,MMAX
      Y=M-1
      DW=WI+Y*RES
C
C  CALCULATION OF W3 FREQUENCY FACTOR.
C
      W2=W1-DW
      W3=W1+DW
      W3FAC=W3*W3/(W2*W2+W2*W2+W2*W2+W2*W2)*1.E26
C
C  CALCULATION OF THE O-BRANCH FREQUENCY DEPENDENT PARTS OF XREAL
C AND XIMAG.
C
      OJR=0.
      OJI=0.
      IF(IANBR.LT.0.OR.IANBR.GT.1)GO TO 980
      DO 230 J=2,JMN
      I=J+1
      DELO=WO(I)-DW
      DELO2=DELO*DELO+WISQR
      OJR=OJR+OLS(I)*DELO/DELO2
230 OJI=OJI+OLS(I)*WIDTH/DELO2
C
C  CALCULATION OF THE S-BRANCH FREQUENCY PARTS OF XREAL
C AND XIMAG.
C

```

Appendix C (continued)

```

980 SJR=0.
    SJI=0.
    IF(IANBR.GE.1)GO TO 990
    DO 220 J=0,JMAX
    I=J+1
    DELS=WS(1)-DW
    DELS2=DELS*DELS+WISGR
    SJR=SJR+SLS(1)*DELS/DELS2
220 SJI=SJI+SLS(1)*WIDTH/DELS2
C
C CALCULATION OF THE Q-BRANCH FREQUENCY DEPENDENT PARTS OF XREAL
C AND XIMAG.
C
990 QJR=0.
    QJI=0.
    DO 240 J=0,JMAX
    I=J+1
    DELQ=WQ(1)-DW
    DELQ2=DELQ*DELQ+WISGR
    QJR=QJR+QLS(1)*DELQ/DELQ2
240 QJI=QJI+QLS(1)*WIDTH/DELQ2
C
C CALCULATION OF XREAL-RESONANT.
C
    XRR=(SJR+QJR+QJR)
C
C CALCULATION OF THE TOTAL XREAL.
C
    XREAL=XRR+XNR
C
C CALCULATION OF XIMAG.
C
    XIRES=(SJI+QJI+QJI)
C
C CALCULATION OF INTENSITY.
C
    CARSI(1,M)=(XREAL**2+XIRES**2)*W3FAC
C
C TEST FOR MAXIMUM INTENSITY.
C
    IF (M.LE.2) GO TO 500
    IF(CARSI(1,M-1).GE.CARSI(1,M-2).AND.CARSI(1,M-1).GE.CARSI
4(1,M)) GO TO 400
    GO TO 500
400 FREQ=DW-RES
    SIGMAX=CARSI(1,M-1)
    TYPE 700,SIGMAX,FREQ
700 FORMAT(' MAXIMUM INTENSITY=',G12.5,' AT ',F10.3,' WAVENUMBERS. ')
500 CONTINUE
    IF (ANCO.EQ.NO) GO TO 72
C
C CALCULATION OF THE CONVOLUTED CARSI INTENSITIES.
C
901 TYPE 58
58 FORMAT('/', ' TABLE OF CONVOLUTED CARSI INTENSITY MAXIMA: ',/)
    SIGMAX=0.
    MMCON=MMAX-MCON

```


Appendix C (continued)

```

DO 506 M=MCON,MMCON
CARSI(2,M)=CON(1)*CARSI(1,M)
DO 505 MC=2,MCON
CARSI(2,M)=CARSI(2,M)+CON(MC)*(CARSI(1,M-MC+1)
I+CARSI(1,M+MC-1))
505 CONTINUE
C
C TEST FOR MAXIMUM CONVOLUTED CARS INTENSITY
C
IF(M.LE.MCON+2) GO TO 506
IF(CARSI(2,M-1).GE.CARSI(2,M-2).AND.CARSI(2,M-1).GE.CARSI
I(2,M)) GO TO 507
GO TO 506
507 FREQ=WI+M*RES
SIGMAX=CARSI(2,M-1)
TYPE 700,SIGMAX,FREQ
506 CONTINUE
TYPE 40
40 FORMAT(//,' DO YOU WANT A PLOT? (YES OR NO) (A)',2X$)
ACCEPT 17,ANSI
IF(ANSI.EQ.NO) GO TO 68
C
C PREPARATION FOR PLOTTING
C
72 ML=1
MU=MMAX
MNP=1
IF (ANCO.EQ.NO) GO TO 38
TYPE 39
39 FORMAT(' WHICH ONE? (UNCONVOLUTED OR CONVOLUTED) (A)',2X$)
ACCEPT 17,ANSMNP
IF (ANSMNP.EQ.UNCON) GO TO 38
MNP=2
ML=MCON
MU=MMAX-MCON
38 CONTINUE
TYPE 41
41 FORMAT(' ENTER MAXIMUM INTENSITY:(F)',2X$)
ACCEPT 10,YMAX
TYPE 49
49 FORMAT(' ENTER MINIMUM INTENSITY:(F)',2X$)
ACCEPT 10,YMIN
TYPE 42
42 FORMAT(' ENTER NUMBER OF Y-AXIS TIC MARKS:(F)',2X$)
ACCEPT 10,YNTIC
TYPE 43
43 FORMAT(' ENTER NUMBER OF WAVENUMBERS BETWEEN X-AXIS',/
1,' TIC MARKS:(F)',2X$)
ACCEPT 10,XTIC
YTIC=YMAX/YNTIC
XMIN=WI
XMAX=WF
TYPE 44
44 FORMAT(' ENTER 0 FOR TEK PLOT OR 1 FOR XY PLOT:(I)',2X$)
ACCEPT 18,IPL0T
IF(IPL0T.EQ.0) GO TO 46
DO 46 I=1,2

```

Appendix C (continued)

```

CALL PLOT(0,511,511)
PAUSE ' SET ZERO ON XY'
CALL PLOT(0,1023,1023)
PAUSE ' SET MAXIMUM GAIN (FULL SCALE) ON XY'
CALL PLOT(0,0,0)
PAUSE ' SET GAIN FOR MINIMUM X AND Y '
46 CONTINUE
ADV=XTIC
DELY=YMAX-YMIN
DELX=XMAX-XMIN
SCALE=DELY/YTIC
CALL LTROUT(27,12)      IERASE TEC
CALL LTROUT(27,12)      IERASE TEC
CALL PLOT(0,0,1023)
TYPE 47
47 FORMAT(' DO YOU WANT AXES DRAWN? (YES OR NO):(A)',2X$)
ACCEPT 17,ANS2
IF(ANS2.EQ.NO) GO TO 48
CALL AXIS
48 YDIM=1024./DELY
IF (I PLOT.EQ.0) YDIM=780./DELY
XDIM=1024./MMAX
MODE=0
IYMAX=YDIM*DELY
DO 501 M=ML,MU
XM=M-1
IX=XM*XDIM
IY=(CARS(MNP,M)-YMIN)*YDIM
IF(IY.GT.IYMAX) IY=IYMAX
IF(IY.LT.0) IY=0
CALL XY PLOT(MODE,IX,IY)
MODE=MODE+1
501 CONTINUE
CALL XY PLOT(0,IX,IY)
CALL PLOT(0,IX,IY)
TYPE 71
71 FORMAT(' DO YOU WANT ANOTHER PLOT? (YES OR NO):(A)',2X$)
ACCEPT 17,ANS3
IF(ANS3.EQ.YES) GO TO 72
68 TYPE 69
69 FORMAT(' DO YOU WANT ANOTHER CONVOLUTION? (YES OR NO):(A)',2X$)
ACCEPT 17,ANS5
IF(ANS5.EQ.YES) GO TO 900
502 CONTINUE
STOP
END

```

Appendix C (continued)

RUN DX1:CAR52

FOR WHICH MOLECULE DO YOU WANT TO CALCULATE A CARS
SPECTRUM? (N2, O2, H2, OR D2):(A) O2

ENTER A FOR TRACE SCATTERING:(F) 7.

W0= 1556.37891 WAVENUMBERS FOR O2

ENTER ROT. TEMP. IN DEGREES KELVIN:(F) 300.

ENTER VIS. TEMP. IN DEGREES KELVIN:(F) 300.

I AM NOW CALCULATING THE CRAZY PARTITION FUNCTION

PARTITION FUNCTION = 73.7961

DO YOU WANT THE O, Q, AND S-BRANCH TRANSITIONS?
(YES OR NO) YES

| J | W0(J) | WQ(J) | WS(J) |
|----|----------|----------|----------|
| 0 | 0.000 | 1556.379 | 1564.909 |
| 1 | 0.000 | 1556.347 | 1570.564 |
| 2 | 1547.753 | 1556.284 | 1576.187 |
| 3 | 1541.971 | 1556.188 | 1581.776 |
| 4 | 1536.158 | 1556.061 | 1587.333 |
| 5 | 1530.313 | 1555.902 | 1592.857 |
| 6 | 1524.439 | 1555.711 | 1598.348 |
| 7 | 1518.533 | 1555.489 | 1603.805 |
| 8 | 1512.597 | 1555.234 | 1609.228 |
| 9 | 1506.631 | 1554.948 | 1614.617 |
| 10 | 1500.636 | 1554.630 | 1619.973 |
| 11 | 1494.610 | 1554.280 | 1625.293 |
| 12 | 1488.556 | 1553.899 | 1630.579 |
| 13 | 1482.472 | 1553.485 | 1635.830 |
| 14 | 1476.359 | 1553.040 | 1641.046 |
| 15 | 1470.218 | 1552.563 | 1646.226 |
| 16 | 1464.048 | 1552.054 | 1651.371 |
| 17 | 1457.850 | 1551.513 | 1656.479 |
| 18 | 1451.625 | 1550.941 | 1661.552 |
| 19 | 1445.371 | 1550.337 | 1666.589 |
| 20 | 1439.090 | 1549.701 | 1671.589 |
| 21 | 1432.781 | 1549.033 | 1676.552 |
| 22 | 1426.446 | 1548.333 | 1681.478 |
| 23 | 1420.083 | 1547.602 | 1686.366 |
| 24 | 1413.695 | 1546.839 | 1691.217 |
| 25 | 1407.280 | 1546.044 | 1696.031 |
| 26 | 1400.838 | 1545.217 | 1700.807 |
| 27 | 1394.371 | 1544.358 | 1705.544 |
| 28 | 1387.878 | 1543.468 | 1710.243 |
| 29 | 1381.360 | 1542.545 | 1714.903 |
| 30 | 1374.816 | 1541.591 | 1719.524 |

ENTER NAT. RAMAN LINE WIDTH (FWHM) IN WAVENUMBERS:(F) .03

ENTER INITIAL FREQUENCY IN WAVENUMBERS:(F) 1547.

ENTER FINAL FREQUENCY IN WAVENUMBERS:(F) 1559.

Appendix C (continued)

ENTER RESOLUTION IN WAVENUMBERS:(F) .005

ENTER XNR:(F) 0.

DO YOU WANT THE Q- AND S-BRANCH TRANSITIONS INCLUDED
ALONG WITH THE Q-BRANCH TRANSITIONS IN THE INTENSITY
CALCULATIONS? (1=Q-BRANCH ONLY, -1=S-BRANCH ONLY,
0=BOTH Q- AND S-BRANCHES, 2=Q-BRANCH ONLY.) IF YOU ARE
NOT SURE ENTER 0 (1) 2

DO YOU WANT A CONVOLUTION OVER W2? (YES OR NO):(A) YES

LINE SHAPE FUNCTION=(F)*GAUS+(1-F)*LOR
ENTER F (FOR FRAC. GAUS):(F) .3

ENTER STOKES (DYE LASER) LINE WIDTH (FWHM)
IN WAVENUMBERS:(F) .17

THE CONVOLUTION RANGES FROM 1547.38 TO 1558.63
WAVENUMBERS.

TABLE OF UNCONVOLUTED CARS INTENSITY MAXIMA:

| | | | |
|--------------------|--------|----|-----------------------|
| MAXIMUM INTENSITY= | 26.862 | AT | 1547.600 WAVENUMBERS. |
| MAXIMUM INTENSITY= | 75.120 | AT | 1549.030 WAVENUMBERS. |
| MAXIMUM INTENSITY= | 189.62 | AT | 1550.335 WAVENUMBERS. |
| MAXIMUM INTENSITY= | 410.59 | AT | 1551.510 WAVENUMBERS. |
| MAXIMUM INTENSITY= | 802.69 | AT | 1552.560 WAVENUMBERS. |
| MAXIMUM INTENSITY= | 1374.7 | AT | 1553.485 WAVENUMBERS. |
| MAXIMUM INTENSITY= | 1985.9 | AT | 1554.280 WAVENUMBERS. |
| MAXIMUM INTENSITY= | 2362.9 | AT | 1554.950 WAVENUMBERS. |
| MAXIMUM INTENSITY= | 2391.7 | AT | 1555.490 WAVENUMBERS. |
| MAXIMUM INTENSITY= | 1827.0 | AT | 1555.900 WAVENUMBERS. |
| MAXIMUM INTENSITY= | 1002.4 | AT | 1556.190 WAVENUMBERS. |
| MAXIMUM INTENSITY= | 288.94 | AT | 1556.350 WAVENUMBERS. |

TABLE OF CONVOLUTED CARS INTENSITY MAXIMA:

| | | | |
|--------------------|---------|----|-----------------------|
| MAXIMUM INTENSITY= | 5.2406 | AT | 1547.595 WAVENUMBERS. |
| MAXIMUM INTENSITY= | 0.45077 | AT | 1547.980 WAVENUMBERS. |
| MAXIMUM INTENSITY= | 14.084 | AT | 1549.030 WAVENUMBERS. |
| MAXIMUM INTENSITY= | 0.61515 | AT | 1549.400 WAVENUMBERS. |
| MAXIMUM INTENSITY= | 34.609 | AT | 1550.335 WAVENUMBERS. |
| MAXIMUM INTENSITY= | 0.88997 | AT | 1550.685 WAVENUMBERS. |
| MAXIMUM INTENSITY= | 75.799 | AT | 1551.515 WAVENUMBERS. |
| MAXIMUM INTENSITY= | 146.40 | AT | 1552.565 WAVENUMBERS. |
| MAXIMUM INTENSITY= | 244.65 | AT | 1553.490 WAVENUMBERS. |
| MAXIMUM INTENSITY= | 351.64 | AT | 1554.285 WAVENUMBERS. |
| MAXIMUM INTENSITY= | 426.62 | AT | 1554.955 WAVENUMBERS. |
| MAXIMUM INTENSITY= | 422.01 | AT | 1555.500 WAVENUMBERS. |
| MAXIMUM INTENSITY= | 326.83 | AT | 1555.915 WAVENUMBERS. |
| MAXIMUM INTENSITY= | 185.59 | AT | 1556.210 WAVENUMBERS. |

DO YOU WANT A PLOT? (YES OR NO) (A) YES

Appendix C (continued)

WHICH ONE? (UNCONVOLUTED OR CONVOLUTED) (A) UNCON

ENTER MAXIMUM INTENSITY:(F) 2392.

ENTER MINIMUM INTENSITY:(F) 0.

ENTER NUMBER OF Y-AXIS TIC MARKS:(F) 10.

ENTER NUMBER OF WAVENUMBERS BETWEEN X-AXIS
TIC MARKS:(F) 1.

ENTER 0 FOR TEK PLOT OR 1 FOR XY PLOT:(I) 1

PAUSE -- SET ZERO ON XY

PAUSE -- SET MAXIMUM GAIN (FULL SCALE) ON XY

PAUSE -- SET GAIN FOR MINIMUM X AND Y

PAUSE -- SET ZERO ON XY

PAUSE -- SET MAXIMUM GAIN (FULL SCALE) ON XY

PAUSE -- SET GAIN FOR MINIMUM X AND Y

DO YOU WANT AXES DRAWN? (YES OR NO):(A) YES

DO YOU WANT ANOTHER PLOT? (YES OR NO):(A) YES

WHICH ONE? (UNCONVOLUTED OR CONVOLUTED) (A) CON

ENTER MAXIMUM INTENSITY:(F) 426.7

ENTER MINIMUM INTENSITY:(F) 0.

ENTER NUMBER OF Y-AXIS TIC MARKS:(F) 10.

ENTER NUMBER OF WAVENUMBERS BETWEEN X-AXIS
TIC MARKS:(F) 1.

ENTER 0 FOR TEK PLOT OR 1 FOR XY PLOT:(I) 1

PAUSE -- SET ZERO ON XY

PAUSE -- SET MAXIMUM GAIN (FULL SCALE) ON XY

PAUSE -- SET GAIN FOR MINIMUM X AND Y

DO YOU WANT AXES DRAWN? (YES OR NO):(A) NO

Appendix D. Tuning Ranges of 355 nm Pumped Laser Dyes from 410 to 715 nm.

Volume 29, number 3

OPTICS COMMUNICATIONS

June 1979

TUNING RANGES OF 355 NM PUMPED DYES FROM 410 TO 715 NM

Dennis M. GUTHALS and Joseph W. NIBLER

*Department of Chemistry, Oregon State University,
Corvallis, Oregon 97331, USA*

Received 27 February 1979

Wavelength tuning ranges and optimal concentrations are reported for 16 commercially available laser dyes pumped with the third harmonic of a Nd-YAG laser at 355 nm. The laser dye outputs cover the visible range from 410 to 715 nm.

The recent commercial availability of Nd-YAG pumped dye lasers and the growing list of laser dyes makes tuning curve information very helpful in choosing the minimum number of dyes to cover a spectral region. Much information is available from the dye and laser manufacturers on flashlamp, N₂, Ar, and Kr pumped dyes, some on the doubled Nd-YAG (532 nm) pumped dyes, but very little on the triplet Nd-YAG (355 nm) pumped dyes. In the course of developing a flexible tunable laser system for CARS and other applications [1], we have found it necessary to determine optimum concentration and tuning ranges for a variety of dyes pumped at 355 nm. Although such results will vary somewhat with dye laser configuration, the curves and data presented here should serve as a useful starting point for others employing such a pumping source.

The dye laser oscillator used in this work was of the transverse pumped Hänsch type [2] employing a wedged quartz flow cell, a 20X beam expander, a 136 line/mm echelle grating operated near its 63.5° blaze angle (eight to thirteenth order), and an output coupler whose reflectivity varies from ~5% at 400 nm to ~30% at 700 nm. The pumping source was provided by a Nd-YAG oscillator-amplifier (Quanta-Ray model DCR-1A) which generates a primary 1064 nm beam. The third harmonic at 355 nm was obtained by passing the primary beam through two KD*P type II crystals, the first a 25 mm crystal cut at 55° for frequency doubling, and the second a 30 mm summing crystal cut at 58°. The beams were separated by

means of a quartz prism and a quartz telescope (~2X) was used to match the 355 nm beam diameter to the 8 mm width of the dye cell. A cylindrical lens ($f = 400$ nm) focused the beam to a horizontal line about 7 mm behind the surface of the dye cell. Typically the pump pulse was 6–8 mj of 355 nm radiation (~8 ns duration) and this was polarized at 45° for irrelevant experimental reasons. The linewidth of the dye laser output was ~0.2 cm⁻¹ and the output polarization varied for different dyes because of grating reflection changes with wavelength.

A list of the laser dyes tested is summarized in table 1 along with solvents, concentrations, and lasing ranges. No special effort was made to optimize the efficiencies by variation of the output coupler or other cavity parameters. The dye laser output curves are presented in fig. 1. Because of their innocuous nature, water, methanol, and ethanol were selected as solvents. However, considerable wavelength tuning may be achieved by varying the solvent for some dyes, with λ_{\max} generally increasing with increasing solvent polarity. An example of this is coumarin 481 which shows a shift in λ_{\max} from 520 to 483 nm (table 1) and a two-fold increase in efficiency as the solvent is changed from ethanol to the less polar dioxane. Identical results for coumarin 481 pumped with the N₂ laser have been reported [3] and, in general, the pumping performance of the 355 nm source appears to be quite similar to that of a 337 nm N₂ laser.

Appendix D (continued)

Table 1
Concentration and tuning ranges for 355 nm pumped dyes

| Laser dye (Source) ^a | Solvent | Concen. M × 10 ³ | Lasing wavelength (nm) | |
|------------------------------------|---------------------------|--------------------------------|------------------------|---------|
| | | | λ _{max} | range |
| Stilbene 420 | Methanol/Ethanol (1/1) | 1.5 | 425 | 415–435 |
| Coumarin 450 | Ethanol | 1.0 | 488 | 435–463 |
| Coumarin 460 | Ethanol | 5.0 | 454 | 440–475 |
| LD 466 | Ethanol | 1.0 | 462 | 450–485 |
| Coumarin 481 | Dioxane | 5.0 | 483 | 465–510 |
| | Ethanol | 10.0 | 520 | 500–540 |
| Coumarin 500 | Ethanol | 5.0 | 504 | 485–530 |
| Coumarin 522 | Ethanol | 5.0 | 525 | 505–550 |
| Disodium fluorescein | Ethanol/Water (1/1) | 5.0 | 550 | 536–568 |
| Rhodamine 575 | Ethanol | 0.40 | 562 | 552–582 |
| Rhodamine 6G (Eastman) | Ethanol | 2.5 | 577 | 567–602 |
| Rhodamine B (Allied) | Ethanol | 2.0 | 602 | 595–640 |
| Rhodamine 610 | Ethanol | 5.0 | 623 | 595–645 |
| Cresyl violet 670 | Methanol/Water | 1.0 | 648 | 639–679 |
| Rhodamine 640 | Methanol/Water (3/2) | 3.5 | 650 | 620–680 |
| Oxazine 720 | Ethanol | 1.5 | 673 | 664–690 |
| Nile blue 690 + Rhodamine 640 | Methanol/Water (3/2) | 1.5 0.15 | 698 | 682–715 |

^a) Unless otherwise noted, all dyes were obtained from Exciton.

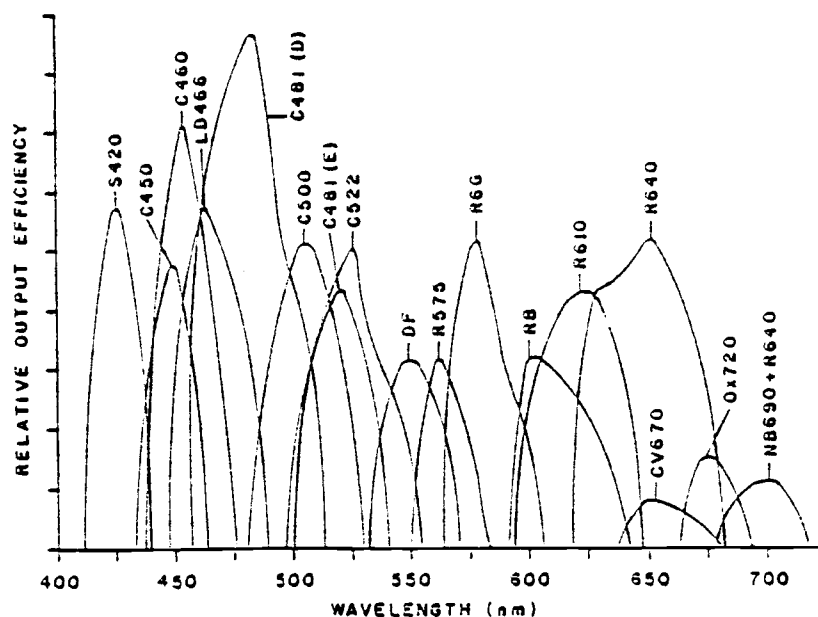


Fig. 1. 355 nm pumped laser dye tuning curves. S = stilbene, C = coumarin, DF = disodium fluorescein, R = rhodamine, CV = cresyl violet, Ox = oxazine, NB = Nile blue, D = dioxane, E = ethanol.

Appendix D (continued)

Volume 29, number 3

OPTICS COMMUNICATIONS

June 1979

Research support by the National Science Foundation is gratefully acknowledged.

References

- [1] D. Guthals, K.P. Gross and J.W. Nibler, *J. Chem. Phys.*, to be published.
- [2] T.W. Hänsch, *Appl. Opt.* 11 (1972) 895.
- [3] J.W. Halstead and R.R. Reeves, *Optics Comm.* 27 (1978) 273.